universität wien

MASTERARBEIT | MASTER'S THESIS

Titel | Title

Simulating Space Charge Effects in the ILIAMS Ion Cooler

verfasst von | submitted by

Daniel Mario Baumgartner BSc

angestrebter akademischer Grad | in partial fulfilment of the requirements for the degree of

Master of Science (MSc)

Wien | Vienna, 2024

Studienkennzahl lt. Studienblatt | Degree programme code as it appears on the student record sheet:	UA 066 876
Studienrichtung lt. Studienblatt | Degree programme as it appears on the student record sheet:	Masterstudium Physics
Betreut von | Supervisor:	Univ.-Prof. Dipl.-Ing. Dr. Robin Golser

Acknowledgements

The assignment of simulating space charge effects in the ILIAMS ion cooler initially seemed to me like a relatively straightforward task for a person with keen understanding and substantial experience of working with computers. Over time, however, it proved to be a stubborn adversary, throwing up obstacles, setbacks and unforeseen problems on a regular basis and the phrase "taking two steps forward and three steps back" became a prominent expression to describe my progress. However, knowing the importance of solving this task equipped me with the necessary willpower and motivation to continue. Looking back at these times, there are several people I must acknowledge and thank for their support, without whom the strain of this challenge on my mental health would have been significantly less bearable.

First and foremost, I would like to thank my supervisor and the research group as a whole, for making this thesis project possible and providing me with everything I needed to conquer this task and more. I would also like to thank my colleagues, who helped me in more ways than one. They were always available for practical discussions, shared their opinions for current conundrums or provided new perspectives when stuck at an impasse. Their knowledge in different areas of research and their experience in the scientific world were invaluable to this project and my learning experience. And, if nothing else, they often provided a distraction, sometimes more welcome than others, but always needed. In a similar manner I have to thank all of my friends, some of whom started out as colleagues, for their continued support and providing respite outside of the work environment.

Also, definitely not to be forgotten, I must thank my dear parents. The amount of unwavering support and care they have given, not always asked for but always very much appreciated, is something that cannot be taken for granted and for which I cannot be grateful enough.

Finally, I would like to thank everyone who has contributed in any way to the development of this thesis and who could not be included in the previous words, as so many people have made an impact, either by providing scientific input or by providing emotional support to the author. Without all of you, this work would not be the same.

Abstract

Isobars, nuclei or molecules of identical nucleon mass, are a common adversity in mass spectrometry because the typically electromagnetic mass selecting apparati cannot feasibly separate them. Ion-Laser InterAction Mass Spectrometry (ILIAMS) is a novel approach to suppressing this isobaric interference for high sensitivity Accelerator Mass Spectrometry (AMS) measurements, developed and successfully employed by the Isotope Physics research group at the Vienna Environemental Research Accelerator (VERA). Laser-induced photodetachment neutralizes anions if the photon energy surpasses the electron detachment energy threshold, removing them from the ion beam. ILIAMS thus uniquely enables the measurement of new isotopes and improves sensitivity for others. For near-total suppression, the ion-laser interaction time must be in the millisecond range, which is achieved through step-wise electrostatic deceleration followed by injection into a gas-filled Radio Frequency Quadrupole (RFQ) cavity. There, the ions cool down to only a few eV of energy and diffuse forwards, biased by the gradient of a constant guiding potential and radially confined by the alternating RF field to guarantee good ion-laser beam overlap. This unique configuration provided excellent results but also exhibited obscure behaviour, including a strong beam current dependence of ion residence time. A major impact of space charge effects was suspected, but impossible to experimentally detect with the diagnostic instruments available, thus necessitating this work. Ion propagation through the buffer gas has been simulated before [1], and the existing COMSOL®Multiphysics model, was extended to include the computation of space charge effects. Simulations in a simpler, smaller model show the large impact of space charge in RFQs in general, e.g. an increase in average radial distance from the axis, especially in combination with buffer gas. An arbitrary, accelerating force in a range typical for Coulomb interaction is shown to be able to cause shortened residence times. An iterative method of computing the space charge field confirmed a significant increase in space charge density for larger beam currents. Finally, the fully dynamic simulation of an injected ion pulse at different currents allowed important insights into the development of space charge fields and initial ion propagation, as well as the effects of injection cut-off. The ions accumulate at their mean deposition depth and build up a strong electric potential, which can accelerate ions towards the exit, while also acting as a barrier for lower-energy ions.

Kurzfassung

Isobaren, Kerne oder Moleküle mit identischer Nukleonenmasse, sind ein häufiges Problem in der Massenspektrometrie, da die typischerweise elektromagnetischen Massenselektoren sie nicht trennen können. Ion-Laser InterAction Mass Spectrometry (ILIAMS) ist ein neuartiger Ansatz zur Unterdrückung dieser Isobaren-Interferenz für hochempfindliche Accelerator Mass Spectrometry (AMS)-Messungen, der von der Isotopenphysik-Forschungsgruppe am Vienna Environemental Research Accelerator (VERA) entwickelt und erfolgreich eingesetzt wurde. Laserinduziertes Photodetachment kann Anionen neutralisieren und aus dem Ionenstrahl entfernen, wenn die Photonenenergie die Schwelle ihrer Elektronenablösungsenergie überschreitet. Auf diese Weise ermöglicht ILIAMS die Messung neuer Isotope und verbessert die Empfindlichkeit für andere. Für nahezu vollständige Unterdrückung muss die Wechselwirkungszeit zwischen Ionen und Laser im Millisekundenbereich liegen, was durch stufenweise elektrostatische Abbremsung und anschließende Injektion in eine gasgefüllte Radiofrequenz-Quadrupol-Kammer erreicht wird. Dort kühlen die Ionen auf eine Energie von nur wenigen eV ab und diffundieren vorwärts, wobei sie durch den Gradienten eines konstanten Leitpotentials beinflusst, und durch das RF-Wechselfeld radial begrenzt werden, um einen guten Überlap von Ionen- und Laserstrahl zu gewährleisten. Diese einzigartige Konfiguration lieferte hervorragende Ergebnisse, wies aber auch ein teilweise undurchsichtiges Verhalten auf, einschließlich einer starken Abhängigkeit der Ionenverweilzeit vom Strahlstrom. Es wurde vermutet, dass Raumladungseffekte einen großen Einlfuss haben, welche jedoch mit den verfügbaren Diagnoseinstrumenten nicht experimentell nachgewiesen werden konnten, so dass diese Arbeit erforderlich wurde. Die Ionenausbreitung durch das Puffergas wurde bereits zuvor simuliert [1], und das verwendete COMSOL®Multiphysics-Modell wurde erweitert, um Berechnungen der Raumladungseffekte zu ermöglichen. Simulationen in einem einfacheren, kleineren Modell zeigen den großen Einfluss der Raumladung in Radiofrequenz-Quadrupolen im Allgemeinen und eine Zunahme des durchschnittlichen radialen Achsenabstands, insbesondere in Kombination mit Puffergas. Es wird gezeigt, dass eine hypothetische Beschleunigungskraft in einem für die Coulomb-Wechselwirkung typischen Bereich in der Lage ist, für verkürzte Verweilzeiten zu sorgen. Eine iterative Methode zur Berechnung des Raumladungsfeldes bestätigte eine signifikante Zunahme der Raumladungsdichte für größere Strahlströme. Abschließend ermöglichte die volldynamische Simulation eines injizierten Ionenpulses bei verschiedenen Strömen wichtige Einblicke in die Entwicklung der Raumladungsfelder, das anfängliche Verhalten der Ionenausbreitung sowie die Auswirkungen einer Injektionsunterbrechung. Die Ionen sammeln sich rundum ihre mittleren Eindringtiefe und bauen ein starkes elektrisches Potenzial auf, welches die Ionen zum Ausgang hin beschleunigen kann, und zugleich auch als Barriere für Ionen niedrigerer Energie wirkt.

Contents

1 Introduction

1.1 AMS and VERA

The Vienna Environmental Research Accelerator (VERA) is an Accelerator Mass Spectrometry (AMS) facility run by the Isotope Physics group of the Physics Department of Vienna University [2].

AMS is an approach to mass spectrometry with the best detection limit reaching 10^{-16} [3] or even 10^{-17} for some isotopic ratios [4, 5]. It is therefore the method of choice to measure rare radioisotopes and often the only solution to conquer various research goals and novel problems in a wide range of fields such as environmental research, geology, dating, astrophysics, medical research, and more.

The centerpiece in the AMS setup at VERA is the 3 MV tandem accelerator granting binal acceleration of anions utilizing a positive terminal and an electron stripping medium.

VERA was continuously modified and extended over the years and it performed exceptionally well under the difficult and intense conditions it was put under to achieve important research goals since its commissioning in 1996. [6, 7, 8, 9, 10, 11]

Method development and scientific progress were always important decision factors for the research group as opposed to solely focusing on radiocarbon dating or measurements for commercial purposes [12, 13, 14].

One of the most significant advancements was the development of the Ion-Laser InterAction Mass Spectrometry (ILIAMS) setup, which tackles the challenge of isobar suppression in a unique and exceptional way [15, 16, 17, 18, 19].

1.2 ILIAMS

Molecules and nuclei with equal mass to the species of interest are a fundamental problem in mass spectrometry as they behave identically in electromagnetic fields. With molecular isobars being dissociated by the AMS stripping process, the only interference can be found on the nuclear chart. Yet, because of the low detection limit through single atom counting, the need for near absolute isobar suppression is particularly adamant.

Chemical preparation and treatment can reduce, but rarely sufficiently eliminate the other element and are in addition extensive, require near perfect laboratory conditions and are sometimes simply not possible. Isobars that do not form stable anions in the ion source are a rarity[1] and the more general, nuclear charge dependent[2] approaches such as beam degrading and complete stripping of the ions (i.e. removing all electrons) are typical ways to deal with

[1] e.g. ^{14}C and ^{14}N

[2] Z-dependent

isobars for the AMS method[3] but are highly dependent on the beam energy [20]. For some ions[4], the necessary energies cannot be reached by the most powerful tandem accelerators operating at 15 MV, and without isobar suppression these ions cannot be measured. As an increasing number of high energy AMS facilities worldwide are decommissioned and the trend towards low energy setups and relevant methods increases, this becomes a matter of global impact [21].

The ILIAMS setup is, at its heart, a radiofrequency-quadruple (RFQ) buffer gas ion cooler combined with a multi-laser setup that collinearly overlaps a laser beam of specific energy with the ion beam axis. Anions from a caesium sputter source are first pre-decelerated via electrostatic lenses, then further cooled by elastic buffer gas collisions and confined in harmonic, oscillatory motion by the RF field while a static guiding field propagates the negative ions towards the exit. The laser enables photodetachment if the laser photon energy is sufficiently large to surpass the detachment energy of the particles' electronic configuration.

If the isobar, or a suitable molecular configuration incorporating it, has lower detachment energy compared to the Isotope of Interest (IoI) or respective molecule, the laser neutralizes the isobaric component of the ion beam inside the ion cooler, which is then no longer affected by the electric fields and fully thermalizes in the buffer gas. In some cases, interaction with, and chemical processes in the cooling gas cause similar results. In any case, the unaffected anionic IoI beam component is driven towards the exit by the fields, extracted, re-accelerated, and passes through the remaining AMS setup to be accelerated, stripped, separated and counted in the detector [15].

The exact processes taking place inside the ion cooler are however not completely understood and mainly speculated about. No model exists to definitively explain the contribution of ion-ion interactions such as coulomb repulsion, or chemical processes like molecular dissociation and recombination. Experimental data differs from simulations and phenomena take place that are not completely founded by the established theoretical background [22].

The effective ion-laser interaction time for photodetachment is in the millisecond range. Therefore, the residence time of the ions inside the cooler is an important measure. Previous experiments at VERA have shown, that the residence time and transmission are dependent on the beam current in a way that cannot be explained by simulations that take into account the ion optics and buffer gas alone. For large beam currents, the residence time becomes shorter and the ion beam transmission is considerably reduced [22]. Even precise simulations of the buffer gas distribution and using an advanced collision model within the extensive simulation software COMSOL Multiphysics®did not give results that are comparable to, or better explain experimental data [1].

1.3 COMSOL Multiphysics®

ILIAMS development was always concurrent with computer models and simulation. The most advanced model of the ILIAMS ion cooler so far exists within the software suit COMSOL

[3] e.g. ^{10}Be, ^{26}Al, ^{36}Cl
[4] e.g. ^{99}Tc, ^{90}Sr, ^{135}Cs

Multiphysics®, which offers simulation methods and tools for a wide range of physics [1, 23]. Within it, a model geometry can be created and distinct physical laws can be defined for each part. The relevant equations are applied to, and solved for these parts, and interaction of different physics can be achieved through "Multiphysics couplings". One such coupling is the effect an ion has on the surrounding, total electric field, which in turn slightly affects other ions and consequently the ion itself. This space charge field generated by ion bunches is suspected to have a larger than anticipated impact and was, prior to this work, not satisfyingly simulated for ILIAMS.

As more and more AMS facilities build upon the ILIAMS method, the importance of having a fuller understanding of the exact processes behind these phenomena becomes evidently predominant [24].

1.4 Motivation

These aforementioned factors are the motivational cornerstone for this thesis. To get a better understanding of thus far unexplained effects in ILIAMS is of paramount importance and essentially the gateway for future adaptations and improvements to the system itself and current, or future daughter projects. A practical comprehension of inadequately conceived effects complementing experimental results is necessary to find ways to optimize current methods, as well as overcome limits of measurement, and finally, to nurture the scientific heritage of this system.

As the main suspected contributor to these so far barely explored effects is space charge, this thesis undertakes the tasks of partly enlightening the dimness surrounding distinct anomalies of ILIAMS operation. Since experimental methods of examination are difficult due to the inaccessibility of the device during measurements and missing diagnostic apparati, the path towards understanding space charge effects starts with simulations. These were done in the software COMSOL Multiphysics®, which was chosen because of accessibility and an already present, mature model that could be readily extended to include space charge. COMSOL makes it effortless to add the effects of numerous physical formulations, as well as quickly and effortlessly modifying any model. Functionalities to perform precise particle trajectory studies in electric or magnetic fields, as well as Monte Carlo studies of statistical interactions such as with matter or a buffer gas, raise it to be an excellent particle tracing software and the stocked formalism concerning space charge readies multiple approaches to model, simulate and compute related effects.

In the final discussion, the simulation results shall be evaluated in light of computational restrictions and accuracy, while connections and implications for the real model are reviewed. Lastly, hypothetical adaptations to better overcome measurement restrictions are brought forth.

2 ILIAMS – Theory and Methods

2.1 AMS

Ion-Laser InterAction Mass Spectrometry (ILIAMS) is designed to work with Accelerator Mass Spectrometry (AMS). Because of the continued exploration of new methods and improvements to the beamline, the VERA AMS setup exceeds the capabilities of several other AMS facilities focused solely on measuring radiocarbon or other "mainstream" isotopes and especially ILIAMS opened the door for the measurement of several new nuclides.

Anions are provided by a Multi Cathode Source for Negative Ions by Cesium Sputtering (MC-SNICS) and then directly pass through a mass separation setup consisting of an Electrostatic Analyzer (ESA) for separation by energy-charge ratio (E/q) and a Bending Magnet (BM) that further separates by mass-charge ratio (ME/q^2) and injects the beam of selected mass into the tandem accelerator, while currents of neighbouring masses can be collected in offset Faraday cups. A Multi Beam Switcher (MBS) applies voltage to the injection magnet chamber enabling fast varying, or switching of the desired injected mass via kinetic energy modulation.

In the accelerator tank, a set of two charging chains transport positive charge to a central terminal and generate an electric potential of up to 3 MV, through an assemblage of large, annular resistor structures in the SF_6 filled tank. The anions accelerate towards the large positive potential, where the molecular bonds are broken up and electrons stripped off by collisions in a thin foil or a dedicated gas. Cations emerge in various charge states and are now accelerated away from the potential, resulting in energies in the range of several MeV.

Thus, the positive terminal divides the low energy side of the beamline complex from the high energy side, where the cations are again mass separated by a BM and an ESA. Isotope currents can be measured down to pA at various points in Faraday cups while detectors, namely gas ionization chambers or Bragg detectors, enable single atom counting and isobar separation by energy loss characteristics ($\Delta Z/Z$). Other peripherals such as Wien filters, quadrupoles, slits, lenses and steerers are distributed over the beamline to control and optimize ion optics and detection rates. Computer software enables the remote control of nearly all devices and the utilization of scripts for automation or optimization. An extensive diagram of the setup is provided in A.1 and a more detailed description of the entire machine can be found in related papers by the research group [11, 12].

In 2010, work began on ILIAMS, a device capable of isobar suppression through photo-detachment, to improve efficiency or even allow measurements of isotopes that are thus far inaccessible to any other AMS facility [19] and paved the way for important milestones including the improvement of measurement sensitivity for ^{36}Cl, [25], increased detection efficiency for ^{26}Al, [26] and opened the door for measuring ^{90}Sr [27], ^{99}Tc [28] or ^{135,137}Cs [29] at VERA.

2.2 ILIAMS

In essence, Ion-Laser InterAction Mass Spectrometry (ILIAMS) is a buffer gas filled Radio Frequency Quadrupole (RFQ) ion cooler with a laser collinearly overlapping the ion beam axis to perform photodetachment of unwanted anionic isobars with lower detachment energy than the respective Isotope of Interest (IoI). Because of the interaction time requirement for the reaction in the order of milliseconds, the ion beam must be decelerated and cooled, which is done through energy loss in buffer gas interactions. The RFQ is needed to confine the ions scattered in the buffer gas to the central axis. The following sections are dedicated to exploring the various components and effects relevant for ILIAMS [15].

2.2.1 Radiofrequency Quadrupoles

Radio Frequency Quadrupoles (RFQs) were found to be an important cornerstone of modern accelerator physics and related fields since their conceptualization more than 50 years ago [30, 31]. Over the years, adaptations and advancements brought forth a multitude of varying designs with different strengths and applications in a wide range of fields. The core principle, however, is essentially the same for all configurations.

In a cavity, four poles are ordered in a planar four-fold symmetry with certain distance from the rotational axis forming a quadrupole that is linearly extruded in parallel to the beam axis. The absolute value of charge is identical for each pole, but the sign of charge is opposite for the poles on the perpendicular plane. An alternating current causes the charge of the poles to oscillate with certain frequency. This periodic, electric field modulation applies a time harmonic force to any charge entering the field.

The ions perform microscopic motion through oscillations in coherence with the RF period, while field inhomogeneities cause a net force average over several periods, the ponderomotive force, causing a superposed macromotion. With the right frequency and voltage, a charged particle entering in near parallel direction to the rods can be manipulated to verge into a trajectory of highly complex, oscillatory motion. The trajectory resembles an irregular helix with an incline dependent on electric parameters and distinct, repeating patterns of superposed periodicities. Visual representations of particle trajectories for various parameters of the RF field are found in A.2. An appropriate setup enables RFQs to be used for different applications including beam bunching, ion beam acceleration with near constant emittance or even mass separation by use of a superposed, static potential field. Ion-Laser InterAction Mass Spectrometry (ILIAMS) is a rod type RFQ, meaning the four poles, or electrodes are made up of cylindrical rods held in place in a device case by non-conductive spacer plates [31, 32].

Mathieu Parameters

For an ion of certain mass m and charge Q, there is a continuous set of combinations of RF-voltage V_{RF} and circular frequency ω that allows the oscillating ions to stay within the bounds or inscribed radius r_0 of the rods. These combinations are derived from solutions to equation 2.1, Mathieu's differential equation, that can represent the equation of motion of

a charged particle in a time harmonic field with help of the parameters $a,\ q$ and $\tau = \omega t/2$, where a and q are different for radial and axial direction as seen in equation 2.2 [33, p.17-19].

$$\ddot{y} + (a - 2q\cos(2\tau))y = 0 \tag{2.1}$$

$$q_r = \frac{2QV_{RF}}{mr_0^2\omega^2}, \quad q_z = \frac{4QV_{RF}}{mr_0^2\omega^2} \tag{2.2}$$

Parameter a represents a constant shift in the Mathieu equation, which can correspond to a superposed, direct current (DC) field. As the RFQ in ILIAMS is only used to constrain the ion beam close to the central axis, essentially operating as a linear Paul trap, no DC field is required and $a = 0$. Thus q, the only relevant parameter, provides an excellent reference measure to describe the behavior of the ions in the device. The typical range of q-values is from over 0 to below 1. A simple schematic of a linear RFQ trap is provided in figure 2.1.

The "Areas of stability", the planes of possible combinations for a and q, or RF frequency $f_{RF} = \frac{\omega_{RF}}{2\pi}$ and V_{RF} values that the motion of ions of specific mass and charge is still stable for via equation 2.1 in a certain trap geometry are different for radial and axial direction and have to overlap for stable particle transmission [34].

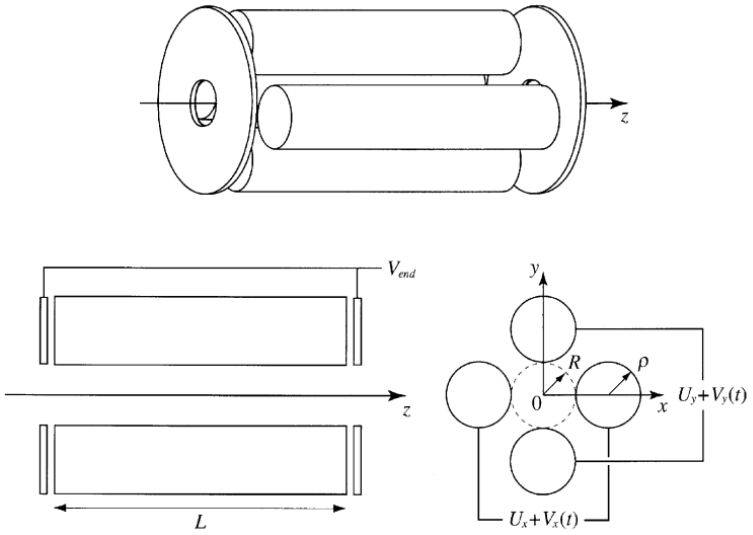

Figure 2.1: Simple schematic of an RFQ linear Paul trap taken from [35, Fig.1]. End Cap Voltage V_{end} can be used for de-/reacceleration and for focusing, the four round poles of radius ρ inscribe a radius of $R = r_0$. The RF-voltage $V_{RF} = V_x(t) = -V_y(t)$ is a constant time harmonic AC field while U_x, U_y are constant, static DC voltages, which are 0 for ILIAMS.

While the theory is rigorous, a basic, phenomenological description of the effect of different q-values requires no special expertise. Ion trajectories are greatly influenced by the initial phase of the RF field when they encounter it, as it defines their main axis of oscillation. From equation 2.2 it is noticeable, that higher q equivalents larger V_{RF} over ω ratio. For low q-values,

the low voltages and high frequencies lead to an ion propagation vector that is barely affected by the field and only when reaching close distance to the rods is their movement direction majorly changed. This leads to a trajectory with a lot of small scale vibration, or micromotion, and a small degree of large scale motion, or macromotion, resulting in an ion trajectory, that swings around the inscribed radius only very slowly. For high q-values, the higher voltages at lower frequency lead to the ions being accelerated towards the poles more strongly and reaching close distances more quickly but the alternating field changes their propagation vector more rapidly than for low q-values. A stronger perpendicular acceleration leads to more prominent micromotion and a more pronounced helical trajectory. The superposition effect from macromotion causes the ions to change from an episode of large amplitudes and high velocities to smaller amplitudes and lower velocities periodically. Operating outside of the area of stability entails either a RF field, that shifts polarity too slowly and causes ions to collide into the pole structures before the alternating field can sufficiently divert their trajectory if the field strength accelerates them too quickly, or an AC voltage that is insufficient to redirect and confine the ions within one period [17, 33].

In ILIAMS, best transmission is usually seen when the q value is between 0.4 and 0.5. This correlates to the main purpose of the RFQ to confine ions close to the central axis and hinder the ions from being diffusely broadened by scattering in the ion cooling buffer gas [22].

2.2.2 Ion Cooling

Ion cooling describes the slowing down and reduction of vibrational and kinetic energy of ions. In ILIAMS, this is achieved through collisions, or elastic scattering, in a very low pressure buffer gas bled into the RFQ cavity. The total forward momentum is reduced by transferring kinetic energy to the collision partner and through an increased path length as the ions are scattered off gas ions and deterred from their direct trajectory. The alternating electric fields of the RFQ keep the otherwise randomly diffusing ions closely confined to the central axis.

Cooling of ions can have multiple purposes, many of which lie in the field of mass spectrometry because of the mass-, or even Z-dependency of the effect. However, the AMS and ILIAMS-method requirement of an anionic ion beam presents additional difficulties as opposed to a cation beam because the additional electron is readily lost in collisional detachment or other chemical processes. Therefore the ion beam must be slowed down to energies below the collisional detachment threshold before entering the buffer gas filled cavity and noble gasses are usually the gas of choice because of their inertness. In some specialized cases, reactive gases such as N_2 or O_2 can be used to turn the cooling cavity into a reaction cell and neutralize selected isobars through chemical processes [22, 36, 37, 38].

Describing collisional interaction theoretically can generally be done on a multitude of levels, from quantum field theoretical computations over quantum mechanical descriptions to simply using Newtonian mechanics. For the calculation of a large number of interactions, a simple description is beneficial and often necessary to keep the equations solvable with available resources or within a reasonable time frame. In particle mechanics, the effect of gas collisions is often evaluated in Monte Carlo Simulations, computing for a large number of particles and statistical collisions over time while respecting boundary conditions.

For basic simulation purposes, a hard-shell collision model is fair. In this elastic collision

model, the colliding partners are treated as spheres with a hard, inelastic shell and due to the conservation of energy and momentum, the velocity of the particles after interacting depends only on their relative masses. Deflection angle and effects on the trajectory are only dependent on the incident angle of collision and size dimension of the hard shells. Because these collision details are assumed to be uniformly distributed for this model, the deflection angles must be uniformly distributed into all directions as well.

A more sophisticated model incorporates a variable cross section for this kind of interaction dependent on the relative velocities and is called Variable Hard Sphere (VHS) model. It specifically addresses the shortcomings of the raw hard shell method when it comes to high velocity collisions, as in reality the cross section for interaction reduces with increasing speed. Experimentally obtained data is used to derive reference cross sections and velocity dependent, variable cross sections are computed from them. The VHS model was used in earlier ILIAMS simulations and offered important insights on ion propagation and details can be found in the respective work [1, p. 12f.].

In ILIAMS, the buffer gas collisions cool the ions to near thermal velocities[1], increasing their residence times within the RFQ cavity to such a degree, that they have sufficient interaction time with the overlapping laser to achieve photodetachment.

2.2.3 Photodetachment

Photodetachment is a photon conveyed electron detachment process. Each electron confined in the orbital configuration of an atomic or molecular core R has a particular energy threshold, whereupon it is too excited to be bound to its orbital and detaches. Conveying this electron detachment energy E_{detach} by means of a photon of frequency ν is photodetachment given in reaction equation 2.3[2][22].

$$R^- + h\nu \Rightarrow R + e^- \qquad \text{if } h\nu > E_{detach} \tag{2.3}$$

Typically, the electrons in the outermost orbitals are bound most lightly. The binding energy of an additional electron to a neutral configuration, or equivalently the ionization energy of the anion is defined as the Electron Affinity (EA). The value is dependent on the different configurations of the positive core on an atomic level and is even more complexly affected for molecular anions, where the binding between elemental nuclei and their geometric constellation affect the molecular orbitals and energy levels. Further, geometric shifts between neutral and anionic molecule lead to further differentiation in energy, as can be seen in figure 2.2 [39], where the potential energy surfaces are different for molecule R and respective molecular anion R^-. It also becomes apparent that anions in an excited state have a lower effective detachment energy, as the distance to the nearest neutral ground state is decreased. So conclusively, while the EA correlates well with the detachment energy, it is no strict measure.

Atoms and molecules can form stable anions or negative molecular ions if their EA is positive meaning energy is required for detachment. The magnitude of the EA affects their production rate in a negative ion source and the cross section for photodetachment, as ions with higher

[1] Only heated/accelerated by the RF field
[2] With Planck constant h

EA are usually more stable. Excluding noble gases, in the periodic table of elements the EA generally increases from left to right and from top to bottom. Halogens therefore form the most stable anions, while alkali metals only form very unstable ones. Chlorine has the highest EA of all elements, but the EA of molecular anions can be higher, giving them their denomination: super halogens. Many stable or meta-stable molecular anions exist but their EA is often unknown because it is unique for each molecule and requires an individual and complex measurement procedure. Calculations are difficult, as the precise structure for each molecule must be computed for and approximations can lead to large differences from the real value [40, 41].

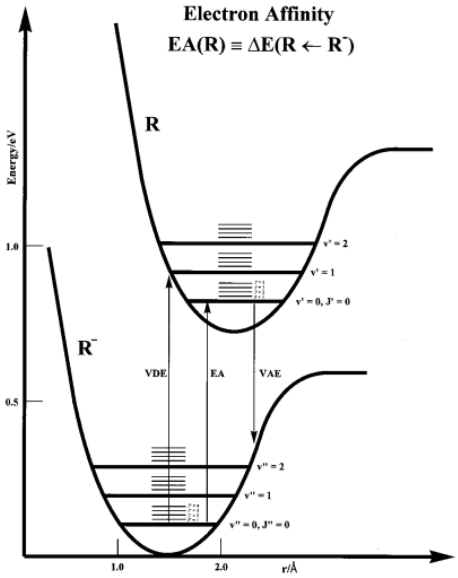

Figure 2.2: Illustration showing the potential energy surfaces and modes for a molecule R and the respective anion R^-. As they have a different equilibrium configuration, they relax their geometry accordingly towards the potential minimum after attachment/detachment resulting in different energy gaps. Adiabatic electron affinity (EA), vertical detachment energy (VDE) and vertical attachment energy (VAE) are indicated here [39, Fig.1].

Photodetachment is a non-resonant threshold process. It only occurs in interactions where the photon energy E is larger than the threshold energy, i.e. electron affinity EA, of the atomic or molecular system. The cross section σ then grows for increasing E according to Wigner's Law $\sigma(E) \propto (E - EA)^{l+0.5}$ for electron angular momentum l. The graph in figure 2.3 depicts the relation of two cross sections over photon energy for two distinct systems of different EA. A photon of energy between the two EAs can detach the electron of one system, but not the other [19]. The number of anions N in an interaction area with laser photons of energy $E > EA$ then decreases exponentially over time t and depends on photon flux Φ and the respective photodetachment cross section σ according to equation 2.4 [22].

$$N(t) = N(0)e^{-\sigma\Phi t} \tag{2.4}$$

As the process requires the isobar M to have a sufficiently lower EA than the IoI A, an appropriate system has to be found. If the single isotope species does not fit this criterion or gives bad beam current from low EA, a stable, molecular anion incorporating it can be selected. Stable super halogens from bonding with x fluorine atoms F are prime, exemplary candidates, providing higher beam currents and providing systems where $EA(\mathrm{MF_x}) \ll EA(\mathrm{AF_x})$. In

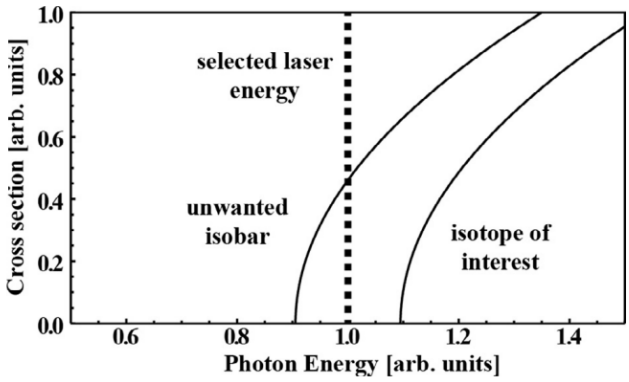

Figure 2.3: Illustrative graph for two different photodetachment cross sections σ dependent on photon energy E. A laser with rightly chosen energy neutralizes the unwanted isobar while not affecting the isotope of interest. [19]

ILIAMS, after the isobaric component of the ion beam has been neutralized through photodetachment, the remaining ions exit ILIAMS and continue onto the main beam line of the AMS setup.

2.2.4 ILIAMS Setup

An ion cooling, buffer gas filled RFQ cavity together with a photodetachment laser are the very basic ingredients in the ILIAMS work formula, but providing clean and stable beam injection and good transmission through the device requires intricate, pristine configuration and a large number of peripherals. The ILIAMS setup is described in detail in several publications [15, 16, 22] which shall be summarized in this section.

At VERA, an entire subsection of the complex is allocated to ILIAMS including a dedicated ion source. Negative ions provided by an MC-SNICS are pre-accelerated to 30 keV energy and separated in a double focussing, 90° bending magnet (r = 0.35 m, 8.4 MeVamu) that injects the ion beam into the setup. The ions are decelerated via a high voltage, and a low voltage lens, so that they enter the cooler segment with only about 50 eV energy. Grounded, conical apertures with a 3 mm opening cap the ends of the cylindrical cooler casing. The ions are slowed down further and have an increased path length from the collisions with the buffer gas atoms which causes them to diffuse and increases their residence time inside the photodetachment region, where the unwanted isobars can be neutralized with a 2.33 eV, 2.72 eV or 3.49 eV laser of up to

18 W power. The periodically changing field of the RF quadrupoles causes the movement of the ions to be biased towards the central axis, while a static guiding field generated by tilted, straight plate electrodes causes a linear potential gradient and bias in direction of the exit.

The exact voltages or frequencies used are dependent on the research parameters but are generally chosen, so that the Mathieu parameter q (see 2.2) is between 0.4 and 0.5. A maximal guiding field gradient of 15 V/m and an RF peak-to-peak voltage of 400 V with a frequency of up to 6 MHz can be reached with the setup. Helium or a helium-oxygen mixture has proven to be the optimal buffer gas, where the latter is prepared in a "gas balloon" reservoir. One turbopump in the center, and two turbopumps at each end help generate a stationary distribution of the buffer gas that is let into the beamline through a bleeding valve, as depicted in a schematic of the setup seen in figure 2.4. Photographs of one end of the ILIAMS setup, with the round quadrupole rods and planar guiding electrodes, held by a ceramic plate, are found in figure 2.5. Average pressures of around 3 - 5 Pa are targeted and, as previous research has shown, the gas distribution inside the cooler follows a step-wise distribution, because molecular diffusion inside the cooler is hindered by these ceramic spacer plates [1].

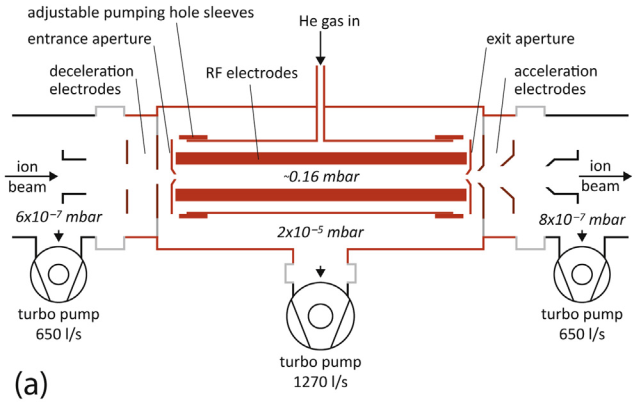

Figure 2.4: 2D schematic of the ILIAMS Setup including the vacuum configuration [22, Fig. 1a]

One of three tuned lasers on a laser optics table can be used to be collinearly overlapped with the ion beam. The laser beam exits the optics setup and enters the beamline through a window. After passing through the cooler and interacting with the ions it exits the beamline again through another window where the remaining laser power is then measured.

Once the remaining ions have passed the exit aperture, they are re-accelerated by a low and a high voltage lens, pass through an ESA and are switched onto the regular AMS beamline to be injected into the tandem accelerator.

The exact details on construction and electrical working are described elsewhere [22, 15], A diagram of the beamline setup including the optic table can be seen in figure A.1 and the ILIAMS setup sections in detail in figure 2.6.

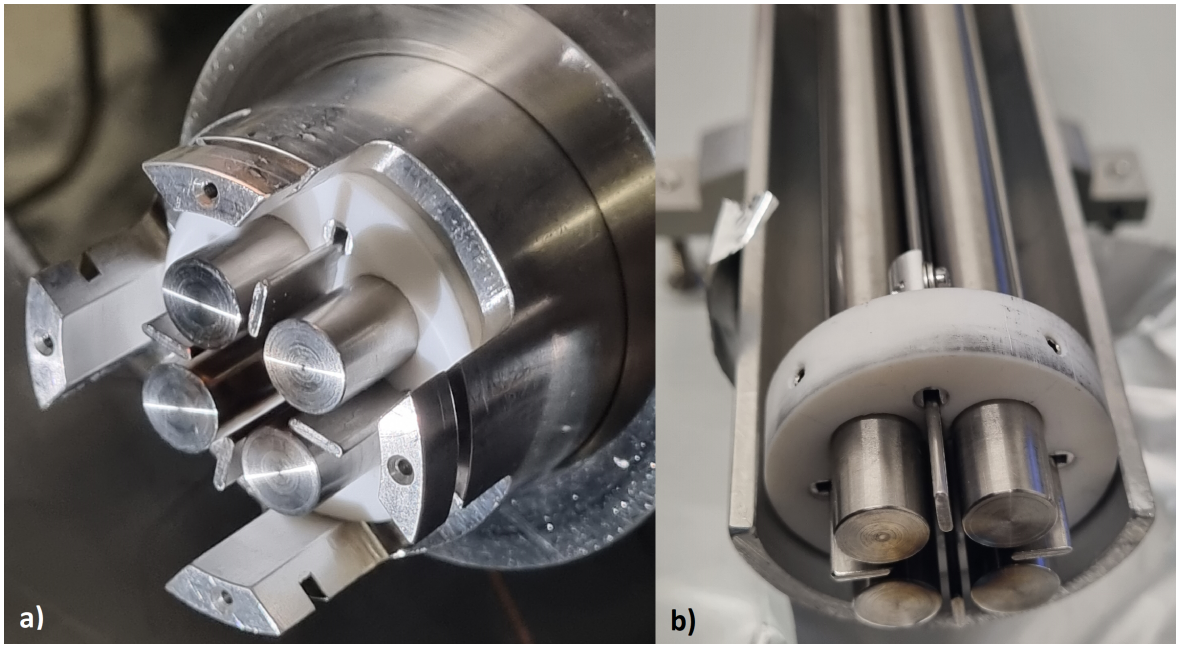

Figure 2.5: Photographs of the end of the ILIAMS rod structures. a): Picture of the round RF rods and planar guiding electrodes mounted in a ceramic plate. b): Structure during service within a storage case

2.2.5 Experimental Data and Problems

Even though ILIAMS quickly became an established method for isobar suppression in AMS and enabled the measurement of various new isotopes at VERA, there is still room for improvement.

Several aspects influence the performance of the ILIAMS method. A high percentage of ions successfully passing through the beamline section is a prime requirement for stable, reliable and time efficient measurements. Also, as the main objective is to suppress the isobaric component of the ion beam to blank levels or below, it is of great importance to keep narrow trajectories within the RFQ and maximize residence time, to ensure sufficient ion-laser interaction time.

Ion transmission is very high for a wide range of low ion beam currents and decreases slowly when reaching intensities of µA as seen in figure 2.7. Also, time of flight measurements through the cooler, determining the residence time of the ions, show the dependence of residence time on the buffer gas pressure, guiding field strength and most importantly, injected ion beam current in figure 2.8 [22].

As the most significant variations are achieved when varying the beam current, the main culprit responsible for out-of-theory behaviour is suspected to be space charge.

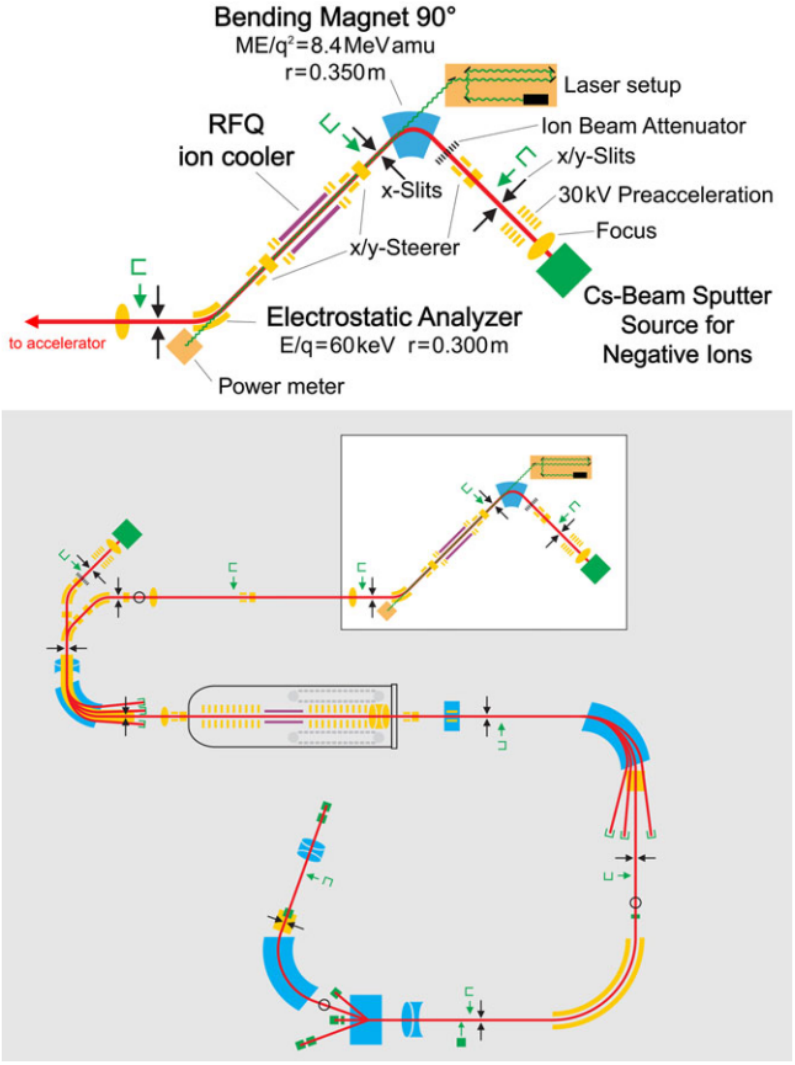

Figure 2.6: Layout of the ILIAMS setup (top) and position within the VERA complex (bottom) with yellow electrostatic, blue magnetic and green ion generation and detection components.[16, Fig.1]

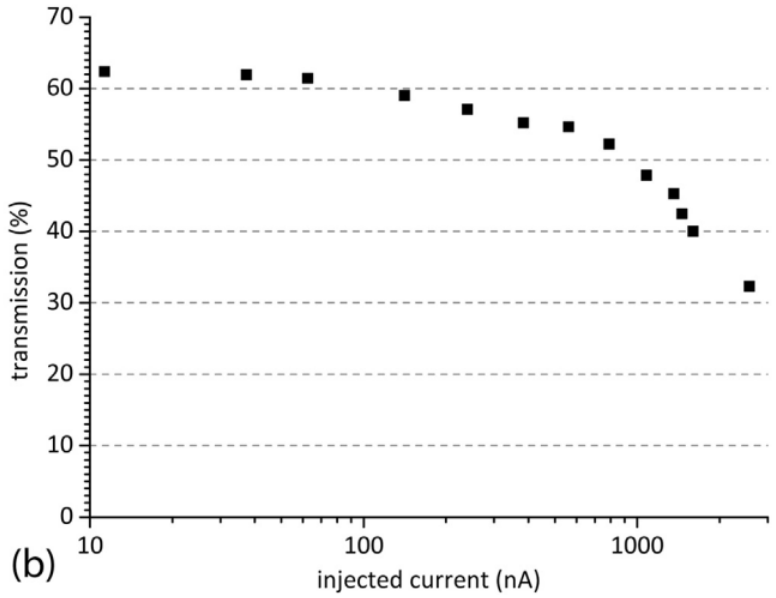

Figure 2.7: Plot showing the dependency of ion transmission in percent through the cooler on the injected ion beam current. There is a decline starting at 100 nA and a drop at 1000 nA [22, Fig.3b].

2.3 Space Charge

Space charge is the field of charges, such as charged particles, occupying a volume in space and affecting the effective total electric field. In the case of particles, it can be seen as the result of collective coulomb interaction within the ensemble. In beam dynamics calculations, this effect is typically not considered and the ions are only affected by exterior influences like electric or magnetic fields and do not interact or interfere with each other.

The considerable increase in complexity arising from accounting for the interaction of each individual charged particle with every other one in the entirety of the N-particle system on a microscopic level, for a total of N^N interactions, is the main reason it is often deliberately neglected, even though the effects of space charge on an ion beam are measurable. Phenomenologically, the self-repulsion within the system increases the beam size, can change its shape or affect the divergence.

In most cases, however, these interactions can indeed be readily neglected or are easily dealt with in an experimental setting, because the effect is small and predictable, as can be seen when comparing experimental data to beam dynamics simulations that ignore space charge. The interaction force is too small and the interaction time at typically high particle velocities is so short, that the actual effect is minor. For low velocities or very large beam currents, resulting in a comparatively high density of charges, the self-repulsion and effects of space charge become increasingly relevant. Nonetheless, in reality, small tweaks to the beam manipulation and steering devices can usually compensate for these effects and operators can,

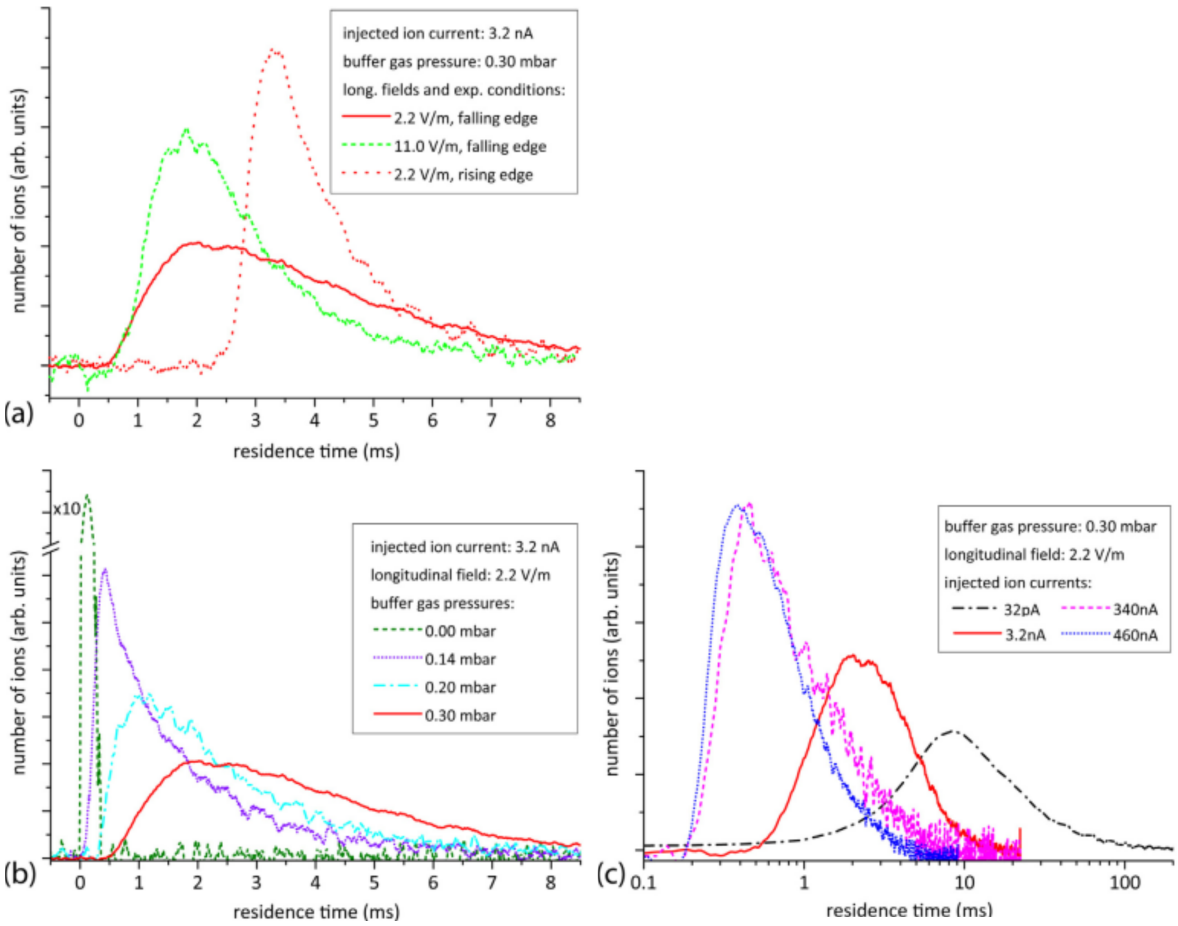

Figure 2.8: Plot showing the dependencies of residence time on guiding field strength (a), buffer gas pressure (b) and injected beam current (c) as measured by [22, Fig.4]

in practice, optimize the dynamics experimentally, without knowing specifics about space charge [32, 42, 43, 44].

Because of the ability to investigate the principal operation, without needing to assemble anything with expensive materials, simulations have quickly grown to play an important and practical role in the design of particle accelerator elements. The inclusion of space charge, however, increases the calculation cost and required time substantially. In practice, a slight discrepancy between experimental and simulated data is often expected due to computational approximations, model limitations or errors. As long as the space charge effects are small enough to be comparable to such simulation artefacts, it is deemed tolerable to neglect them, as it would not be worth the additional computational effort.

Nonetheless, as the anions within the ILIAMS ion cooler are continually injected, slowed down to near thermal speeds and tightly packed and confined by the RF fields, it becomes apparent that these effects can not be assumed to be negligible and are expected to affect the behaviour significantly. In addition, RFQs are prone to be negatively affected by space charge, since it can impact the transmission drastically, cause measurement errors, lower the ion motion frequency and impact measured mass when used as mass spectrometers [45, 46].

Even though space charge effects are a notorious issue in RFQs, no rigorous theory exists and in addition, hardly any investigation was performed for RFQ ion coolers, as they provide additional complexity through their buffer gas that essentially positions ILIAMS closer to being a chemical reaction cell, than an ion optical instrument.

In order to improve understanding and strengthen the theoretical background behind ion transport mechanisms with dominant coulomb repulsion, several different scientific approaches were taken.

2.3.1 Theoretical and stochastic approaches to describe space charge

Research on the statistical mechanics of coulomb systems is not a recent problem, as it is of great relevance in many fields of science including plasma, semiconductor or condensed matter physics, chemistry or any field where charges affect phenomenological change. Analytical solutions exist for simple cases like the one component plasma and in most cases only with a restricting number of approximations, but realistically complex systems are difficult to compute or even parameterize [47].

Envelope Equations

The figurehead of mathematically analytical beam dynamics descriptions are the beam envelope equations, where characterizing the time dependent propagation of a particle beam through a system is reduced to an analytical formulation using parameters within a 6D phase space. The size and shape of an ion beam are then fully defined by a phase space distribution function depending on particle position and momentum vector, representable as a phase space ellipse. According to Liouville's theorem, this distribution is time invariant and the phase space volume constant, if Hamiltonian particle dynamics are satisfied and no interactions are considered. Space charge self-effects can constitute in the form of a continuous potential, being added as an additional de-focusing force described by the Vlaslov equation, where the additional

field from space charge is coupled to the distribution function itself [48]. This enables the analytical investigation of the effect of space charge on ion beams where the movement is predominantly in forward direction and trajectories behave close to a ray optical approximation [49, 50]. However, Liouville's theorem is no longer satisfied, as soon as non-reversible, stochastic processes such as buffer gas collisions are considered. These processes change the phase space volume and necessitate the introduction of additional theory.

Early approaches integrate the stochastic attributes of scattering into the theory of envelope equations by implementing terms for emittance growth and beam expansion [51]. More recent approaches dive deeper into the modern stochastic methods and approach this problem supposing Markovian properties to the beam and develop a modified Fokker-Planck equation to include such effects into an equation framework [52].

Nonetheless, the model calculations being extensive and rarely straightforward to perform is but one hindrance of their application to find the space charge distribution within ILIAMS. They first and foremost dictate clear particle beam characteristics, where the particle propagation dominates in one particular direction and is predominantly defined via equations of motion in the classical or relativistic limit, typically behaving in a way similar to optical rays. In the conditions ILIAMS operates under, these characteristics are no longer clearly given, as the ions are cooled to energies close to full thermalization and essentially move with a velocity comparable to that of gas molecules at room temperature. Under these conditions, molecular diffusion is a dominant process and motion and transport is no longer strictly defined by the electric field and inertia alone. Simulations show, that the ions injected into the device can be turned around by collisions and move backwards towards the entrance for a significant portion of their trajectory. Therefore, beam envelope equations are of limited use when applied to this problem.

Assymetric Simple Exclusion Process (ASEP)

On a most fundamental level, the transport mechanism of ions passing through the ion cooler can be approximately described as the stochastic Assymetric Simple Exclusion Process (ASEP). This process is founded rigorously in a background of stochastic theory.

The ASEP is defined as a Markov stepping process, where time dependent steps are performed on an integer lattice with exponentially increasing probability, that have a higher, thus asymmetric, probability to step in one direction over the other causing a movement bias, or flow, towards that direction.

Additionally, if a targeted position is occupied, the step cannot be performed. This exclusion of certain steps makes this process unique and also turns it into an excellent candidate to be a stochastic description of many transport processes including ion transport statistics. This is because, when Coulomb repulsion is considered and as repulsion grows dramatically for short distances, it effectively means multiple ions are forbidden from occupying the same position at the same time.

While only few real insights about the true, dynamic behaviour of ions and their space charge effects can be obtained from this description, one of the main results of evaluating ASEPs is the connected Tracy-Widow distribution. It resembles a normal distribution with a

tail, as can be seen from the figure shown in 2.9 [53]. Most measurement data from ILIAMS related to ion transport statistics present themselves in this distribution.

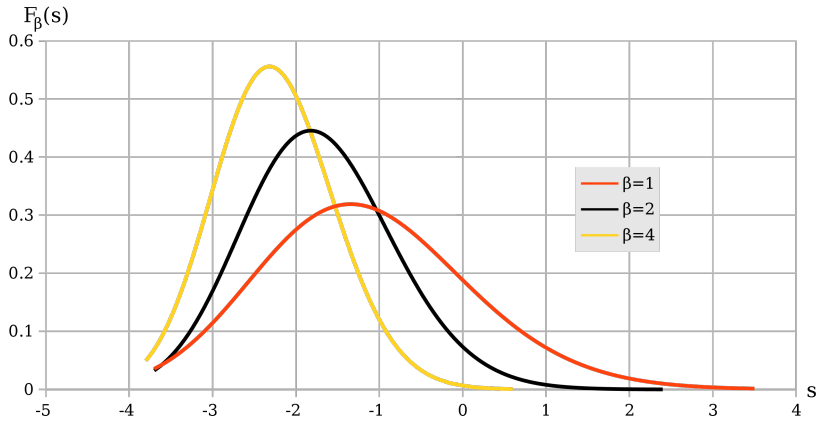

Figure 2.9: Plotted distribution functions for the Tracy Widom distribution for different parameters

Tube Method

Another possible and easily justified approximation that can be used to make better predictions about the dynamic behaviour of space charge, is the assumption of homogeneously dispersed charges, self-ordering into an equilibrium distribution where their Coulomb and kinetic potential is minimal, readily accompanied by maximally equi-distributed and short ranged forces. As a result, the calculation of statistics of a coulomb gas in equilibrium can be approximated through truncation of these forces [54].

In a similar manner, the detail of the assumed homogeneously distributed ion cloud can be further reduced to a continuous charge distribution in the geometric shape of a cylinder, or tube, along the axis with radius r_s. The electric field of this configuration and resulting effects on particle trajectories are comparatively easy to calculate and can be integrated into the established framework for setting up RFQs with Mathieu equations making macroscopic predictions about ion behaviour possible [55].

In this tube method, the number density of charges within the cylinder correlates directly with the beam current I and is inversely proportional to the particle velocity v. This results in a stronger electric field and therefore space charge effects for increasing currents or decreasing particle velocity. From this, an equilibrium state equation (eq. 2.5) can be found by balancing the effects of harmonic particle confinement on the left, with space charge and thermal RF heating effects $k_B T$ on the right [56, eq.2.3].

$$\frac{2e^2 r_s^2 V_{RF}^2}{m r_0^4 \omega_{RF}^2} = 2k_B T + \frac{eI}{4\pi\epsilon_0 v} \tag{2.5}$$

Equation 2.5 can be rewritten into equation 2.6, showing the relation to the Mathieu parameter q (eq. 2.2):

$$q^2 \cdot \frac{m\omega_{RF}^2}{8} \cdot r_s^2 = 2k_B T + \frac{eI}{4\pi\epsilon_0 v} \tag{2.6}$$

The relation can be used to account for the effects of space charge and temperature in an RFQ cooler. If the configuration of the electric RF–Quadrupole field is not changed and considered constant, the only changing variables are the beam radius r_s, temperature T, beam current and particle velocity. If the temperature does not change significantly and is assumed constant, then the following dependency can be assumed:

$$r_s^2 \propto I/v$$

This postulates the quadratic increase of beam size for increasing beam current or decreasing particle velocity. A slowed down particle bunch, or increasing particle number causes wider beams. Faster particles remedy that at high currents by lowering ion density but for the photodetachment process to work, the ions have to move slowly and highly confined. This relation exactly describes the problem ILIAMS seems to have because the only way to achieve slow, tightly confined ions is with low ion currents when using similar RFQ settings.

Hypothetically, increasing I and decreasing v linearly leads to a quadratic increase of the term on the right-hand side, which could be compensated by an increase of $\frac{V_{RF}^2}{\omega_{RF}^2}$ on the left-hand side, essentially increasing the q-value of the RFQ, or the Temperature T on the right-hand side, as also proposed by [45, 46]. However, both increase the effect of RF-heating, where ions can gain energy from the RF-field after being out of phase after a collision and thus, lead to additional, undesired phenomena in real experiments. While this presents the limits of this model equation as a predictive aid, the basic idea of this approach is valid, and a stronger amplitude and shorter RF cycle could potentially allow for compressed ion beams at higher currents.

The idea behind the formalism approximating the distribution of charges inside an ion beam as uniform, is also a basic assumption of the "arbitrary force tests" in section 6.1. There, the uniform distribution is assumed to cause a time-averaged constant distance between ions and therefore constant force acting in forward and outward direction. Forces in other directions are cancelled out by the symmetric and uniform distribution of the ions. The results of these simulations were in good agreement with experimental results and show the same trend towards shorter residence times for higher currents. So, even though the formulas give inaccurate results, simulations with similarly basic assumptions prove to be encouraging.

2.3.2 Difficulties

Conclusively, even though all these models do great work to explain the phenomenology, none explain the experimental data or operation experience to a satisfying degree. Thus, they are considered to be mainly a shallow grasp on the entirety of processes taking place inside ILIAMS, where the full mechanism is suspected to be much more complex and consists of a multitude of interwoven effects, especially considering the apparatus is more similar to a chemical reaction cell than an ion optical device. This requires a more detailed consideration of all processes taking place within the apparatus, but increasing the details and reducing

approximations to account for individual particle interactions and physical effects quickly leads to a large number of equations that are increasingly difficult or even impossible to solve analytically.

This necessitates the use of numerical calculation using computer processing power. They are of especially great value for particle beam physics, as they can compute the large number of equations of motion for the individual particles very quickly and impose additional boundary conditions without much impact on solution time. They can effectively imitate the real world and can help make predictions or give insight into otherwise unsolvable problems enabling a most direct approach. Therefore, designing a simulation seems to be an important step towards understanding the space charge effects inside ILIAMS.

3 COMSOL Multiphysics®– Theory and Methods

Simulations have always accompanied the development of ILIAMS. The simulation software SIMION®was used to optimize the geometry and solve many problems regarding the ion optics or the buffer gas interactions [17, 18, 57]. To get an improved understanding of the buffer gas distribution and the movement of the ions therein, a model of the cooler was created in COMSOL®Multiphysics [1].

COMSOL®Multiphysics is a physics simulation software suite containing all the tools necessary to create and run extensive physics simulations. The equations describing the various laws of physics are solved numerically via different solvers and fields are calculated using the Finite Element Method (FEM). A general overview and a basic introduction to the typical workflow of creating a model within COMSOL and performing a simulation and study shall be given in this chapter. The extensive *COMSOL Multiphysics Reference Manual* is also given for reference in [58].

3.1 Finite Element Method

Many problems in physics are difficult to solve because analytical solutions are often only available for simplified, idealistic initial conditions or geometries such as perfectly straight conductive wires or spherical problems and even then, further approximations are made such as ignoring air resistance or dependencies on temperature or pressure. In reality, geometries are more often than not very complex, not in a vacuum, and many different initial conditions and coupled variables are distributed throughout it.

Approximations of any kind are popular and widely used throughout physics. Instead of trying to find adequate approximations to obtain an analytical solution to a problem, numerical calculations using the equations that precisely describe the changes of the dependent variables in a system, the differential equations of the related physics, in combination with a sufficiently realistic combination of initial and boundary conditions can be used to find a solution approximating the real result to a high degree. Even though still being approximations, the results of these numerical calculation methods yield most accurate results and can, in addition, often be tailored, or scaled as desired, to have increasing accuracy at the cost of computational time and resources.

While mathematics has no problem with the concept of irrational numbers, computers can only ever calculate finite, discrete numbers because of the physical background processes handling the calculation. They can therefore only ever approximate a continuous function by using discrete points in very small distances. Hence, the computation of continuous fields needs

to have a special discretization algorithm, mapping analytical continuities to numerical discreetness, so that a computer can solve for them using tailored methods. COMSOL®Multiphysics achieves this task using the Finite Element Method (FEM).

The finite element method uses the "weak form" of differential equations, generated by integration over the multiplication of the differential equation with a test function and a set of basis functions to asymptotically approach a continuous function via linear combination. The differential equation over the entire model space is broken into a finite dimensional system of equations. Which set of basis functions and in which way they are used to approximate the real function is defined by the discretization method [59].

The possible discretizations are dependent on the dimension of the problem. The entire space that a solution is searched for needs to be partitioned into disjunct mesh elements that provide the nodes and edges the various discretizations can apply their basis functions between and along. As every dependent variable is then present at every mesh node, their product gives the total number of unknown variables, or Degrees of Freedom (DOF), within the model and can be used as a measure for the required computational resources and calculation time.

Finally, the entire problem can be written as a system of equations and represented in matrix form where the matrix of coefficients, or system matrix $\boldsymbol{A}$ and the vector of solved-for-variables, or unknowns x together with a side vector b uniquely define the problem via equation 3.1. The matrix $\boldsymbol{A}$ is typically sparse as only overlapping test and basis functions contribute to non-zero entries.

$$\boldsymbol{A}x = b \Longleftrightarrow \boldsymbol{A}^{-1}b = x \tag{3.1}$$

The system can be solved via different iterative or direct approaches, all essentially sharing the goal of finding the inverse of $\boldsymbol{A}$. They are more precisely discussed in section 3.2.5.

Time dependent problems use an adapted "weak form" equation where time dependent coefficients modify the original equation but the test and basis functions remain time independent. The method of lines, a simpler discretization scheme, is used for the function of time dependent coefficients which yields two calculation methods:

- An **implicit method** solves the full system of equations at one point in time, then advances to the next. The size of the time steps can be comparatively large as the entire problem is solved at each given step and the values in between can be interpolated.

- An **explicit method** is an equation that directly yields the solution for the following time steps, from the previous ones, but is only stable for comparatively small time steps [59].

Modern time stepping/marching schemes can automatically choose the appropriate time step length and switch between implicit or explicit methods depending on the problem.

COMSOL enables the creation of a FEM simulation in a well defined number of steps and the general process structure is the same for every model resulting in a distinct workflow.

3.2 COMSOL Workflow

3.2.1 Component and Dimension

At first, a blank component is created in any number of space dimensions between 0D and 3D. 0D or 1D problems are very restrictive, fairly specific and often purely mathematical in character.

Some real-world 3D problems can be simplified to fewer space dimensions when accounting for symmetries, which reduces the required computational cost and calculation time. For example, heat transfer through a rod or beam can be reduced to a 2D or even 1D problem if the heat distribution is symmetric over one length of the real 3D object. The predictive strength of a dimensionally downscaled model is dependent on the specifics [58, p.155-157].

To simulate space charge effects in a gas filled RF quadrupole, a 3D model is needed and reduction to lower dimensions is not possible as the underlying problem is strictly dependent on all four dimensions and totally non-symmetric. A linear quadrupole cannot be reduced to 2D and while it is possible to simulate linearly propagating particles on a plane, oscillating from the effect of an orthonormal, time periodic, electric field, they cannot be confined towards an axis, as the particles initial momentum is only disturbed periodically and any changes average out. Additionally, energy loss and scattering from the buffer gas collisions are nonphysical in lower space dimensions.

3.2.2 Geometry and Material

After creating an environment in the correct dimension, a geometry must be constructed. COMSOL supports importing a CAD model as well as creating one in the software using typical, primitive shapes and operations such as rotation, mirroring, extruding, sweeping and difference.

The FEM needs a geometry to locate and fix points, edges, boundaries or domains in and to a coordinate system and then further to apply the functions and boundary conditions. Geometries are typically in a Cartesian coordinate system, but cylindrical, radial or shifted systems can easily be defined.

Each domain needs to have a material assigned to it. Materials provide numerical values corresponding to the physical attributes or real world properties usually represented by constants in equations. Those values are used in place of the respective variable in the equations compiled in the solving step. Materials and their physical properties can be added from a data library provided or can be individually defined with specific properties as needed.

3.2.3 Physics

Once a geometry exists, a physics module needs to be added to the environment. Different main groups of physics consisting of many sub-modules are available and can be chosen as needed and various couplings are available as well, to account for interacting physics.

The physics modules supply the FEM with the necessary equations and boundary conditions as well as a discretization method. Each module has different typical conditions that can be applied to domains, boundaries, edges, or points to set boundary conditions and fix the

physics in these locations in the coordinate system. The methods of discretization that are available are dependent on the physics in the model. One way to increase the accuracy of the simulation at the cost of calculation time is to change the discretization method so that a higher number and higher orders of base functions are available.

3.2.4 Meshing

The process of partitioning a geometry into the mesh elements is defined in the meshing step. While for one dimensional models this break-up is a separation into intervals, the number of possible element shapes increases for higher dimensions.

For two dimensions, the element or vertex shape can be triangular or quadrilateral. When applied as a boundary mesh for 3D geometries, they can be swept along a domain to create a "swept mesh" of regular prisms. While tetrahedrons are the default shape for 3D models, hexahedrons are also available, and pyramid elements are automatically created whenever necessary. Triangular or tetrahedral shapes can fairly easily be used to evenly divide any shape while providing a large number of vertex points per area or volume. Quadrilateral or hexahedral shapes provide more nodes per element and, while they are more memory expensive, are particularly appropriate in geometric regions with many orthogonal edges or symmetry in one direction.

The size and shape of the elements greatly influences the simulation result, as smaller elements lead to a tighter web of nodes, further refined by the order of discretization, thus enabling a closer approximation of the real function, while increasing the computation time and resource cost due to the larger size of the system matrix, higher number of variables and DOFs solved for.

An automatic, "physics-induced" mesh is created per standard via a COMSOL algorithm. Meshes for simulation of plasma physics are typically a lot tighter than general purpose physics meshes and fluid-dynamics simulations induce a mesh that has a number of layers along the domain boundaries to better resolve the wall interactions relevant for these calculations. The set boundary conditions are also accounted for, when an automatic mesh is generated. A nine stage setting enables the selection of global element size from an extremely coarse to extremely fine mesh. Because meshes have great influence on the calculation time it can be useful to manually design a mesh or optimize the automatically generated one for a particular purpose.

The automatic meshing algorithm provides a mesh that is globally of equal quality. In certain cases, however, the simulation result only needs to be precise in certain areas so a finer mesh can be specified in these areas while a coarser mesh is used in others. Also, different element types can be chosen for different meshing areas and other attributes can be added such as varying distribution of element size within a meshed domain and corner refinement, as too coarse meshing around sharp, small corners can lead to nonphysical computation.

COMSOL can analyse the mesh statistics such as mesh volume, mesh element quality and the number of the various types of mesh elements to compare different meshes. Mesh element quality can be evaluated on skewness, growth rate or maximum angle of the element and a histogram depicts the quality distribution (see Appendix fig.A.10).

3.2.5 Study and Simulation

Once the mesh is set up adequately, the solving sequence has to be configured. In COMSOL, each solving sequence is integrated into a "study", consisting of a row of solver steps of which "*Stationary*", "*Time dependent*", "*Time periodic*" and "*Eigenfrequency*" are generally the most applicable. For any available model setup, COMSOL proposes standard studies and generates the corresponding solving sequence automatically. Additionally, the entire sequence can also be modified or built from the ground up to be optimized or fit special needs.

The solver sequences each belong to a solution with a certain number in COMSOL. In general, the first steps are to compile the model equations for computation, and the definition of the dependent variables that should be solved for. It is also possible to not solve for dependent variables, but take their values from previous solutions. Other operations such as copying or combining solutions from different parts of the sequence are available, and "for loop" programming can be added to design an iteration-limited solving sequence. The most important step, however, is the solver itself.

Two major pathways are available to solve the system of equations. The *segregated solver* splits the problem into separate systems of equations by their dependent variables, solves for them individually and finally compiles them according to defined convergence criteria. While this usually saves memory and is more robust, there is also a higher chance of not reaching convergence of the variables at the end. On the other hand, a *fully coupled solver* solves the entire system of equations for all dependent variables at the same time, often resulting in a higher chance of convergence at the cost of computational resources and speed. For complex models with many DOFs and 3D models typically the segregated solver is suggested while the fully coupled solver is suggested whenever possible.

The solving algorithms themselves can be separated into direct and iterative methods. A *direct method* generates one large system matrix from the compiled equations that then is inverted via matrix operations to find the solution. This is a method with a very high chance of convergence but is again only viable for models up to a certain size, because not only does the entire system of equations, all DOFs, need to be fed into one matrix simultaneously, but all reordering, pivoting, and factorization operations also take space in the working memory (RAM) of the computer which can quickly blow up and surpass the typical limits of single workstations. Different algorithms are available for direct solving like MUMPS, PARDISO, SPOOLES or via a density matrix.

An *iterative method* solves the system of equations iteratively. At first, a preconditioning algorithm does the initial work of reducing the complexity of the system to make the subsequent iterative solving method faster and more likely to converge. "Incomplete LU", "SOR", "Vanka" or "Krylov" preconditioners are often used. The preconditioned matrix is then solved with an iterative solving method such as "Generalized minimum residual" or "Conjugate Gradients". The process is repeated until a predefined threshold is reached.

A full framework for iterative solving, that can be used as a preconditioner or full solver, is provided by the multigrid methods, which take a slightly different turn on the problem and not only precondition the given system, but also try to automatically find the system of equations that is sufficiently easy to solve and minimize problem complexity by coarse solving, evaluating and changing the system so the minimal problem size for a given accuracy setting

is found.

Many iterative solving schemes are available each with certain benefits and disadvantages and some can only be used for certain physics. Control settings enable the steering of the iterative process, how it handles divergences, when to restart and when to terminate. Every solving algorithm in general can be fine-tuned using a multitude of settings to optimize the computation.

3.2.6 Data Evaluation

After the computation is finished and the problem is solved, the solution is linked to datasets to be evaluated and viewed within COMSOL's data evaluation and result section. Any expression, for example electric potential or particle position, can be presented in a multitude of ways such as surface or volume plots, streamlines and arrows with a variety of design settings to best visualize the data. Multiple plots can be combined in a single plot group to be viewed on top of each other and translation operations can move the plotted data to enable direct comparison of 2D or 3D data.

Also, global data evaluation of single expressions can be done and exported into a table or plotted as a line graph over time or other parameters just as well as specific data points can be accessed. Datasets can be joined, integral or average operations over time or over the domain can be performed or filters can be set to only include data from certain domains or areas. Definable cut planes or cut lines limit the data evaluation to these set dimensions.

For particle simulations, an important subset of data is the particle dataset. It enables the evaluation and presentation of particle positions and trajectories, as well as their properties. In a particle trajectory evaluation, individual particles can be represented as points, and trajectories as connected lines between locations over the past times, while properties such as velocity or kinetic energy can be visualized via a colour legend.

3.3 Computing Resources

Crucial hardware resources for computation in COMSOL are the Central Processing Unit (CPU) and the Random Access Memory (RAM). The CPU is responsible for the calculations and operations on the data stored in its operating cache, which is directly exchanged with the RAM. The fast RAM caches the data the system is directly working and operating on and is responsible for storing the compiled system matrix when it is being solved. In certain cases, an overflowing RAM can be outsourced to the hard drive, and intermediate solution data or other temporary files are saved there as well. Thus, a fast hard drive such as an SSD should also be available.

An already existing workstation was used for the first simulations but was in a later stage replaced by a newer machine, which was optimally designed for the task of simulating space charge. The new CPU, an AMD Ryzen Threadripper PRO 5975WX, was the third best CPU at the time according to several rankings and the 128 GB RAM with 3200 MHz was the fastest available for that CPU. It is capable of more than 10 times the FLOPS of the old machine, even though the base frequency is lower. It has larger caches for storing operations and data

directly on the chip and possesses 32 cores, while the old CPU only had 4. That does however not automatically mean that computation happens faster, as the effect a larger number of processing cores has on the computation speed depends on the problem. Some tasks are more easily distributed over multiple processors, while others can only be computed on a single core. It also depends on the coding of the program, as it needs to be optimized for parallel computing.

COMSOL supports multi-core computing, where the computation is distributed over a CPU that has multiple processing cores. It does, however, not support multithreading, which is a technique that splits the processing power of each core further into logical processors. The computer recognizes this capability and attributes more processing power to it which COMSOL does not access so it does not register as using 100 % of the CPU while computing. Still, some tests show that the newer CPU computes around 3-4 times faster than the older one.

For fast memory access time, an SSD is used for active simulation projects in each of the computers. Because simulations can be quite memory intensive and in the hundreds of gigabyte range, the 1.5 TB SSD can run out of space quickly. The second machine therefore has a 12 TB and a 4 TB HDD as archive drives, in addition to the 2 TB and 4 TB SSDs. Full details on the computational resources used can be found in the appendix (A.8).

4 Simulating Space Charge with COMSOL

Simulating space charge in a buffer gas cooled RFQ is a multi-physics problem. The static electrical field from the guiding electrodes and the alternating RF field from the quadrupole rods have to be simulated with proper grounding to correctly affect the ions' trajectories, just as well as the right gas number density distribution through the device needs to be considered to correctly account for the collisions with the buffer gas.

While all this can be simulated comparatively easily and realistically using only slight approximations, computing space charge accurately adds considerable complexity to the problem, since the electric field can no longer be assumed constant in time or frequency domain and particle movement becomes much more dynamic.

Nevertheless, COMSOL offers ample architecture and proper tools for the simulation of space charge.

4.1 Core Model Simulation Setup

While there are many different approaches for simulating space charge in COMSOL that require different configurations, it is not necessary to build an entire model from the ground up for each of them. A simulation model that correctly represents the geometry and simulates all physics not directly related to space charge has to be set up properly to serve as a basis for further investigations into the space charge effects within a model. Also, various approaches can then be compared more directly.

A core model for a buffer gas RFQ ion cooler with guiding electrodes needs to simulate the electric field generated by the device itself, as well as handle the particle dynamics.

4.1.1 Electric Field Simulation

The *Electrostatic (es)* module and the *Electric Current (ec)* module are part of the *AC/DC* COMSOL package and offer fairly similar physical equations, boundaries and discretization methods. Both modules are needed to simulate the electric field configuration of an RFQ with guiding electrodes.

A quadratic discretization is sufficiently detailed for most model problem formulations. A tight mesh over the geometry should be used for precise results, especially around corners, edges, curves and towards sources.

The stationary electric field is solved using the Finite Element Method (FEM) on the common differential equation form of the eminent Maxwell equations. As there is no relevant magnetic contribution, the differential equation for the electric field $\boldsymbol{E}$ induced by an electric potential V is given in equation 4.1 while the gradient of the electric displacement field $\boldsymbol{D}$ is given by the charge density ρ_V via equation 4.2:

$$\boldsymbol{E} = -\nabla \cdot V \tag{4.1}$$

$$\nabla \cdot \boldsymbol{D} = \rho_V \tag{4.2}$$

For electric currents, correspondingly, the electric flux density $\boldsymbol{J}$ joins the set of equations and is defined from $\boldsymbol{E}$ via a material-dependent conductivity σ and an external current density J_e via equation 4.3 and also represents a continuity equation with current source $Q_{j,v} = \partial\rho/\partial t$ via equation 4.4:

$$\boldsymbol{J} = \sigma\boldsymbol{E} + J_e \tag{4.3}$$

$$\nabla \cdot \boldsymbol{J} = Q_{j,v} \tag{4.4}$$

Boundary Conditions – Set Voltages and Currents

The boundary conditions used are *charge conservation* (eq. 4.5 & 4.6) over the entire domain and a general *zero charge* and *insulation* on the outermost boundaries (eq. 4.7 & 4.8), which are overwritten by other boundary conditions like *electric potential* source terms. Initial conditions can be a set electric potential of defined voltage or charge in a defined domain or boundary.

$$\boldsymbol{D} = \epsilon_0\epsilon_r\boldsymbol{E} \tag{4.5}$$

$$\boldsymbol{J_C} = \sigma\boldsymbol{E} \tag{4.6}$$

$$n \cdot \boldsymbol{D} = 0 \tag{4.7}$$

$$n \cdot \boldsymbol{J} = 0 \tag{4.8}$$

To simulate the electric field inside the device, the potentials and grounding have to be set correctly on the corresponding boundaries. The *Grounded* and *Electric Potential* boundary conditions are essentially Dirichlet type boundary conditions that keep the field value constant at zero, or another set voltage value respectively.

The guiding electrodes and deceleration or acceleration lenses thus have an "electric potential" boundary condition that holds the voltage constant corresponding to the real world device. As the field does not change over time, the *Electrostatic (es)* physics module and a stationary solver is used.

The RF rods are powered by an alternating current. The *Electric Currents (ec)* physics module uses a set impedance to form equations in the complex domain, which can then be solved quasi-stationarily in the frequency domain for a given frequency. The electric potential boundary condition sets the voltage amplitude and the grounding has to be separately set in the *EC* physics module again, identically to the *ES* module. The two modules are solved separately and generate two different solutions for their individual dependent variable for the electric potential (V and $V2$).

Because fields can be superimposed, their combined effect on particle motion can be simulated by addition of the individual electric forces.

4.1.2 Charged Particle Simulation

Particle motion can be simulated in COMSOL with the particle tracing package. Various modules like purely mathematical particle tracing, particle tracing in a fluid, liquid droplet tracing or charged particle tracing (cpt) are available.

As we are interested in the behaviour of ions, or more concretely anions, which are per definition charged particles and affected by electric fields, the latter is the most suitable option.

Using the Newtonian formulation, the Newton differential equation of motion (ODE) given in 4.9 is solved for each individual particle at every time step. There, for a particle of mass m_p, the acceleration, or change of its velocity v, is only dependent on the total of forces $F_t = \sum_i F_i$ acting on it.

$$\frac{d[m_p v]}{dt} = F_t \tag{4.9}$$

Special cases are the Newtonian first-order approximation, where the above ODE with second-order component (eq. 4.9) is expressed as two coupled first-order ODEs, or a massless formulation where solely the position derivative is given by $\dot{q} = v$.

Alternatively, the motion can be expressed via the Hamiltonian or Lagrangian formulation where the Hamilton or Euler-Lagrange equation are solved respectively. For these, however, the full analytical description of particle motion and involved potential has to be known in advance and included in the equation and it does not allow for interactions between particles.

Particle tracing within COMSOL is not solved via a FEM. The position and velocity parameters of a particle are scalars or vectors with scalar components that do not need to be discretized over mesh nodes. The equations of motion within cartesian coordinates can be solved directly and meshing is only important when considering interactions with fields, or boundary walls in the geometry. These sections need to be meshed finely to accurately simulate the interaction behaviour. Further, the time needs to be discretized which is typically done by an automatic time stepping algorithm but a maximum step size can be set if necessary.

Multiple particle types can be defined via a *Particle properties* node that defines their mass and charge.

Particle Release

Particle initial conditions can be defined in various ways with different types of inlet nodes. They can be released with uniformly, randomly, mesh-based or density based distribution from a boundary with fixed initial energy and direction, or velocity vector, or even sampling from a 4D distribution, such as Gaussian, KV, Waterbag or Parabolic, to correspond to the statistics of an ion beam with specified phase space ellipse dimensions or Twiss-Parameters and emittance. They can also be released from a data file, or a defined grid with initial energy

and direction or velocity.

The **particle release type** specification is a core setting for the module. Two different pathways are available and affect what equations are used and alter how the problem is defined:

- *Specify release times*: Initializes a set number of particles via one of the various release methods for any range of specified release times. This can be used to simulate a stream, or continuous particle beam, as at each of the time steps a certain number of particles is initialized in the simulation similar to a real particle beam, where a discrete number of particles enters a volume per time, only averaging to a current over time. Therefore, releasing a number of ions ΔN with one elementary charge e in very short intervals Δt to the simulation is the most realistic approach to simulate a beam current $I = \frac{\Delta N}{\Delta t} \cdot e$.
- *Specify current*: Initializes a set number of particles at $t = 0$ at the release, similar to the previous method but without the option of adding other particles at later times. They are individually propagated through the simulation the same way as in the previous method but with the difference, that each particle represents a stream of particles $dN^2/dtds$ on the path $S = \int ds$ so that the integral over all streams amounts to a particle beam of a given current. This is useful because it uses few resources to simulate beam optics of a particle beam of any scaled current and is efficient in purely ion optical situations where ion trajectories are approximately the same for all consecutive ions independent of beam current.

Boundary Conditions – Walls, Forces and Collisions

The charged particle tracing module offers many boundary conditions and other options to affect, restrict and analyse the particle dynamics.

Per default, the outermost boundaries in the geometry are defined as *wall*, where the particles are scattered, frozen or removed from the simulation on interaction. Further, they can be defined as accumulators to count the particles in the boundary or the particle-wall interactions and calculate the number density. Combined with the pass-through setting of a wall, particle propagation can simply be quantified by counting the particles moving through an internal boundary plane in the geometry.

The *forces* inferred on the particles via the Newtonian equation of motion 4.9 are a combination of the force features added to the model. Magnetic, electric, friction or general forces can modify the particle motion by adding to the total force F_t in 4.9. Other interactions can infer further forces on the particles, or reinitialize their velocity based on a specified formula.

Particle-particle interactions can be simulated via localized fields, such as Coulomb, Lennard-Jones, linear elastic, or a custom potential, where all particles interact with all other particles excluding ones outside of a defined cut-off distance. *Particle-matter interactions* can be simulated accounting for ionization loss and nuclear stopping as desired.

A "*collision*" feature allows various particle-buffer gas interactions via a stochastic approach. A domain is declared as a volume where interactions take place and a buffer gas number

density and molar mass are specified as well as the cross section of interaction. The most basic case of elastic collision is sufficient for simple gas interaction simulations. Others such as (non-)resonant charge exchange, excitation, ionization, attachment or "user-defined" interactions can also be applied.

Additionally, *auxiliary dependent variables* can be added to track and integrate certain properties for every particle, over time or their trajectory. The most basic application is calculating each individual particle's trajectory path length or lifetime inside the simulation.

For the simulation within an RFQ with guiding electrodes, only the electric force is relevant. Because fields can be superimposed and all force conditions on the particles are summed up to a total force vector in equation 4.9, the model can independently calculate the stationary solution of the electrostatic field of the guiding electrodes and the frequency-domain solution of the time periodic field of the RFQ-rods and the resulting total force on the ions can be attained by the implementation of two separate electric force conditions. For charge number Z and elementary charge e, the electric force F_e from an electric field E is given by equation 4.10.

$$F_e = eZ\boldsymbol{E} \tag{4.10}$$

To account for buffer gas interactions, elastic collisions via the standard hard-shell method, or a modified version using variable hard-shell collisions (see [1, p.12f.]) are added, with the cross section and molecular mass corresponding to a gas of choice. The buffer gas number density, or pressure, follows a real gas distribution determined in earlier works. A 1D function supplies the gas density each particle experiences dependent on the depth in the cooler.

The velocity of the buffer gas molecules in the device v_g is assumed to be distributed according to a drifting Maxwell distribution (eq. 4.11) for a known Temperature T, gas molecule mass m_g and gas drift velocity $\mathbf{u}$.

$$f(v_g) = \left(\frac{m_g}{2\pi k_B T}\right)^{\frac{3}{2}} \cdot exp\left(-\frac{m_g \left|\mathbf{v}_g - \mathbf{u}\right|^2}{2k_B T}\right) \tag{4.11}$$

Sampling from this distribution, the collision frequency ν_j for collision j for a gas with number density n is given by 4.12.

$$\nu_j = n\sigma_j(\mathbf{v} - \mathbf{v}_g)|\mathbf{v} - \mathbf{v}_g| \tag{4.12}$$

The collision probability for constant collision frequency is given by equation 4.13 for a time step of duration t.

$$P(t) = 1 - exp(-\nu t) \tag{4.13}$$

In case of elastic collisions, the velocity after the collision $\mathbf{v}'$ for particles of mass m_p and gas particles of mass m_g is given by equation 4.14, where the relative velocity to the center of mass frame is $\mathbf{g} = \mathbf{v} - \mathbf{v}_g$ and after the collision $\mathbf{g}' = |\mathbf{g}|\mathbf{R}$ with a uniformly distributed random unit vector $\mathbf{R}$ [60, p.192-200].

$$\mathbf{v}' = \mathbf{v} - \frac{m_g}{m_p + m_g} \left(\mathbf{g} - \mathbf{g}' \right) \tag{4.14}$$

4.1.3 Particle – Electric Field Interaction

The tools mentioned so far allow accurate simulation of the effect of gas collisions and stationary or time-periodic electric fields on the ion motion. To simulate space charge, the charge of the ion also has to affect the electric field, or in other words, the charges of the ions have to be coupled to the electric field computation. In COMSOL, this can be achieved by the "Electric particle field interaction" (epfi) Multiphysics module, which connects the charged particle simulation to the electric field computation.

The ion positions are evaluated in the model mesh and each mesh element individually contributes to the overall space charge density, dependent on its volume and the number of ions, or charges, inside it. The resulting charge density ρ_V field then serves as an additional source for the electric displacement field 4.2, computed in the electrostatic module. The resulting electric field then correctly accounts for all electric potentials including space charge. Ions are affected by this field via the electric force and their equations of motion are solved accounting for all electric effects including space charge.

However, when developing simulations with this coupling, some additional considerations have to be made, as opposed to a simple ion optical study that ignores space charge. While the computation of trajectories in purely ion optical simulations with electric or magnetic fields is independent of the number of particles and a higher number of distributed particles is only simulated to better visualize the beam envelope, and while Monte Carlo simulations of ion-matter or ion-gas collisions only need a high number of particles to get better statistics, space charge directly correlates and even scales with the number of ions.

In theory, a simulation with maximal realism would need to simulate the real number of particles, highest order discretization and a mesh element and time step size as small as the computer precision allows. In practice, it is a logistical near-impossibility to simulate while fulfilling even one of the above criteria within the limits of even high-end computational resources. Thus, certain approximations have to be made, but while the meshing quality, discretization and time stepping can be easily simplified and optimized for speed and precision automatically or from experience, the choice of number of simulated particles pertains.

This choice and the specifics of the particle release are therefore of utmost importance when simulating space charge effects. Each particle adds more Degrees of Freedom (DOF) to the problem that need to be solved for and any computational model within COMSOL with more than a million DOFs is considered a complex problem. The tight mesh needed for accurate simulation of the electric field alone causes the number of DOFs to lie in the order of millions before particles are even considered, and while a typical particle simulation generally uses a couple of thousands of particles, even for pA ion beam currents the number of real particles lies in the order of millions every second and for currents in this range the space charge effect is typically not even noticeable. Simulating µA beam currents with the full particle number in the order of trillions is simply not feasible.

To solve this conundrum, several approaches can be taken in COMSOL to approximate a realistic number of particles through a significantly reduced number of DOFs.

4.2 Simulation Approaches within COMSOL

To simulate space charge effects inside the ILIAMS ion cooler, a few things must be considered. Space charge is the effect resulting from particles affecting each other as a consequence of their charge. Naively, one would think that as each particle interacts with every other the problem complexity grows with N^N for a particle number N and would therefore grow quickly out of hand for realistic particle numbers.

Using the *electrostatics (es)*, *electric currents (ec)* (section 4.1.1), *charged particle tracing (cpt)* (section 4.1.2) COMSOL modules and the *electric particle field interaction (epfi)* multiphysics coupling (section 4.1.3), three different, major pathways for simulating space charge effects are realizable in COMSOL, each requiring different model configurations and setups. Relativistic corrections are in general not necessary, as the highest simulated ion speeds are less than $10^{-4}c$.

4.2.1 Coulomb Interaction

One intuitive way to directly simulate space charge is to enable coulomb interactions within the *cpt module*. Using this method, for each particle at position $\vec{r}$ an additional force F component is calculated by summing over the Coulomb interactions between every other particle j at position $\vec{r_j}$ in accordance with equation 4.15.

$$F = \frac{e^2}{4\pi\epsilon_0} \sum_{j=1}^{N} Z Z_j \frac{\vec{r} - \vec{r_j}}{|\vec{r} - \vec{r_j}|^3} \tag{4.15}$$

In this pure form, each particle affects every other particle and the problem complexity thus scales with the number of particles N according to the power law N^N and is only viable for a very limited number of particles. A cut-off distance can be set so that only particles within a certain range are affected. Finding the right cut-off distance can make this method potentially as good as any other in many cases but the complexity still grows with N^N with the number of particles within the sphere around each particle. It also does not compute any charge density field by default which would have to be calculated in a separate, extra step from the number density.

All in all, this method is best suited for small-scale, microscopic simulations of a relatively small number of particles which is why it is not used for simulating space charge effects in the ILIAMS ion cooler.

4.2.2 Charge Scaling – Fully Time Dependent Simulation

One way to approximate a realistic amount of particles without affecting the problem complexity is to assume highly mutual particle dynamics and re-scale the particle problem. It is postulated, that in reality many particles behave sufficiently similar in a proximate neighbourhood and

their behaviour can actually be collectivised around their position. Therefore, one particle can be used as a représentant for a larger, local particle group.

To substitute a larger particle number when simulating space charge, the charge of each of these *macro particles* has to be scaled by a *charge multiplication factor* n to represent n real particles. Using the *specified release times* release type (section 4.1.2), in every time step COMSOL computes the full space charge density field from the different charge densities ρ_s, computed individually for each mesh element over the domain. The ions within each mesh element contribute to a local charge density dependent on the sum of ions in each cell, their charge number Z_j, the charge scaling factor n and the internally computed mesh volume *meshvol* according to equations 4.16 and 4.17.

When a particle j enters a domain mesh element:

$$\rho_{s,new} = \rho_s + \frac{eZ_j n}{meshvol} \tag{4.16}$$

When a particle j exits a domain mesh element:

$$\rho_{s,new} = \rho_s - \frac{eZ_j n}{meshvol} \tag{4.17}$$

The resulting charge density field is the present space charge field and serves as an additional source for the calculation of the electrostatic field. This field is used to compute the electric force exerted on the particles and affects their movement for a sufficiently small time step. For the next iteration, the particles' new position generates a slightly different space charge distribution, resulting in a new electric field. This process is the closest possible, dynamic, real-time simulation of particle movement with space charge interaction.

The process is illustrated in figure 4.1. At the beginning of every time step the particle position is evaluated and the number within each mesh element is counted (A). The charge density is then computed according to equation 4.16 and 4.17, and the charge density field is computed via the FEM method (B). Then finally, this charge density field is added as an additional source term for the electric field computation, which is then used to compute the electric force on the particles (C). A short description of the algorithm is compiled at the end of subsection 4.2.2.

This method uncouples the injected beam current and therefore amount of charge present in the device from the number of particles that are simulated and the choice of how many ions are used only depends on the desired quality of the statistics. Any statistically significant number of ions can be used to approximate a space charge field representative for ion numbers, orders of magnitude larger. The ions affected by this field then move accordingly, representing the behaviour of a significantly larger number of ions.

A few things have to be taken into account, however. The method effectively decouples the charge position from the particle position and groups the charges through the mesh elements. This works well for lower charge densities but there is an increasing error for larger charge scaling and larger mesh element sizes. This is because then the charge field is increasingly inhomogeneous and peaked, as more and more charge is grouped into the same mesh element,

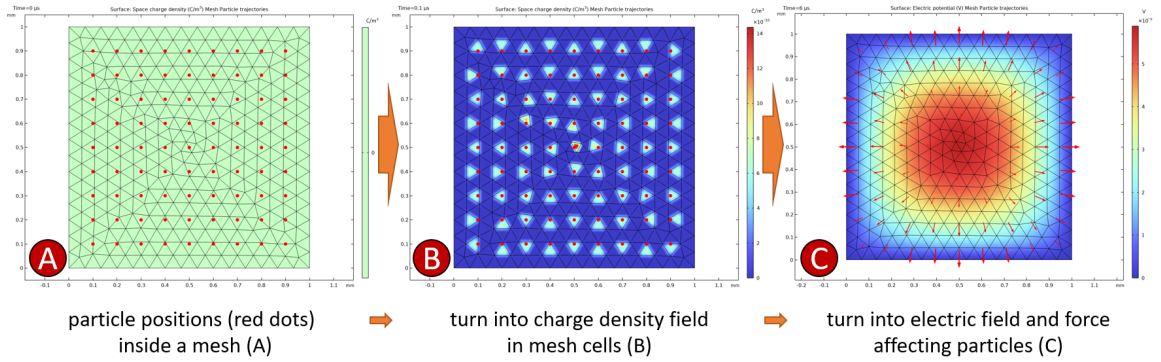

Figure 4.1: Illustration of how fully time dependent space charge simulation works in a 2D representation. First, the ion positions are evaluated in the mesh (A). Then, a charge density field is computed (B). Finally, the charge density field is used to compute an electric field, that is used as an acting force on the ions (C).

resulting in more erratic ion behaviour and force overestimation. This can be remedied by either decreasing charge scaling while increasing the number of simulated particles, or a mesh refinement.

To illustrate the problem, consider a system of N ions with charge q that will self-distribute into a field of homogeneously dispersed charges with a certain mean equilibrium distance if N is sufficiently large. A smaller fraction of the particles $\frac{N}{a}$, each with charge $a \cdot q$ amount to the same total charge but will self-order into a less ordered, more inhomogeneous field with larger equilibrium distances due to stronger Coulomb forces between them.

Thus, exceptional care has to be taken when choosing the number of ions and charge scaling factor in combination with mesh element size, as it not only defines the quality of the Poisson statistics, but may also result in incorrect particle dynamics or a breakdown of the approximation method.

As the entire electrostatic field needs to be recalculated in each time step, the entire computation takes significantly longer compared to a pure particle dynamics simulation. Increasing tolerances or step size are common practices to increase computation speed but are not viable in this situation. Only low error-tolerances resolve the intricate inter-particle field physically correctly in the space between particles and short time steps ensure the dynamically accurate representation of the interaction processes.

Fully Time Dependent Algorithm

1. Initialize new particles if the current time step is a specified release time step
2. Compute space charge density from particle positions and scaled charge
3. Add space charge field as an additional source for electric field computation
4. Compute electrostatic field

5. Solve equations of motion with electric force contribution for each particle

6. Advance one time step and repeat

4.2.3 Cumulative Space Charge Density – Bidirectionally Coupled Particle Tracing

Because calculating via the fully time dependent approach typically takes a substantial amount of time and computational resources, it is not always viable for all simulation problems. Instead another, less demanding method can be used to get a very good approximation for the distribution of space charge in most particle tracing problems.

In this method, N particles of charge number Z are released in the *specify current* mode, where each ion and the corresponding trajectory represents a number of ions per time so that the entire ensemble amounts to the specified beam current $I = NZet^{-1}$ with elementary charge e, similar to the *charge multiplication factor* of the Fully Time Dependent method in section 4.2.2.

First, the full ion trajectory is computed in the pure electric field, free from space charge. Using this trajectory data, the true-scale charge density flux $\dot{\rho_s}$ corresponding to an ion beam of specified beam current can then be attained for each mesh element by calculating the individual contribution of simulated ion i using the charge $Z_i e$ and frequency of release $f_{rel,i} = \frac{I}{|Z_i e|N}$ tied to it, summing over the number of simulated ions within the cell N_j and dividing through the mesh element volume *meshvol* as seen in equation 4.18.

$$\frac{\partial \rho_s}{\partial t} = \sum_{i=1}^{N_j} \frac{f_{rel,i} e Z_i}{meshvol} \tag{4.18}$$

This first-order equation is then used to acquire the stationary space charge distribution. The electric field resulting from adding this charge distribution is then used in another particle simulation run, in a way imitating a real, dynamic, ion stream by effectively letting ions fly through the field left behind by the ions in front of them. Consequently, iterating this process leads to a convergent space charge distribution for many ion optical problems, where the effect of space charge on beam shape, size and divergence is of the greatest interest.

Because solving the Newtonian equation of motion and handling motion even for a large number of particles is significantly quicker to compute, than computing a high resolution electric field, this method is substantially faster than the fully-time-dependent method, because it computes the electric field only once for every particle trajectory simulation, instead of for every time step.

However, while this method works very well to predict problems, where space charge effects dominate in lateral and radial directions, the prognostic accuracy in axial direction is limited. Because the electric field is always stationary and does not change during an iteration, any accumulation of space charge leads to a stationary potential well. The slowing of ions leads to an increased number of space charge in a region and ions that are slowed down by the potential well can therefore deepen, widen or shift the existing potential well for the next iteration. This can be the natural way of convergence and lead to the real space charge distribution, but can

in some cases lead to nonphysical behaviour or cause the simulation to diverge by disrupting the ion trajectory too much. Especially when simulating relatively low ion speeds and high currents, space charge can easily be overestimated using this method. To deal with this, a slightly adapted version of this method can be employed.

Enabling *cumulative space charge density* changes the algorithm so that it no longer uses the full-scale space charge density computed from equation 4.18 for computation of the electric field, but instead slowly accumulates towards the final space charge distribution with increasing proportional weights in every iteration. In β iterations of a *ramping up* phase, the space charge density field for the next iteration is computed as average $\bar{\rho_s}$ over the previous distribution $\rho_{s,\bar{prev}}$ and the current one ρ_S according to equation 4.19. When the iteration number $iter > \beta$, the actual *cumulative averaging* begins via equation 4.20 for an increment $i = iter - \beta + 1$ using weights w_j that can be distributed uniformly ($w_j = 1$), arithmetically ($w_j = j$) or geometrically ($w_j = r^j$ with common ratio r).

$$\bar{\rho}_s = \frac{\bar{\rho}_{s,prev} + \frac{iter}{\beta}\rho_s}{2} \tag{4.19}$$

$$\bar{\rho}_s = \frac{\left(\sum_{j=1}^{i-1} w_j\right)\bar{\rho}_{s,prev} + w_i\rho_s}{\sum_{j=1}^{j} w_j} \tag{4.20}$$

Setting the right β and choosing a weight sequence that grows not too abruptly can reduce the probability of space charge overestimation at the cost of an increased number of iterations. This, however, limits the practicability of this method due to an unreasonably high number of iterations to achieve a convergent solution. Additionally, the stationary nature of this method limits its applicability to highly dynamic problems, such as chemical transportation, diffusion-dominated systems, or other processes where charge repulsion has immediate, large-scale effects on the particle motion, and no averaged, stationary field exists.

Iterative Partially Stationary Algorithm

For a set number of iterations I, a set value of ramping up steps β and a current iteration number *iter* do: While $iter \leq I$:

1. Compute electric field $\mathbf{E}$, respecting the space charge density ρ_s of the last iteration
2. Compute full particle trajectories with applied electric force from the $\mathbf{E}$ field
3. Compute space charge density field ρ_s from the trajectories using the specified beam current I
    - *cumulative averaging*: compute average space charge density $\bar{\rho}_s$ from current ρ_s and previous $\bar{\rho}_{s,prev}$

- using equation 4.19 if $iter \leq \beta$
- using equation 4.20 otherwise

4. Advance iteration number *iter*

4.3 Simulation Models

To exploit the various intricacies of the simulation methods available in COMSOL®Multiphysics, they are explored in two different geometries and simulation models. A *full model* geometry allows space charge simulation within the highly detailed ILIAMS model but for limited simulation periods, while a *simple model* was developed with the idea to have the possibility to do fully time dependent, full transmission studies of space charge effects in a basic geometry.

4.3.1 Full Model

The already existing, full-scale model of the ILIAMS setup used in previous, extensive collision and buffer gas studies, can be very easily modified to account for space charge density calculation and bidirectional coupling of particle tracing and electric field. A 3D model of the injection/entrance section and early drift section of the model can be found in figure 4.2, and the respective 2D cross section in figure 4.3. The majority of the entire cooler length is composed of the drift section surrounded by the RFQ rods (blue/orange) and guiding electrodes (violet) and the entrance and exit section are essentially mirrored. A very-high-resolution mesh is employed for the computation of the RF field in the frequency domain, which is not recalculated in the time-dependent simulations. For these, another mesh is created, which has a very high concentration of mesh elements in the particle area within the inscribed radius of the RF-rods and a normal to lower resolution in the surrounding. Also, mostly tetrahedral elements are used, as an otherwise useful, swept mesh consisting of lengthy hexahedrons in axial direction imposes a large shape bias to the field. The simulation of space charge generally requires a fine mesh in the area particles move in, as it needs to be sufficiently tight to accurately represent the small and close changes of the field due to the charge of a potentially dense ion cloud.

Instead of the simpler *elastic collision* condition that simulates hard shell scattering, the *full model* applies the more sophisticated Variable Hard Sphere (VHS) implemented in a previous work [1] as a *custom* collision condition, where the scattering cross section is dependent on the ion speed and on empirical collision data. The buffer gas number density is sampled from the distribution resulting from the studies of this work (see A.12).

Additionally, statistical tools like accumulating or counting surface conditions are applied to better quantify particle loss and distribution. An auxiliary dependent variable integrating over the lifetime or path length of each particle can be used to get an understanding of residence time or the length of the trajectories for each individual particle.

Because of the size of the model and more concretely the length of the particle flight, it is unfeasible to do a full simulation through the entire device fully time-dependently. In ILIAMS, ions take several ms to pass through and to have enough ions reach the exit for sufficient

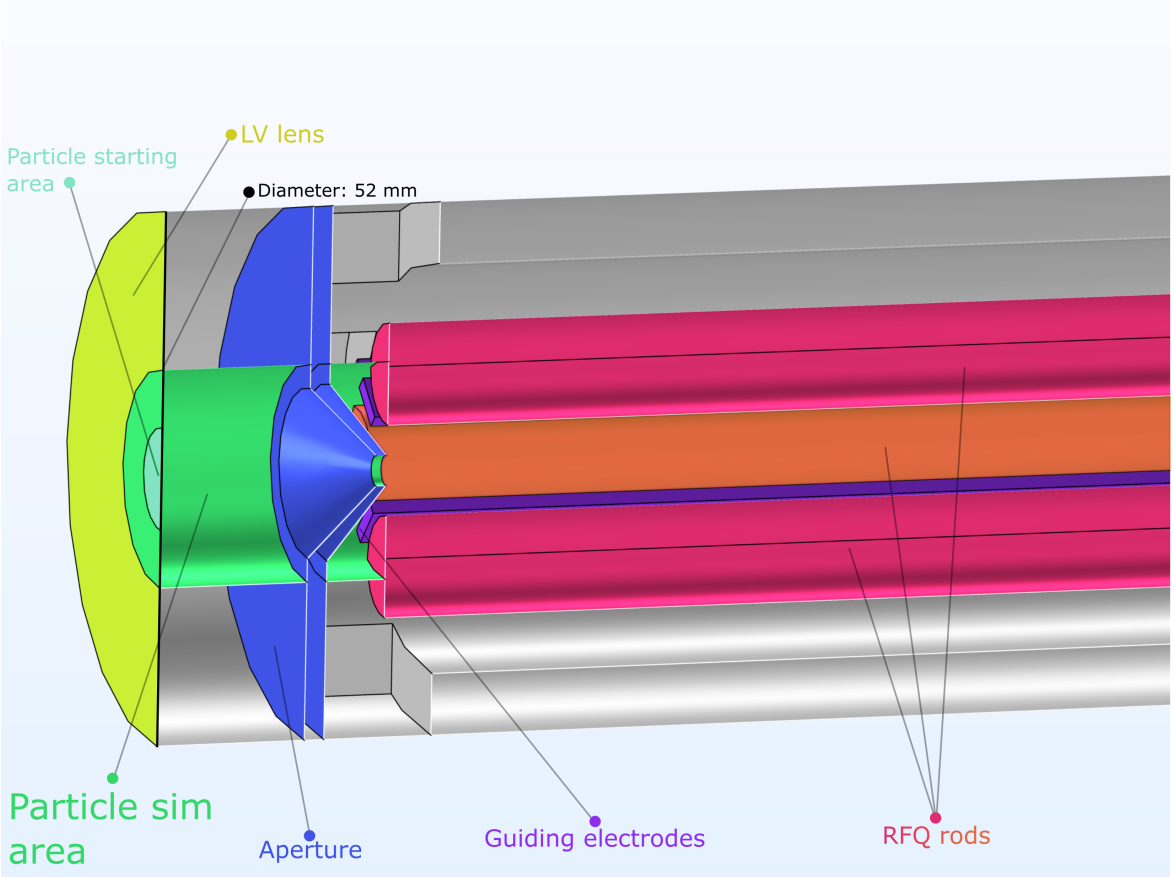

Figure 4.2: 3D Model of the entrance section of ILIAMS with colours and text indicating the components.

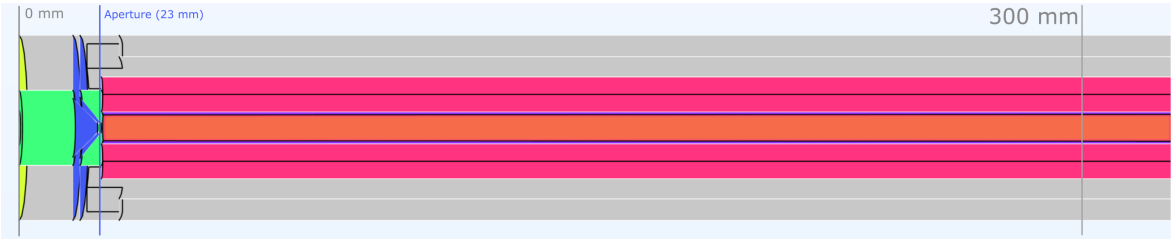

Figure 4.3: 2D lateral cross section of the first 300 mm of the ILIAMS ion cooler with the same colouring as 4.2.

statistics, the simulated time period needs to be around 15 ms. Even on a powerful single workstation, calculating fully time-dependently with the necessary time steps of 20-100 ns would result in simulation times of several weeks and large file sizes of several 100 GB.

For this reason, the only attempted simulation of full ion transmission is via the partially stationary, bidirectionally coupled particle tracing method to ultimately find a convergent solution for a space charge distribution through iteration. Fully time dependent simulations are only performed for the first couple of hundred µs to better understand the general, dynamical effects of an increased beam current and increased space charge in the device without aiming to get data that is directly comparable to experimental data such as transmission or residence time.

Another endeavour was the development of the *arbitrary force model*, which significantly simplifies the problem by use of arguably significant approximations, assumptions and problem redefinitions, but at the same time achieves good agreement with experimental data.

4.3.2 Arbitrary Force Model

Intuition

The effect of increased beam current correlating to reduced residence time is a very important result that is a very likely candidate to be a result of space charge effects and thus, should be explained by the simulations. This *arbitrary force model* was designed, following the results of a simple line of thought about the physical processes:

In the real cooler ions are continuously injected, which means that the particles are slowed down inside the cooler while faster, higher energy particles are streaming in from behind. The injected ion density is directly correlated to the ion beam current, as larger currents mean more particles and charge per unit time and consequently per unit volume when injected with the same velocity. It is then possible to compute an average, equilibrium distance between ions for a given beam current and known beam diameter. The density increases further, while the particles slow down rapidly through collisions in the buffer gas, causing ion packing. Higher number density equals lower mean distances and electric repulsion effects increasing with r^{-2}. All ions are isotropically surrounded by other ions with an over-time mean equilibrium distance - apart from the ones on the surface of the ion cloud, which would feel the force of the ions behind.

Therefore ions on the surface would be affected by the charges behind them while the ions inside would not feel a directed effect, as the repulsive forces cancel each other because of symmetry. While the ions on the surface are repulsed away from the layer below them, more space between the ions is opened, so that ions from the inside have a higher directed tendency to fill this space from being repulsed by the other ions. This process happening continuously would effectively result in a collective behaviour and, in essence, all ions would feel a constant force outwards of the ion cloud predominantly forwards because confinement limits axial increase. Because the ion injection is continuous, the ion cloud has no posterior termination and retrograde forces are overwhelmed by the injection. A larger number of ions correlates with a higher ion density, which directly translates to shorter, mean distances and thus, stronger Coulomb repulsion.

Whenever injection stops or the stream is cut off, ions at the now newly formed end have no longer forces acting on them from behind. This would change the equilibrium of forces and the ions at the rear now experience force from the ions in front of them resulting in retrograde acceleration. The ion cloud now has a beginning and an end. Ions at the posterior are losing velocity more quickly than the rest, while the ion density at the centre, however, is still intact. Ions in the front are therefore not instantaneously affected and are still repulsed and accelerated forwards. The ion cloud in its own inertial frame now spreads in both directions, slowly losing density. After some time, the ion cloud is spread so far that the number density is low enough so that the ion-ion distance is too large for coulomb forces to play a big role. The ions are now mostly only moving through the cooler via the guiding field.

Because of the difficulties related to simulating space charge, no accurate simulation so far has simulated this dynamic fully. The cumulative space charge method is useful for determining a stationary space charge field, which is useful for investigation of beam profile, divergence and other qualities of interest to ion optics. However, the ions never have other ions behind them and only feel the effect of the field extrapolated from the particle paths of the previous simulation, which is not very suitable for processes, where individual and dynamic ion-ion interaction is significant. The ions inside the ion cooler no longer behave like an ion beam, in the sense of ray optics, but, because of the random walk, resemble an ion cloud. A stationary field can not explain that dynamic, microscopic behaviour in detail.

The fully time dependent method would capture this effect, but only when a sufficient number of particles is simulated. This would mean a continuous beam of ions that are injected in sufficiently short intervals for a significant amount of time, so they are at close enough distances to affect each other and feel the effect of continuous injection. With charge scaling, this can be approximated, but a simulation throughout the entire device would take weeks with available resources.

Method

To see whether an accelerating force could explain the shorter residence times, or whether the increased velocity results in too much particle loss through wide scattering from the buffer gas, another separate simulation method has been designed for the full ILIAMS model.

The charged particle tracing module possesses a *custom force* condition with configurable parameters, that is added to the total force $\vec{F}_t$ used when solving the Newton equation 4.9 for each particle constantly throughout the simulation.

At first, real arbitrary forces in forward direction were used in the ranges of 10^{-15} to 10^{-19} Newton to inspect the effect on velocity, residence time and transmission. The accelerative effect is obvious and the residence time inside the device was greatly reduced for larger forces. Forces above 10^{-16} cause a particle loss inside the cooler because of scattering upwards to full beam dissipation.

As a next step, a good approximation of the true accelerating force is needed. For this, the approximate distance between ions needs to be determined first. The ion number density can be taken from measurement or simulation data, or be estimated by dividing the average change of ion number per unit time by the average change of volume these ions occupy per

unit time, using the residence time to calculate an average velocity $\bar{v}$, and simulation data to obtain average beam radius r_{Beam} for a typical gas density as seen in equation 4.21.

$$\frac{I_{Beam} \cdot e^{-1}}{r_{Beam}^2 \cdot \pi \cdot \bar{v}} = \frac{N}{V} \tag{4.21}$$

If one assumes, that each ion is approximately in a cube of certain volume, then the inverse of the number density represents that volume per ion. The edge length of such a cube is then the cubic root of the volume $\sqrt[3]{V} = a$. If it is then assumed, that the ions are sufficiently equidistantly distributed and ordered close to a cubical grid, the average distance can be approximated by the cube edge. Because ions would be maximally packed at an equilibrium distance from continuous injection and are effectively forbidden from occupying the same region because of symmetric repulsion, the grid approximation is assumed to be fair.

If one imagines the surface of the ion cloud grid structure and only accounts for the 9 closest ions ordered behind it, the total forces in any other direction but surface normal cancel out and the total force out of the surface i.e. forwards is given by equation 4.22, where $F_C(r)$ is the Coulomb force.

$$F_{tot} = \sum_{i=1}^{n=9} F_i = F_C(a) + 2\sqrt{2}\left(F_C(a\sqrt{2}) + F_C(a\sqrt{3})\right) \tag{4.22}$$

This force can be directly calculated once using equation 4.21 and 4.22 and is, in a first approximation, assumed to be fixed. The simulation, thus, takes no longer than a usual particle trajectory calculation through the entire cooler, as the additional force is simply a constant added to the total force vector used to solve the Newtonian equation of motion 4.9.

Consequently, this method can correlate beam currents to a hypothetical accelerating force and perform particle trajectory simulations close to the speed of a space charge-free simulation. Residence time can therefore easily be evaluated with sufficient statistical accuracy and compared to real measurement data. To judge the validity of this model, it is possible to perform short simulations using the fully time dependent charge scaling method 4.2.2.

The fully time dependent method gives the most accurate results and is the only one correctly accounting for the full, physical dynamics in real time, yet simulating particle motion through the entire ILIAMS in the *full model* for an expected residence time of up to 15 ms would take several months to finish. However, a simulation of continuous injection and injection stop for a couple of 100 µs, can supply important data on behaviour, acceleration and average velocity for different beam currents to assess the hypothesis of beam current dependent acceleration and the effect of continuous injection in a more realistic setting.

Nonetheless, to do a full transmission evaluation of all possible space charge effects in the environment of a RFQ buffer gas ion cooler with guiding electrodes, a smaller, more rudimentary model was created. In this *simple model*, fully time dependent computation of particle motion with space charge interaction is possible for a full device transmission within a reasonable time frame. Evaluating the general dynamics of the simulation qualitatively can help to comprehend the implications and make better predictions for similar devices like ILIAMS.

4.3.3 Simple Model

The geometry of the *simple model* is similar to the basic RFQ – mass spectrometer model provided by the COMSOL application library. The original model is composed of four, ~12 cm long cylindrical RFQ rods and an accelerating injection lens in a cavity. An injection pipe stretching back up-beam was implemented, to examine the back-scattering caused by the effects of space charge, which is not experienced in a space charge free particle simulation. The meshing follows the same idea as for the *full model*, where a high resolution mesh is used for the computation of the RF field in the frequency domain, and another mesh is used for the particle tracing and space charge simulation studies, where a fine mesh is applied in the particle tracing domain, and a normal mesh is used for the remaining regions as seen in figure 4.4 (B).

Interactions with buffer gas are easily included by adding the *elastic collision* condition to the particle domain and a realistic density can be added by sampling from a smoothed triangular distribution (see A.11). However, when simulating buffer gas, the ions lose inertia through the collisions and effectively get stuck in the gas. This necessitates the implementation of guiding electrodes, which were therefore directly scaled from the *full model* and implemented. Also, the buffer gas density cannot be as large as in the full scale ILIAMS model, because the ions' trajectory diverges too far from the centre due to the scattering causing the beam to become too large and collide with the rods. The model was optimized without space charge computation so that ion transmission was sufficient for a high buffer gas density.

In the last step, the injection and extraction domains were improved and apertures were added similarly to ILIAMS. The injection pipe was shortened and an area between the injection or extraction lens and apertures was inserted, to reflect the geometry of the full model. Statistical tools are added in a similar manner to the *full model* wherever needed. The final geometry can be seen in figure 4.4 (A).

A full simulation, optimized so that almost all ions make it into the extraction area takes up to 800 us of simulated time for the given buffer gas pressure, leading to a computation duration of 21 days for a simulation using the fully time dependent approach of section 4.2.2. Different charge scaling can imitate different beam currents for comparison.

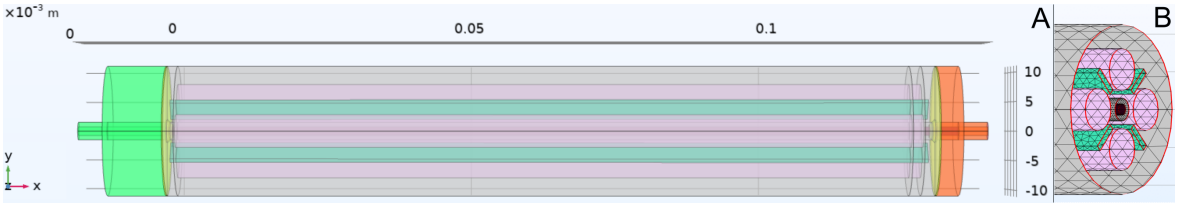

Figure 4.4: The final, full geometry model (A) used for simulation of space charge in a general RFQ buffer gas filled ion cooler ILIAMS analogue consisting of a case structure (gray), RFQ rods (pink), guiding electrodes (turqoise), injection and extraction lens sections (green and orange) and apertures (yellow), next to a cross section (B) showcasing the finer mesh distribution in the particle trajectory area. Axis indicator and axes including scales are included for reference.

5 Simulations with the simple model

For simulations in the simple model, 25 ions are released every 25 ns for the first 10 µs, amounting to a final number of 10025 ions. This simulates a continuous ion beam current of 160 pA for a 1:1 charge scaling.

5.1 Simulations without buffer gas

First simulations were performed with no buffer gas in an early version of the small model – a regular RFQ without apertures, injection/extraction sections or guiding electrodes. For all simulation runs, only the charge scaling factor n was changed while the Mathieu parameters were kept constant. Figure 5.1 gives a cross sectional view of the particle trajectories as lines for different charge scaling factors n=1, 10^3 and a no space charge simulation as reference. The line colour indicates the particle velocity and the increase of ion motion amplitude can be seen. A plot showing the increase in average distance from the beam axis can be found in the appendix (A.5).

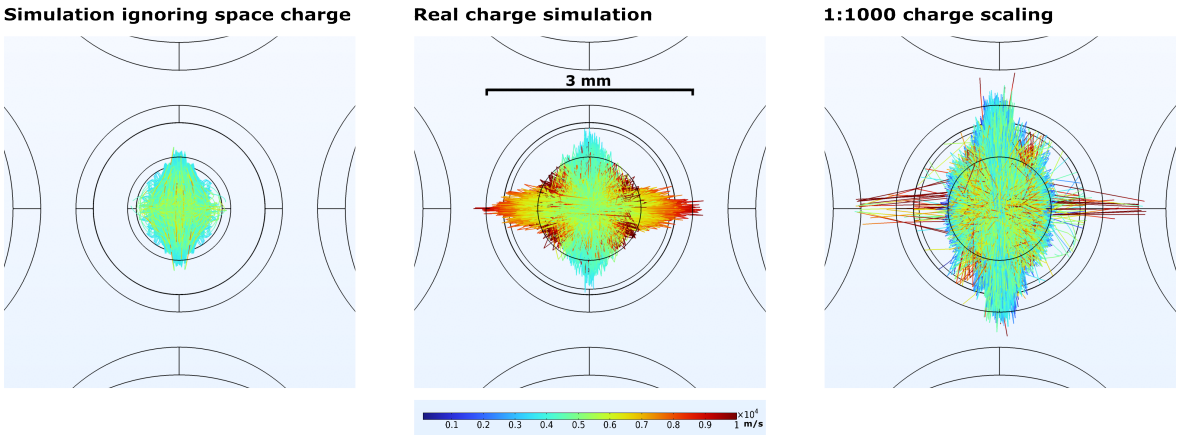

Figure 5.1: Beam normal cross sectional view at the ion trajectories through the entire small model RFQ, traced with lines. The larger motion amplitude related to larger repulsion from the charged beam at the axis can be observed. The colour indicates the velocity magnitude.

5.2 Simulations with buffer gas

The model used for buffer gas simulations includes guiding electrodes. The buffer gas simulation uses a smoothed triangular distribution of number density with a peak at the central point of the RFQ (see A.11). The pressure values mentioned in the following data correspond to the peak pressure at the center of the device. After ion transmission was optimized through the RFQ by varying the q-value and guiding field voltage while space charge was disabled, simulations were set up to investigate the effects of the ion charges on their trajectory using different charge scaling factors.

First space charge simulations were performed with 2 Pa peak buffer gas pressure and 10^2 charge scaling as well as 1 Pa peak pressure and 10^2 and 10^4 charge scaling. Results for the number of particles hitting the exit boundary and the number of active particles over time are presented in figure 5.2. Data on the average distance of ions from the central beam axis is compiled in 5.3.

5.3 Evaluating Simple Model Results

The simple model provides insight into basic principles of the effect of space charge inside a typical RFQ.

5.3.1 Effect of Space Charge without Cooling

Without collisions in buffer gas or space charge effects, the ions move in a periodic, oscillatory motion along the central beam axis. They are confined by the RFQ field and pass through the device quickly in comparison to a cooled beam.

When simulating space charge effects, the motion and trajectories are affected even without cooling. As the ions repel each other, the ion motion amplitude increases, enlarging the beam waist and causing the ions to have a higher risk of colliding with inner structures. As the repulsive effect grows superlinearly with reduced ion-ion distance, highly confined beams are progressively difficult to achieve for larger beam currents.

5.3.2 Effect of Space Charge with Cooling

When adding collisions in a buffer gas, a reduction of ion forwards motion can be observed, firstly due to an increased path length from elastic collisions and secondly from kinetic energy transfer to atoms in the buffer gas. A guiding field is necessary to prevent ions from equalizing their kinetic energy with the buffer gas and essentially performing an undirected random walk.

Under these conditions the effect of space charge is even more pronounced. The beam waist, already widened by the stochastic buffer gas collisions, is widened even further by ion-ion repulsion. Reduced propagation velocity in beam direction means the Coulomb interaction has more time to radially affect the ion momentum outwards and cause beam expansion. This significantly increases the probability of ion loss by collision with inner surface structures. Ion confinement is greatly suppressed and the widened beam potentially decreases photodetachment efficiency, as ions may be outside the boundary of the laser beam. Also, the repulsive forces

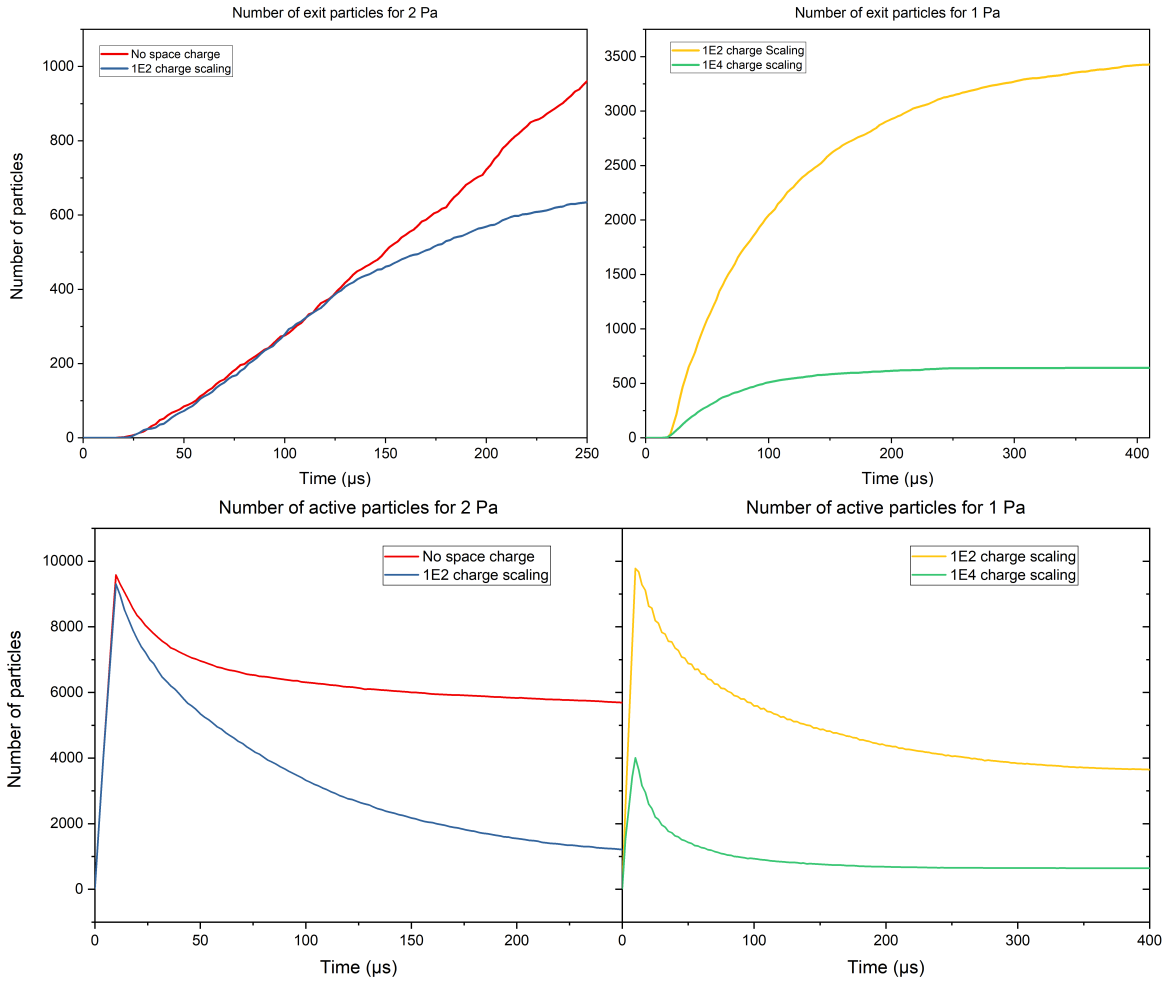

Figure 5.2: Number of particles reaching the exit (upper row) and number of active particles in the device (lower row) over time for a 2 Pa buffer gas peak pressure simulation with no space charge contribution and a 10^2 charge scaling (left column), and a 1 Pa buffer gas peak pressure simulation with 10^2 and 10^4 charge scaling (right column). A clear reduction of ion transmission through, as well as increased particle loss in the device can be identified for larger charge scaling and higher buffer gas pressures.

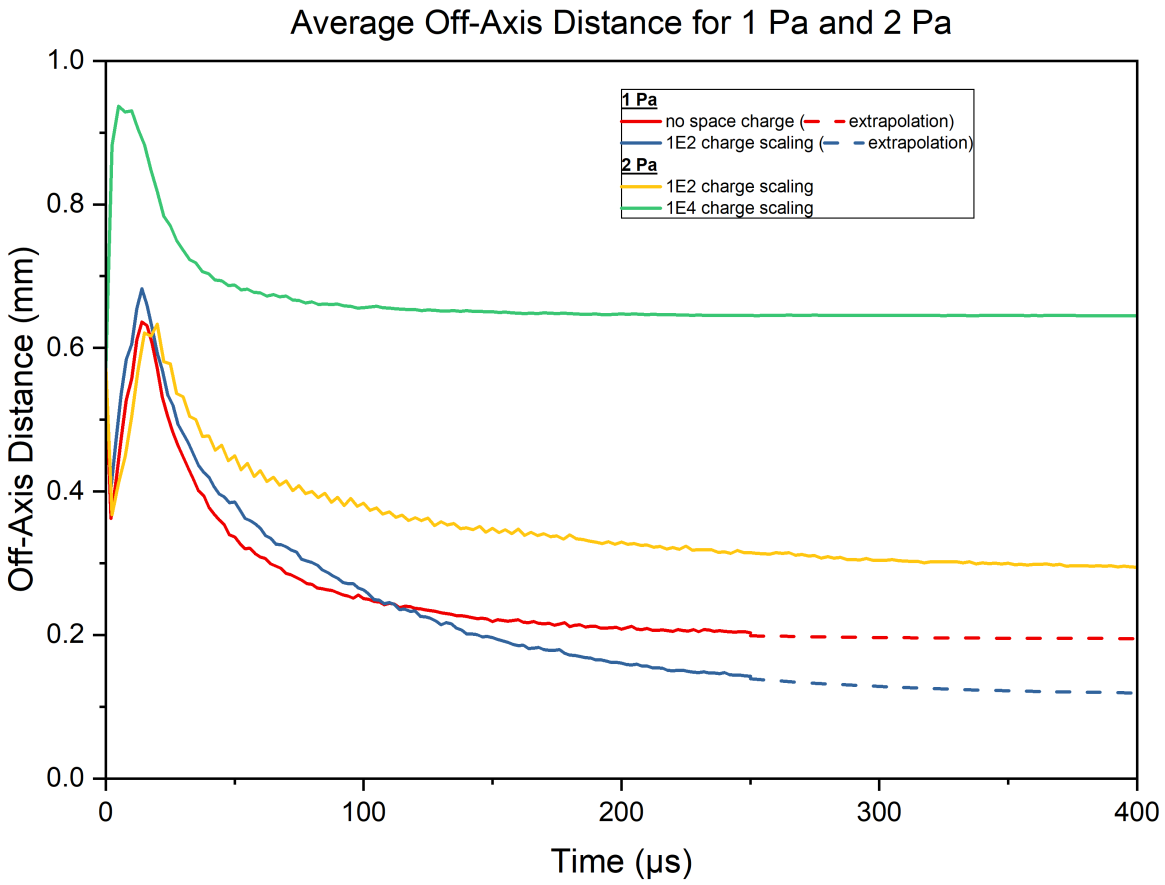

Figure 5.3: Average off-axis distance of the particles over time for a 2 Pa buffer gas peak pressure simulation with no space charge contribution and a 10^2 charge scaling, and a 1 Pa buffer gas peak pressure simulation with 10^2 and 10^4 charge scaling. An increase in average off-axis distance for larger charge scaling, as well as higher buffer gas pressures can be identified. An extrapolation was performed due to shorter simulation times of the 2 Pa simulations and assumed asymptotic behaviour.

reduce the cooling effect of the buffer gas, as the ions are continuously accelerated by Coulomb repulsion.

5.3.3 Conclusions from the Simple Model

Several things can be learned from simulating space charge effects in the simple model. In general, the effect of space charge can be large in an RFQ, even more so when cooled with buffer gas. An increase in average particle off-axis distance, i.e. beam size, is observed, which can quickly result in large ion losses to the inner structures of the device. As there is a verifiable effect in the radial direction and because the coulomb force acts isotropic, it must also be assumed that there are axial effects. Simulations, however, give no clear indication of such an effect or of a correlation between larger beam currents and higher axial propagation velocity. The ion propagation is strongly affected, and different in character for different beam currents, but the ion loss in the small model is too large to have sufficient particle data to be evaluated.

While it might be possible, to further develop and optimize the small model for better transmission and get more valid data from it, the key question of how the ions behave in ILIAMS cannot be answered. Thus, focus has to be put on designing simulations within the full model, which can give indications on how the space charge is distributed, and how the ions propagate for different beam currents, in order to give possible explanations for the current dependent residence time and measurement data.

6 Results of the ILIAMS Simulations

A number of different simulation methods were performed in the full model, approaching the question of how space charge affects the ion dynamics in ILIAMS from different angles. The simulations can be categorized into three different methods: the cumulative charge density approach from bidirectionally coupled particle tracing (see section 4.2.3), the arbitrary force method (see section4.3.2) or the fully time dependent approach with charge scaling (see section4.2.2), but for a limited period of simulated time. Details on used cooler parameters and the applied numeric solver methods can be found in the appendix at A.7.1 and A.7.2.

6.1 Arbitrary Force Tests

6.1.1 Truly arbitrary forces

The range of arbitrary force, such that the simulated ions are still passing through the cooler, is explored in separate studies for a range of orders of magnitude of force. The range is determined to be between 10^{-15} and 10^{-20} Newton of applied constant force where the highest is the limit for near total beam loss, and the lower the limit for notable effect.

The resulting residence time histograms of exit particles at the end of the simulation for different orders of magnitude of applied constant force are depicted in figure 6.1. The respective distance from the central axis averaged over each ion for every time step is portrayed in figure 6.2. The lines end at earlier times because for stronger accelerative forces, the ions reach the exit faster, or are removed from the simulation due to collision with inner wall boundaries. The strong drop for 10^{-15} N, for example, is caused by large particle loss on surfaces, due to large ion beam expansion from buffer gas collisions at high velocity.

6.1.2 Real Force Equivalents

After it was determined that the simulation behaves physically reasonable for a range of added forces and ions can pass through the device, the question comes naturally what magnitude such a force potentially explaining the shortened residence times could have.

Using the model described in section 4.3.2, values for forces acting on the ions in Ion-Laser InterAction Mass Spectrometry (ILIAMS) for beam currents of 32 pA, 3.2 nA, 340 nA and 460 nA were calculated and simulated for. A residence time histogram counting the number of exit particles and their lifetime at the end of the simulation for each of the real force equivalents is pictured in figure 6.3.

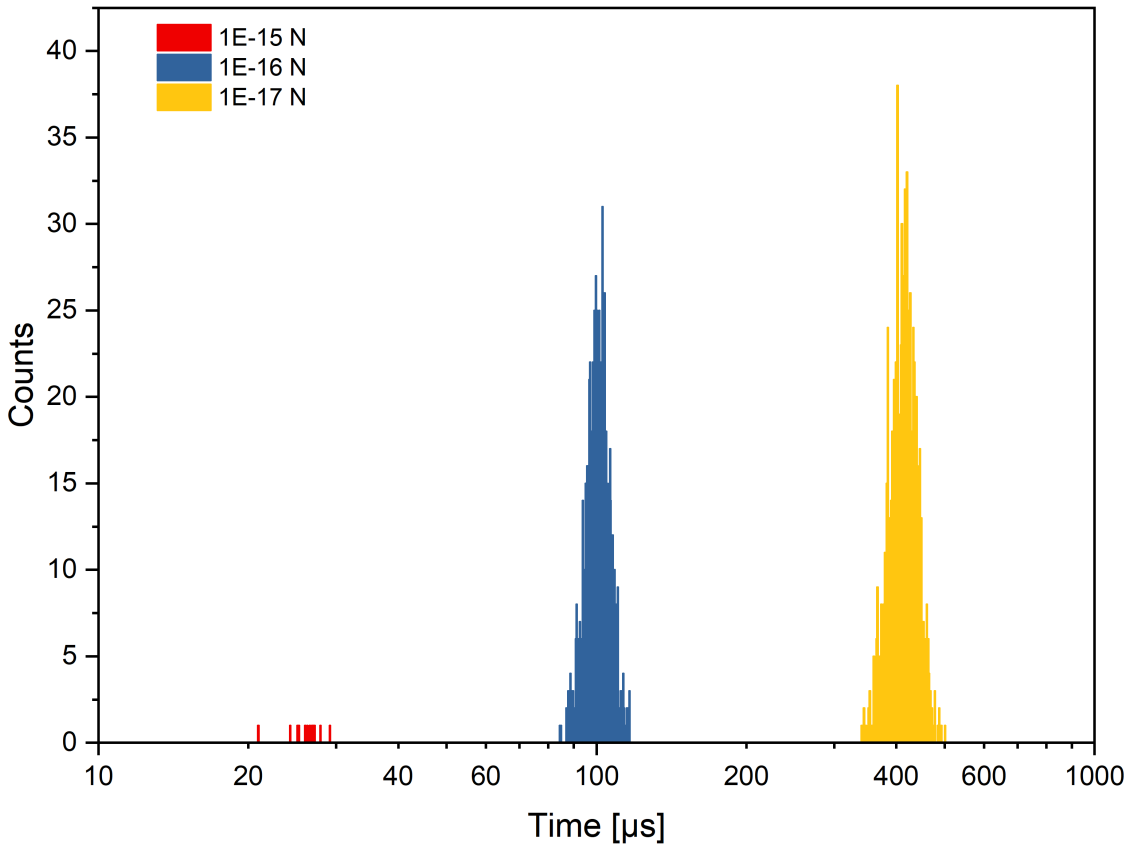

Figure 6.1: Histogram of ion residence times in µs within the device for different magnitudes of truly arbitrary force. For 10^{-15} N (red), only a small fraction of particles reach the exit due to loss in wall collisions. In agreement with the assumption, higher axial forces in forwards direction result in shorter residence times.

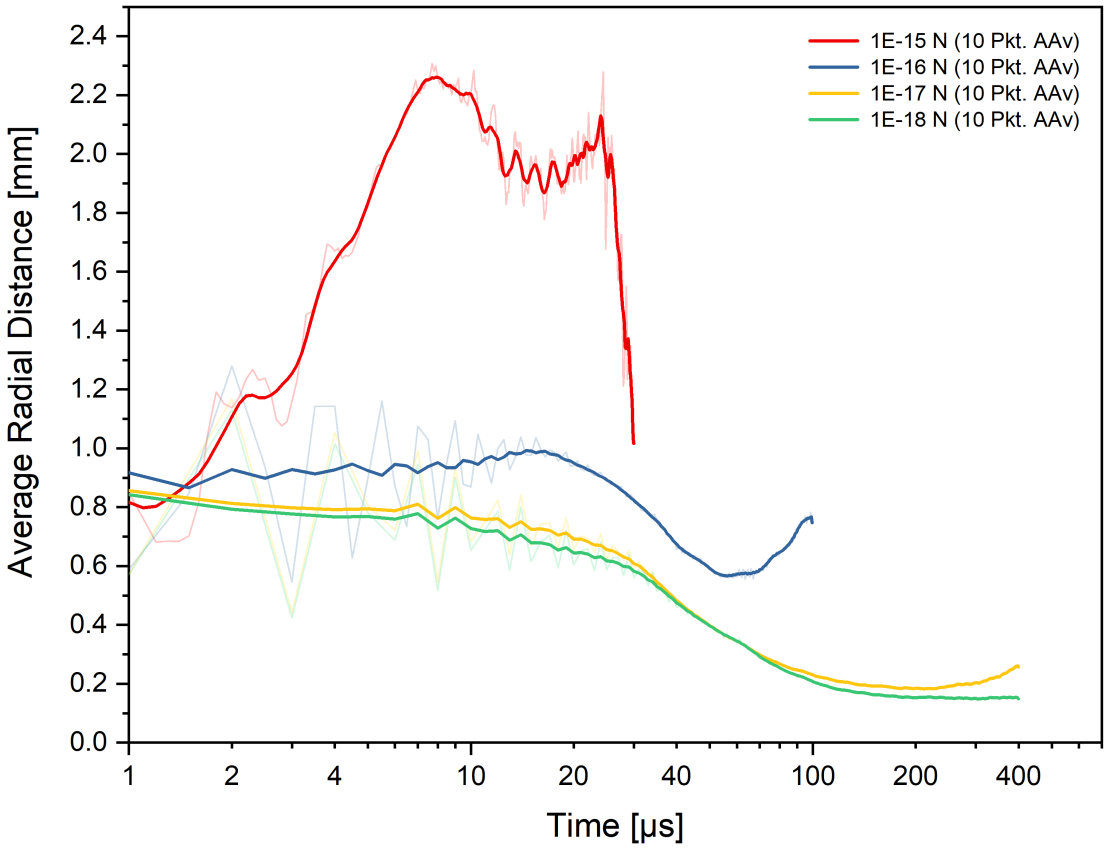

Figure 6.2: Radial distance from central axis in mm averaged over every particle within each time step for various truly arbitrary forces. The values (transparent lines) oscillate strongly at early times and are smoothed by 10 pt adjacent averaging (full color line). For 10^{-15} N (red) and 10^{-16} N (blue), the lines end early because all particles have exited the simulation before 400 µs have passed. Larger axial forces in forwards direction cause the ions to be scattered farther from the central axis.

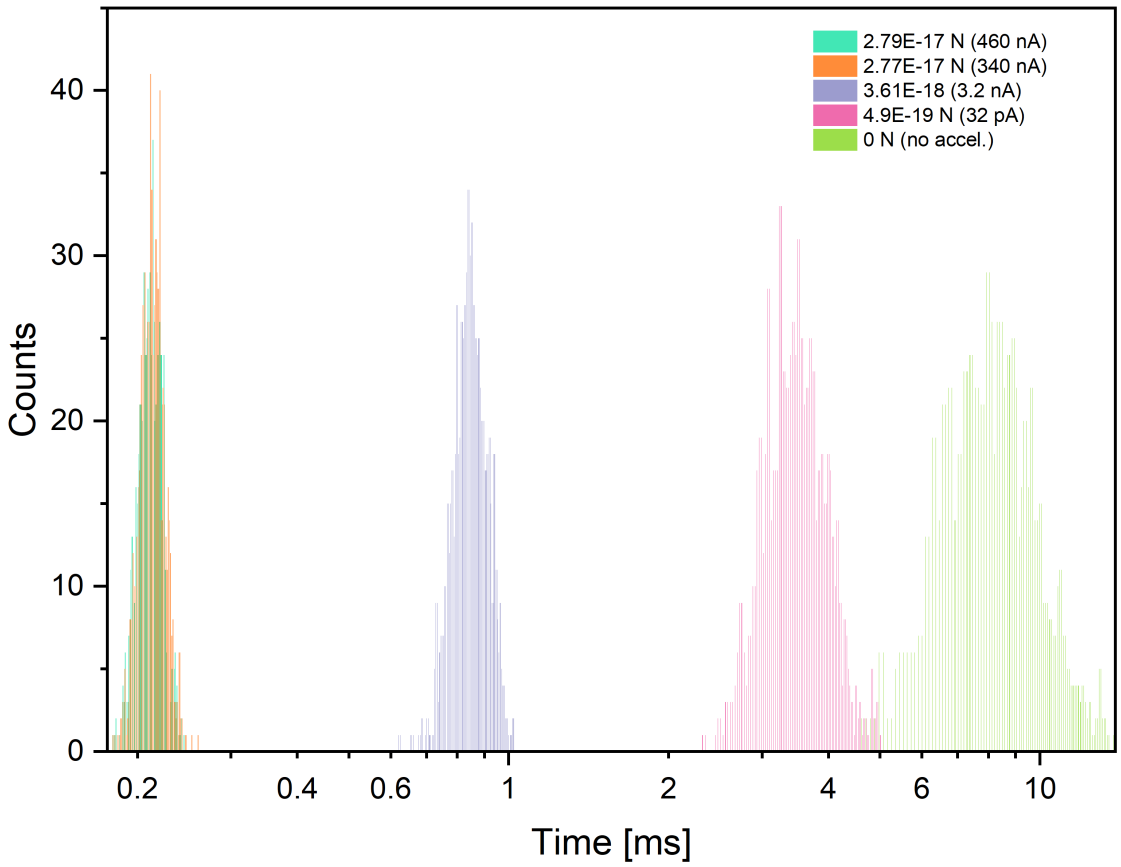

Figure 6.3: Histogram of ion residence times within the device in ms on a logarithmic scale for different forces. The approximated beam current is indicated in the legend. Higher axial forces in forwards direction result in shorter residence times, which agree well with measured residence times for the respective ion beam current.

6.2 Convergence Trials

Using the bidirectionally coupled particle tracing method described in section 4.2.3 with the specify beam current release mode is a simplified and suitable method to obtain a space charge distribution in ion optical compartments. For exploratory purposes, space charge distributions were initially computed only for 300 µs simulation duration for simulated beam currents of 1 nA, 10 nA and 100 nA.

For higher beam currents, it takes an increasing number of iterations and different averaging methods for a converged space charge distribution. For the 10 nA simulations, a setup with a total number of 8 iterations consisting of 4 iterations ramping up and 4 iterations cumulative averaging with arithmetically distributed weights leads to a homogeneous, physically reasonable distribution, which changes insignificantly for higher iteration numbers. The 1 nA simulations were performed with the same settings.

Simulating 100 nA ion beam current with these settings results in a very unphysical, inhomogenous and rough distribution that is different for varying iteration numbers and weights. It must therefore be concluded, that the distribution is not the correctly converged space charge distribution. A simulation of 25 iterations consisting of 10 ramping up iterations and 15 cumulative averaging iterations using geometrically distributed weights with a common ratio of 1.4 results in a smoother space charge distribution.

After achieving convergent solutions for the space charge distributions, it has to be noted that it is still not representative of the real situation. Every iteration is started with the same phase difference with respect to the RF field, which therefore results in trajectories and space charge distributions with a distinct focal point after the aperture. This is remedied by performing 6 individual, full studies with an initial phase difference of $n/6 \cdot 2\pi \quad (n \in [1, 6])$ and, for the 100 nA simulation, a couple of additional values in between. Then, computing the mean field over all resulting fields gives the final space charge distribution for the respective ion beam current.

However, trying the same settings on a 10 nA simulation that is sufficiently long to allow ions to pass through the entire length of the cooler did result in a nonphysical, rough space charge distribution and nonphysical particle behaviour, indicating non-convergence. As this is often a result of stationary space charge overestimation, a higher number of iterations with more gradually increasing accumulation weights can fix this divergence. However, even a high number of iterations with only very gradually increasing, geometric weights did give a divergent, overestimated space charge. As a single, full length run takes almost a whole day to compute, trying to find a convergent space charge distribution through the entire length of the cooler via this method was abandoned, because the required number of iterations would take an unfeasible amount of computation time with available resources.

In any case, several parameters indicative for space charge effects can still be extrapolated from the three 300 µs simulations for 1 nA, 10 nA or 100 nA beam current. A cut line is used to evaluate data along the central axis and the effect of space charge on the electrostatic potential along it is represented in figure 6.4. The field initially rises steeply, due to remnant effects of the deceleration lens before the aperture. Shortly after the aperture at 23 mm, the guiding field takes over and generates the constant gradient observable for the 1 nA simulation. The

electric field is increasingly disturbed by higher currents in magnitudes significantly surpassing the nominal guiding field voltage. Figure 6.5 represents a plot of the radial distance from

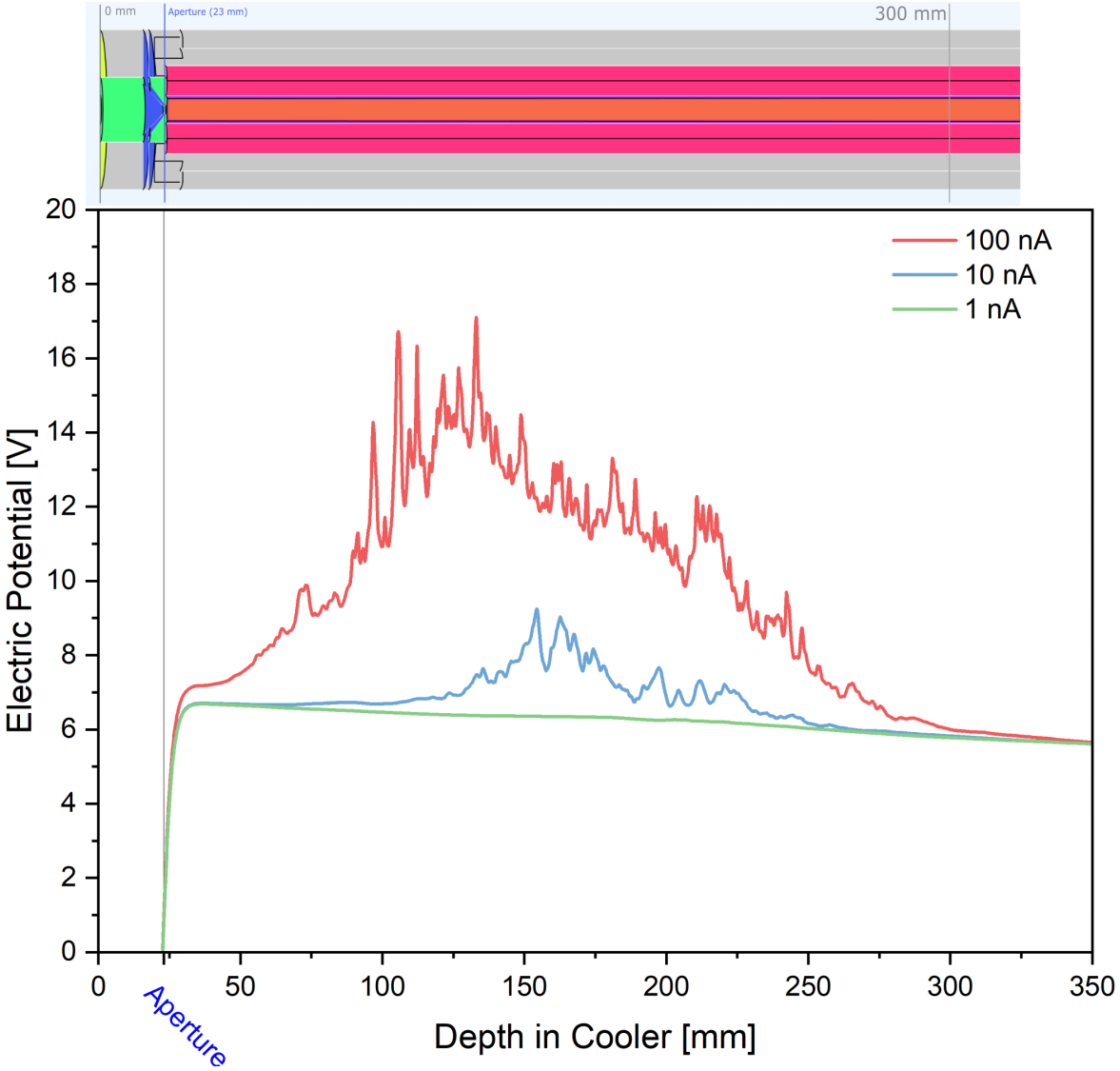

Figure 6.4: Electric potential along the central axis in Volt for a 1 nA, 10 nA and 100 nA anionic beam current. A device cross section is provided for geometric comparison. The constant guiding field gradient begins shortly after the aperture at 23 mm and and can still be identified in a mainly undisturbed form for the 1 nA simulation. For higher beam currents, a potential barrier begins to develop at a certain depth in the cooler. The height of this barrier grows for increasing currents.

the central axis averaged over all ions at every time step. The distance is equal at the start, because ions start with the same configuration, followed by a decrease due to focusing and

passage through the aperture (after 23 mm) and an eventual blow up after the focal point and first collisions with the buffer gas. Then, the deceleration decreases the beam diameter in the confining RFQ field, where the ion motion finds itself in equilibrium between redirection from gas collisions and RF field alterations.

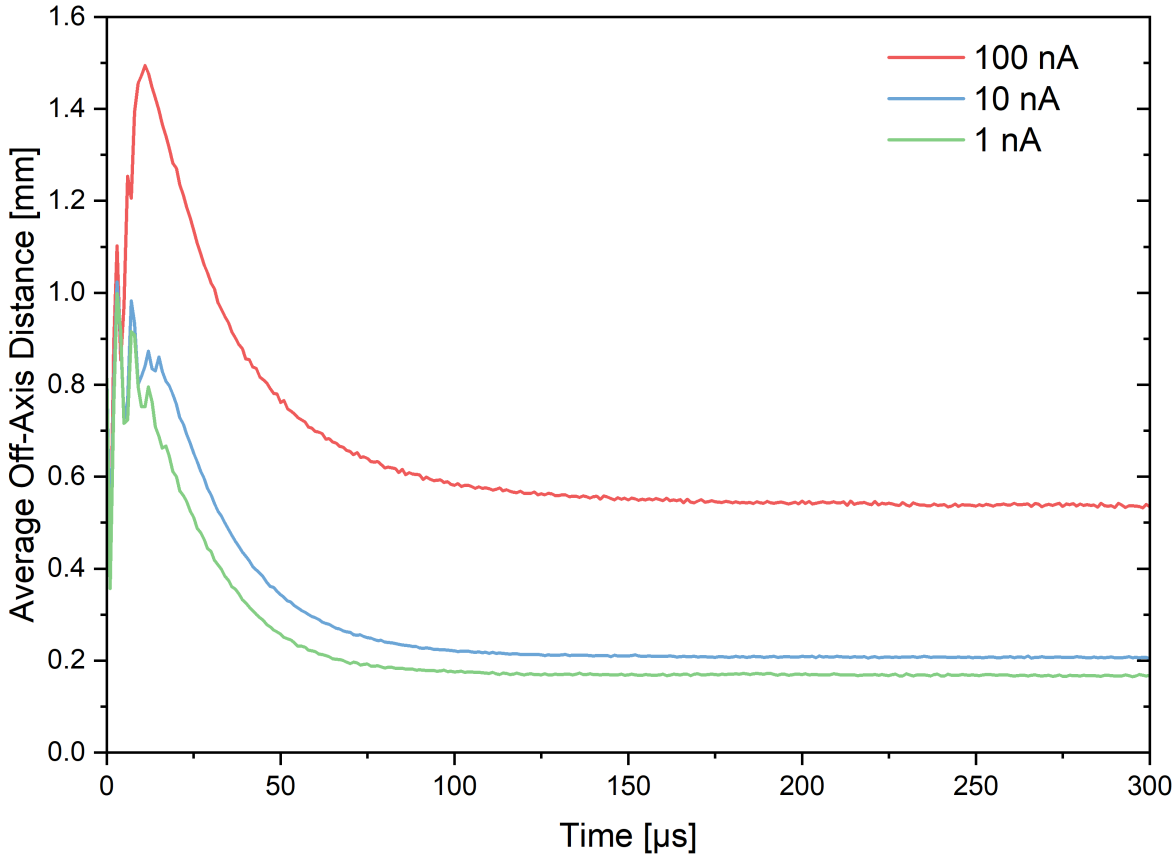

Figure 6.5: Radial distance from the central axis in mm averaged over all ions at every timestep for 1 nA, 10 nA and 100 nA beam current. Higher beam currents lead to larger average beam diameter.

The actual space charge along the central axis is presented in figure 6.6 with a linear, and a logarithmic y-axis for all three beam currents, to show the direct evolution, and the difference in orders of magnitude. The strongly fluctuating space charge values due to the high resolution of the evaluation are smoothed. The density increases gradually with depth, until it reaches a peak at a certain depth, some cm into the buffer gas. In addition to the axial dependency of the space charge density, a lateral cross section along the length of the first half of the cooler, illustrates the space charge density field and it's radial expansion in figure 6.7 with a logarithmic color scale. There, the strong radial dependency of the space charge density can be seen, as it decreases exponentially outwards. The narrow tip of the distribution results

from the fact that the iterative simulation was only performed for the first 300 µs and is not representative of a real distribution. In addition, as seen in the cross section normal to beam direction in figure 6.8, the field is predominantly radial symmetric at the high density center, but becomes increasingly rectangular in shape, for the more sparse, outer regions. This is due to ions moving in the electric field of cuboid guiding electrodes.

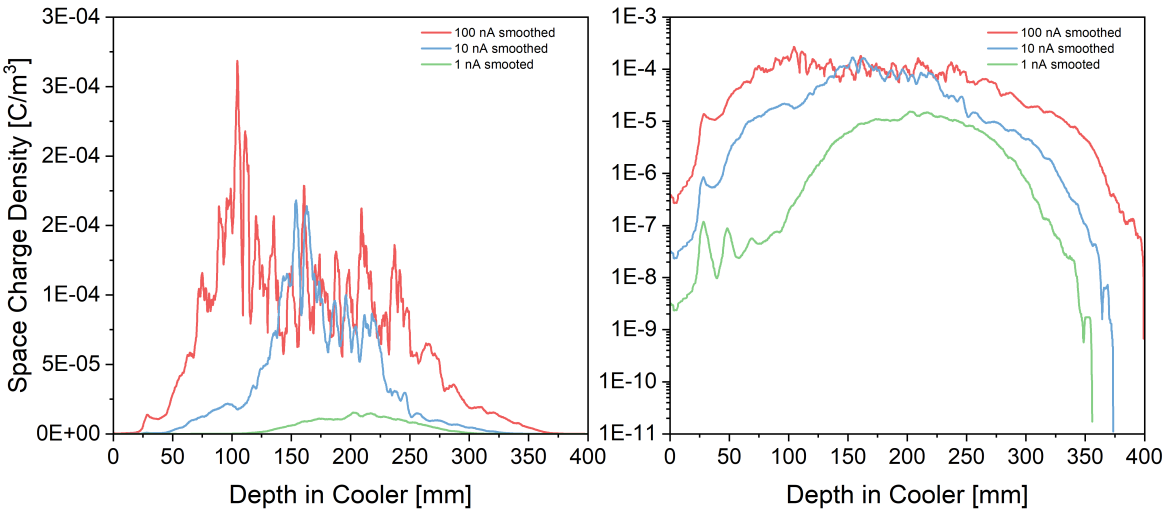

Figure 6.6: Space charge density in C/m^3 along the central axis for a 1 nA, 10 nA and 100 nA beam current on a linear scale (left) and a logarithmic scale (right) 300 µs after injection. On a linear scale, the difference of space charge density seems to be significant, but on a logarithmic scale the distribution follows a similar trend for different beam currents, where it reaches a peak maximum with varying magnitude at several cm into the device. The height seems seems to be at a limit at around 10^{-4} C/m^3.

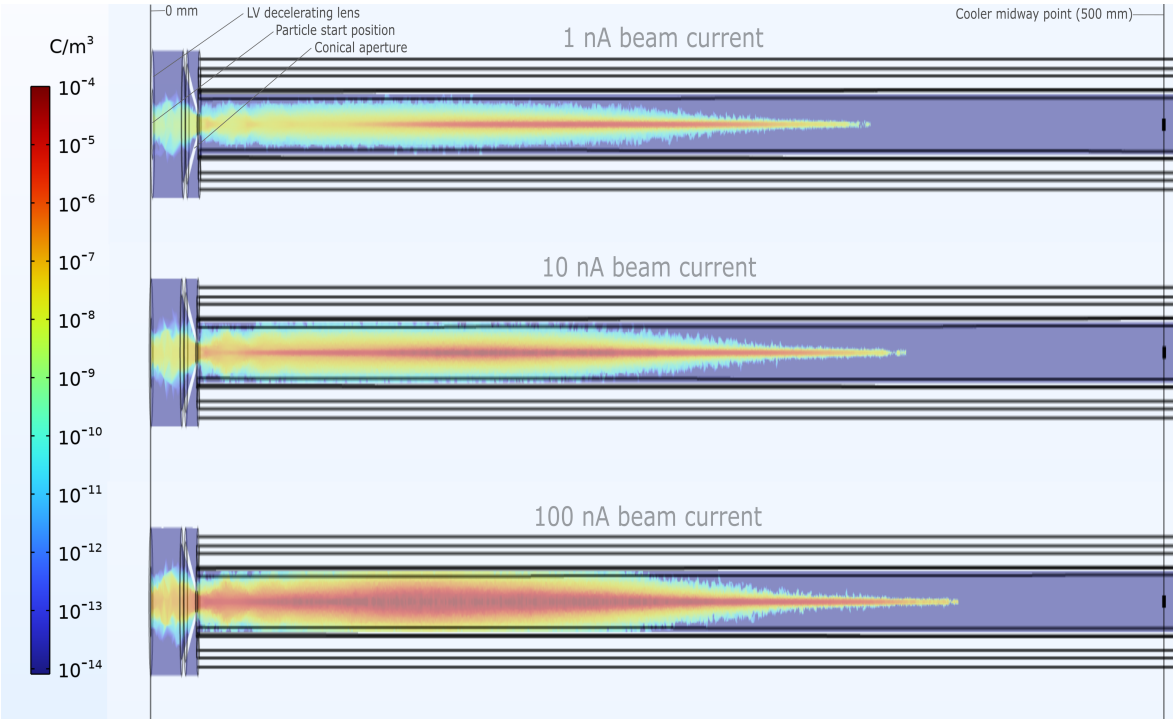

Figure 6.7: Space charge field in C/m^3 on a logarithmic scale for 1 nA, 10 nA and 100 nA beam current 300 µs after injection. While the space charge density distribution is comparable for larger beam currents, the magnitude grows significantly. Higher currents result in widespread distribution and near-filling of the cooler with high charge densities, which for low currents are only present close to the central axis.

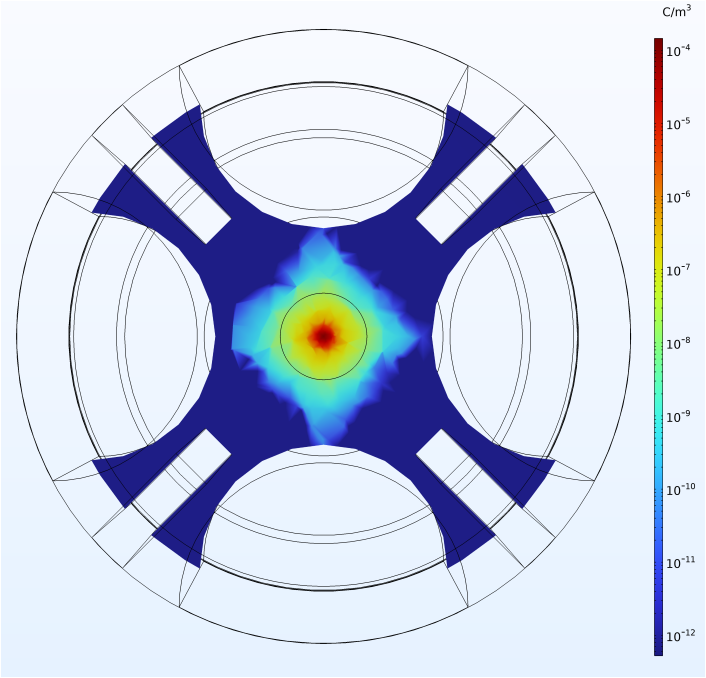

Figure 6.8: Beam normal cross-sectional view of the space charge distribution within ILIAMS in C/m^3. While the high density center is predominantly radial symmetric, the outer charge field adopts an increasingly rectangular shape due to the guiding electrode geometry.

6.3 Fully Time Dependent Injected Pulse

Without the resources to simulate the entire particle flight fully-time dependently, it will not be possible to compare simulation results to data obtained by physical measurements. However, simulating a short, pulse-like injection of ions into the cooler for a sufficiently long simulation period gives insight into the behaviour of ions within ILIAMS and may help to understand the experimental results. Special focus is put on the ion velocity and propagation through the device for different charge scaling, i.e., beam currents, to make extrapolations and explain the shortened residence times.

To that avail, a simulation was set up that injects 40 ions every 2 µs for 500 µs. Injecting a smaller number at closer intervals was avoided, as the charge scaling approximation can only deliver reliable results if enough Newtonian bodies partake in the interaction to represent ensemble behaviour. For example, injecting only 2 ions every 0.1 µs results in a sequential simulation of a Newtonian 4-body process, which does not converge to an ensemble result over time. In reality, however, injection happens continuously, with all ions already in equilibrium distance from each other. Initializing 40 ions out-of-equilibrium, at the same axial position at the start of the simulation, results in large radial repulsion and unsuccessful injection through the aperture, especially with scaled charge. To solve this conundrum, a simulation was performed without space charge until the ions passed into the RF field, where their position and velocity data was saved to serve as initial condition for all space charge simulations. This enables simulation of space charge effects of the cooled ions, which are expected to be the dominant contributor, as well as direct observation of the cooler filling process and early developments towards a steady state equilibrium in ILIAMS. Possible effects during injection itself are likely not accurately resolved.

Initially, simulations were then performed for a charge scaling factor of 10, 10^3 and 10^4 on a base ion current of I_0=3.2 pA based on the injection frequency described above of 40/2µs. The approximated beam current in the simulations thus is $I_0 \cdot n = 32\ pA, 3.2\ nA$ and 32 nA. Preliminary data showed large charge overestimation for scaling factors above 32 nA and the results diverged more and more from experimental data. The overestimation error described in section 4.2.2 became dominant and all simulations above 32 nA had to be disregarded. They are, however, potential representative simulations for very large beam currents, where ILIAMS reaches a charge limit. The data is shown in a dedicated section in the appendix A.4.

To make an accurate simulation of higher beam currents possible, "high rate" simulations with a 10 times larger injection rate (I_0=32 pA) are performed, enabling the simulation of 320 nA, 160 nA and again 32 nA for comparison. Due to the larger particle numbers and corresponding larger computational resource costs, it was not feasible to inject at such a high rate for the same duration as the "low rate" simulations, so the simulation was configured to inject for 200 µs and then continue for another 200 µs. Because of this, the two simulation variants cannot easily be compared. The upcoming figures show the data of both, the "high rate" and "low rate" simulations.

6.3.1 Particle Positions

The effect of different charge scaling can most prominently be seen in figure 6.9, depicting the particle positions for different beam currents after the same injection period right before injection ends at simulation time t=500 µs (low rate) and t=200 µs (high rate) respectively. Within the two injection frequency modes, higher currents result in ions reaching higher depths over the same time period, as well as higher velocities. For the high rate simulations, a clear back-flow of ions towards the entrance aperture can be observed. The difference between the low and high rate 32 nA simulation gives an idea about the extent of overestimation.

6.3.2 Electric Field

Figure 6.10 shows the electric field along the central axis for various beam currents evaluated during injection at t=500 µs for the low rate and t=200 µs for the high rate simulations. The position of the peak is dependent on the position and distribution of the ion cloud and therefore is different at every time step.

The near space charge free field from the tilted guiding electrodes is mostly undisturbed and can easily be identified in the 32 pA simulation through the constant gradient. For higher beam currents, space charge effects begin to appear. A spike right after injection occurs due to focusing through the aperture. Charges accumulate near the mean deposition depth in the buffer gas and an electric potential well develops, the dimension of which is dependent on the number of charges in the system. As the potential is in the same order of magnitude as the guiding field, space charge effects can be expected to cause a dominant disturbance of particle propagation and transmission.

6.3.3 Beam Characteristics

To gauge the transportation mechanic in two inertial frames, the evaluation of the various parameters is performed over both the simulated time and particle lifetime. Evaluating over simulated time presents data from the viewpoint of the experimenter observing the experiment. The averages are taken over all particles regardless of their lifetime and position in the cooler. Evaluating over average particle lifetime presents data from the viewpoint of the particles. It represents the average experience a particle has while travelling through the cooler. This view gives more insight into the processes involving the particles and therefore a unique view compared to real measurements.

Beam Radius

The radial off-axis distance of the particles, depicted in figure 6.11, corresponds to the ion cloud radius. For all currents, a small peak manifests right after injection, stemming from de-focusing, deceleration and repulsion, after which the off-axis distance decreases. For low beam currents, this occurs quickly after injection and the ions equilibriate close to the central axis. Higher beam currents show a trend towards larger radii. All particles in the simulation are represented in the scatter plot in figure 6.12. The width of the distribution and range of possible states also grows with injected current, corresponding to an increase in average

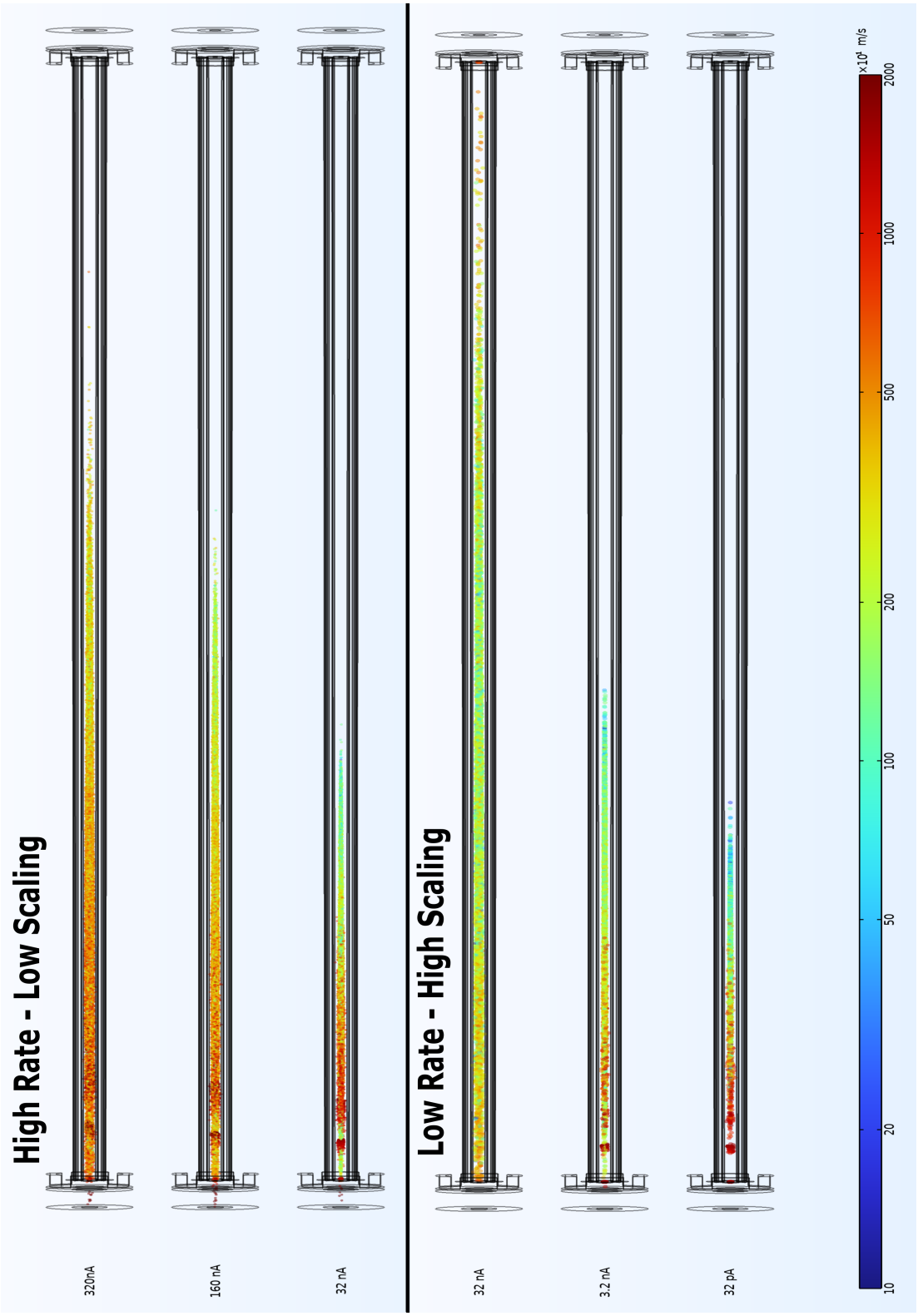

Figure 6.9: Vertical presentation of the particle positions in ILIAMS for high injection rate, low charge scaling simulations of 32, 160 and 320 nA after 200 µs of simulated time (upper), and for low injection rate, high charge scaling of 32 pA, 3.2 nA and 32 nA after 500 µs of simulated time (lower). The times were chosen right before the injection ends. The color indicates the particle velocity magnitude in m/s on a logarithmic scale shown alongside. Higher beam currents lead to higher ion velocity and faster propagation through the cooler. Ions reach larger depths over the same time period.

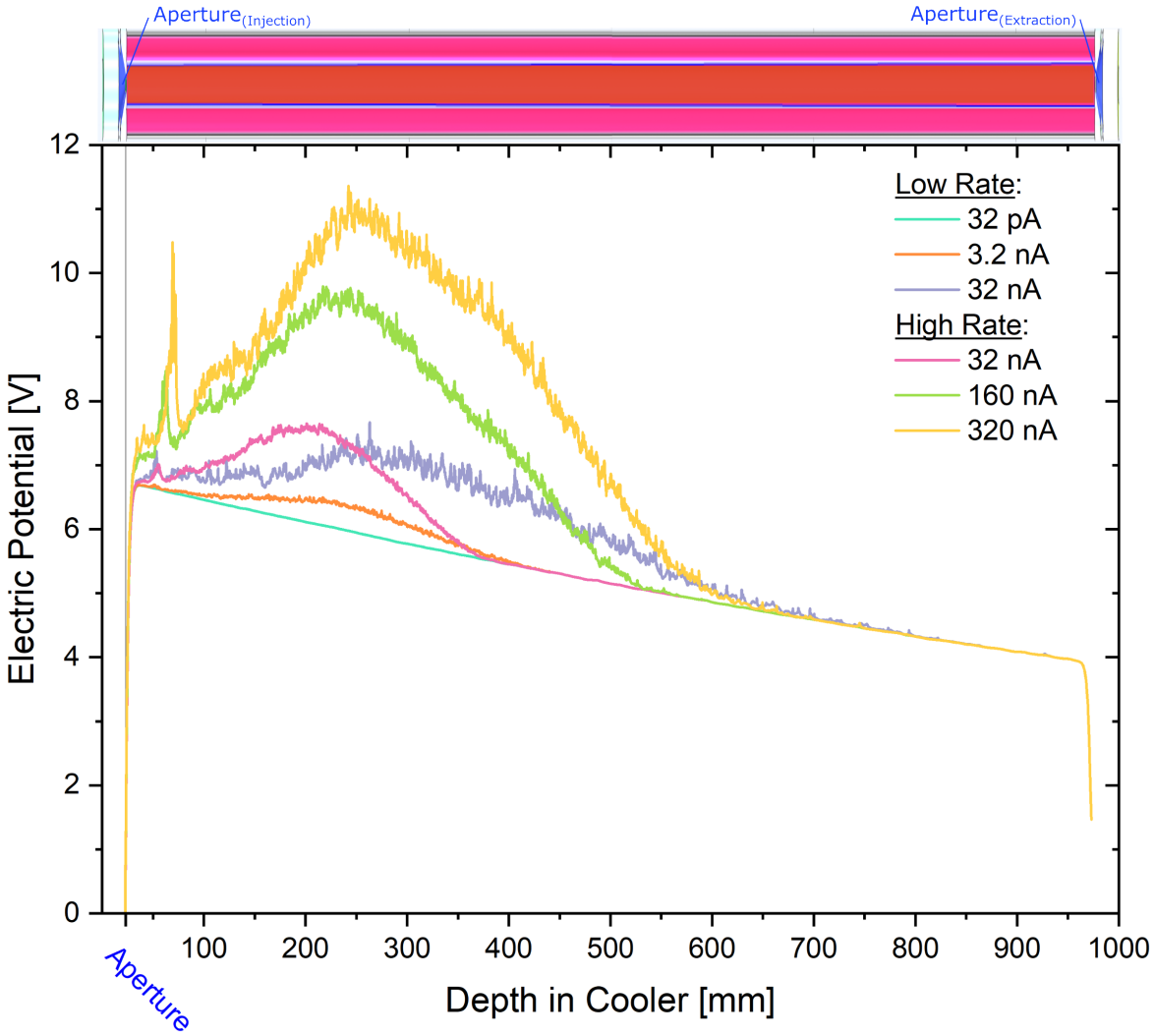

Figure 6.10: Electric field in the cooler segment evaluated along the central axis for a negative test charge and disregarding the RF field for the 3 high rate (@ t=200µs) and 3 low rate (@ t=500µs) simulations of different beam currents. Higher beam currents cause increasing disturbance of the constant guiding field gradient and a larger potential barrier.

particle distance. For high currents, several ions reach radial distances outside the spot size of the laser and some even approach the inscribed radius of the rods at 4.37 mm.

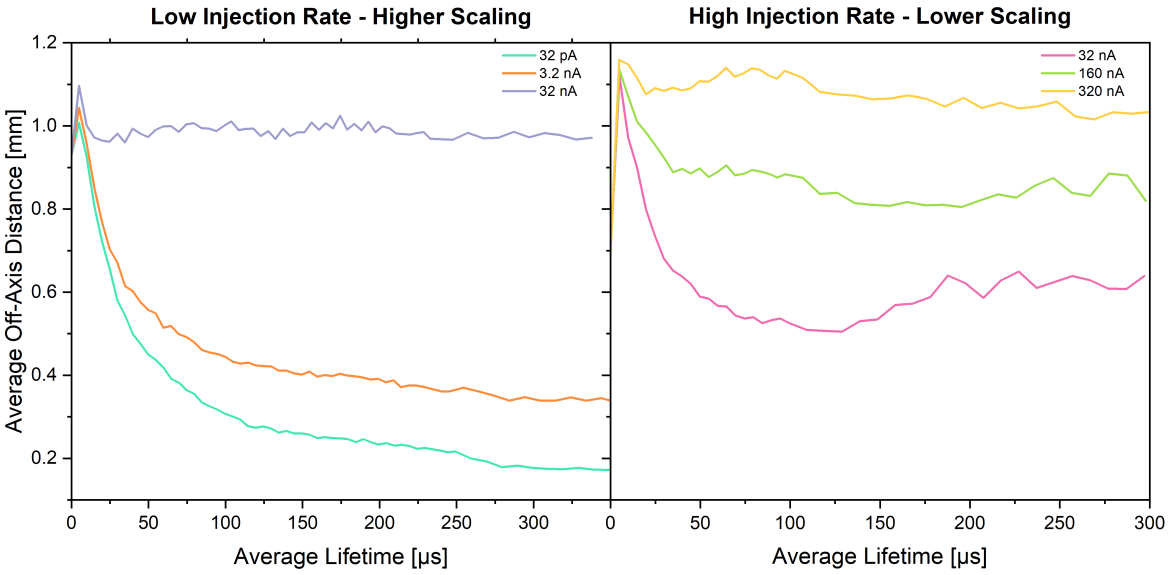

Figure 6.11: Radial distance from the central axis in mm averaged over all particles within each time step over the average lifetime for low and high rate simulations. Larger beam currents lead to an increase in ion cloud radius and reduced confinement.

Particle Depth and Propagation in Cooler

The actual ion transport process can be evaluated by observing the average depth of the particles over simulated time, as shown in figure 6.13. The plots correspond to what is expected from theory: ions are injected at large velocities and lose energy through buffer gas collisions. Once they have lost all their initial forward momentum, and collisions mainly redirect their movement uniformly in all directions, they have reached their deposition depth. Due to the statistical nature of collisions, all ions reach this depth around an average position. All motion bias forwards, or backwards from that point on is due to the set guiding field gradient, and space charge effects. Higher beam currents are deposited deeper on average, and deceleration seems to be adversely affected, as ions reach larger depths more quickly. After reaching deposition depth, average forwards propagation occurs at a constant rate at a terminal drift velocity, as indicated by the constant gradient in all cases. After the injection stops, the average depth position jumps forwards. This is due to a larger particle loss rate in lower cooler depth regions, which is no longer compensated by the number of injected ions. This jump effect is stronger for higher currents, correlating with a higher impact and thus extent of space charge. The positions can also be evaluated from the viewpoint of the particles over their lifetime. 2D histograms enable the evaluation of the distribution and spread of possible position states. Figure 6.14 shows such a histogram for the three low rate, and high rate

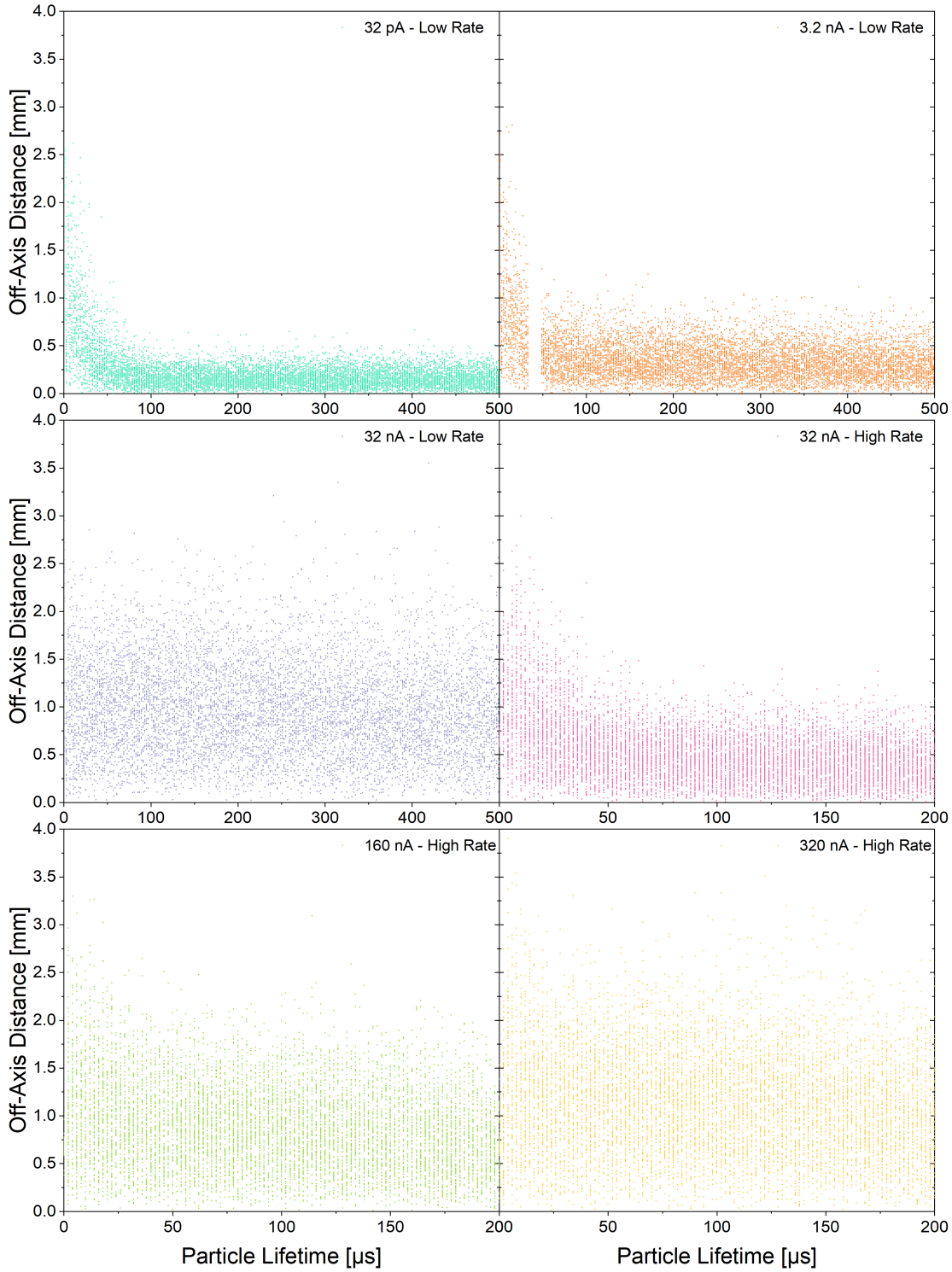

Figure 6.12: Particle scatter diagram showing the off-axis distance and corresponding lifetime of every particle in the simulation during injection. For the high rate simulation, only 25% of particles are shown for viewability. Higher beam currents lead to larger off-axis distances.

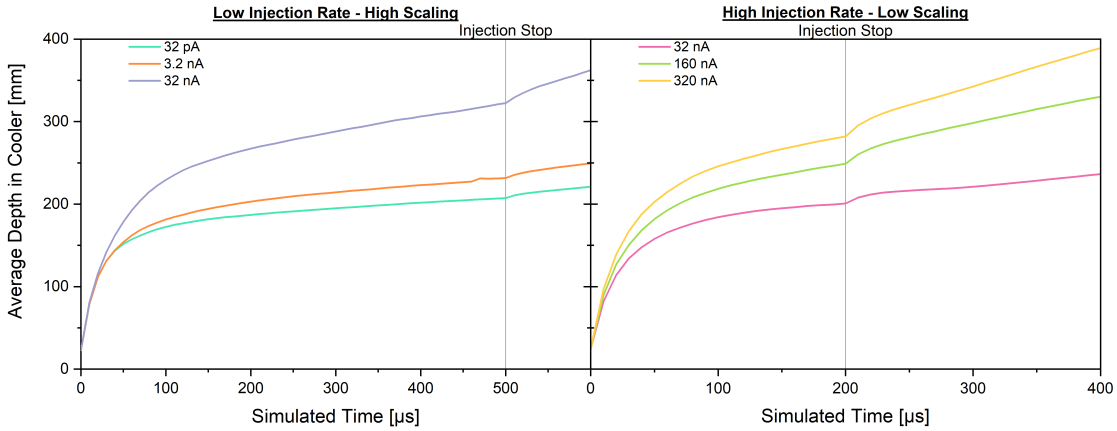

Figure 6.13: Average particle depth, or position within ILIAMS, in mm over simulated time in µs for all low rate simulations (left) and high rate simulations (right). Different injection duration for the high and low rate simulations are indicated by their respective times of injection end. Larger beam currents lead to quicker progression into the cooler and larger average velocity, indicated by the slope of the curve. The jump after injection end is due to an increased loss at lower depths that is no longer compensated for since injection ceased.

simulations. The color legend indicates the abundance relative to the peak. The position a particle can be in within the cooler after a certain lifetime varies to an increasing degree for higher beam currents. While the low current simulation has a narrow spread of possible states, this changes for higher currents. Ions can live long and make it far into the cooler, but can also turn around towards the entrance and populate depths even lower than the mean depth they were initially deposited in. In the high current simulation, an additional effect becomes visible: The state distribution splits and ions seem to avoid a certain depth, which seems to correlate with the mean deposition depth. A large fraction of the ion stream passes this depth and continues onwards, while a smaller portion propagates backwards towards the entrance. This is suspected to be indicative of a barrier effect. Ions that lose a large amount of energy in early depths through a larger number of collisions do not have sufficient inertia to make it past this barrier and stay behind at lower depths. The barrier is likely the main bulk of ions at the mean deposition depth before them, which creates the large electric potential seen in figure 6.10.

In addition to the position coordinate, the length of the particle trajectory is also a valuable parameter to evaluate. It gives insight into the total distance moved by the particle, regardless of the direction, and thus gives valuable data about the degree of redirection in the dynamic. Figure 6.15 shows a 2D histogram of particle trajectory length over depth in the cooler. The color legend indicates the abundance relative to the peak. For low currents, the distributional spread is very narrow, and particles follow a very predictable pathway. The absolute distance moved by each ion correlates strongly with the depth in the cooler. The lower right diagonal half of the distribution is empty because the diagonal line represents the direct path, i.e.

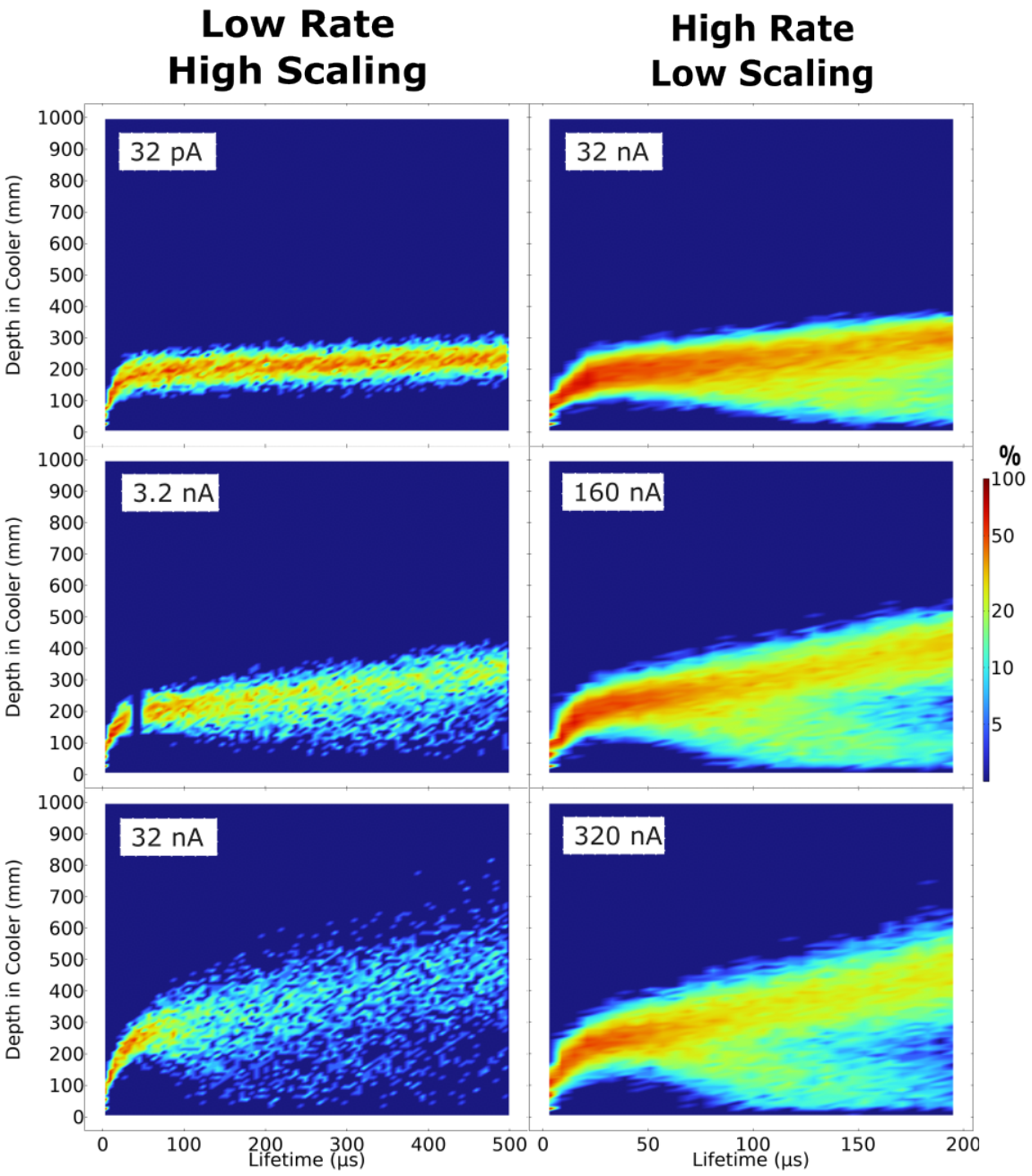

Figure 6.14: 2D particle histogram (bins: 6 µs/10 mm) showing the depth in the cooler in mm over particle lifetime in µs during injection (low rate@500 µs, high rate@200 µs). The color indicates the relative abundance compared to the peak on a logarithmic scale. For larger beam currents, the width of the distribution band increases over lifetime. For very large currents, the distribution splits and only a portion of the ions propagate further into the cooler, while some ions move back towards the entrance aperture.

particles propagating forwards without being redirected. It seems throughout all currents, this is the predominant pathway for lower depths, meaning most ions move without being redirected until they reach higher depths corresponding to higher buffer gas densities. At these depths, the trend shifts and more and more redirection occurs. For increasing currents, the spread increases and particles can move large distances without reaching higher depths. The range of possible states increases for higher currents. Also, similar to figure 6.14, a split in the distribution of possible states can be discerned. The main bulk of the particles propagates forwards, while a band veers off backwards to lower depths at high trajectory lengths. Some ions move a distance corresponding to 2 cooler lengths but are still stuck at depths of several tens of mm, even before their main deposition depth. This correlates well with the hypothesis that the ions at mean deposition depth generate a large electric potential barrier that some ions cannot pass.

Velocity and Phase Space

In addition to the position, the average propagation velocity, meaning the change of the depth coordinate over time $\dot{z}$, can also be directly evaluated. Figure 6.16 depicts the velocities for all simulations. The ions decelerate strongly at the beginning and over time reach an average propagation velocity asymptotically. All simulations show a similar trend up until the injection for the high rate simulations ends. Higher beam currents correspond to larger velocities and the velocity drops rapidly and quickly reaches another asymptotic value after injection stop. The average propagation for the high rate simulations even drops below zero, caused by significant and violent backwards motion of several ions at early depths.

To take averaging misconceptions out of the equation, the entire phase space of propagation velocity over depth can be observed for different times in the simulation in figure 6.17. The first 50, 100 and 200 µs after simulation start show the situation during injection, where a particle cloud develops. During injection, a clear flow of high velocity ions can be seen entering the phase space at 2 µs intervals, collecting around a mean deposition depth. As the flow continues, the phase space expands in both directions, to mainly positive propagation velocity after the mean deposition depth, and mainly negative propagation velocity before. The ions are either driven forwards or backwards by the charge accumulation. At 200 µs a stream of ions being pushed back through the entrance aperture can be seen. After the injection ends, the last ions reach the mean deposition depth and the phase space disturbance ends at around 240 µs, resulting in a more linearized distribution. As the ions distribute throughout the cooler, at t=250 µs a trend towards higher velocities at higher depths begins to develop. A near linear correlation between cooler depth and particle propagation velocity can be observed 200 µs after injection stop at t=400 µs.

Kinetic Energy and Phase Space

To better understand the fundamental reason behind the higher velocities for larger beam currents, the kinetic energies of the particles are evaluated before injection ends (high@200 µs, low@500 µs) in figure 6.18. This gives an overview of all the different, possible energy states the particles can be in over their lifetime. The energy spread for all ion currents is approximately 2

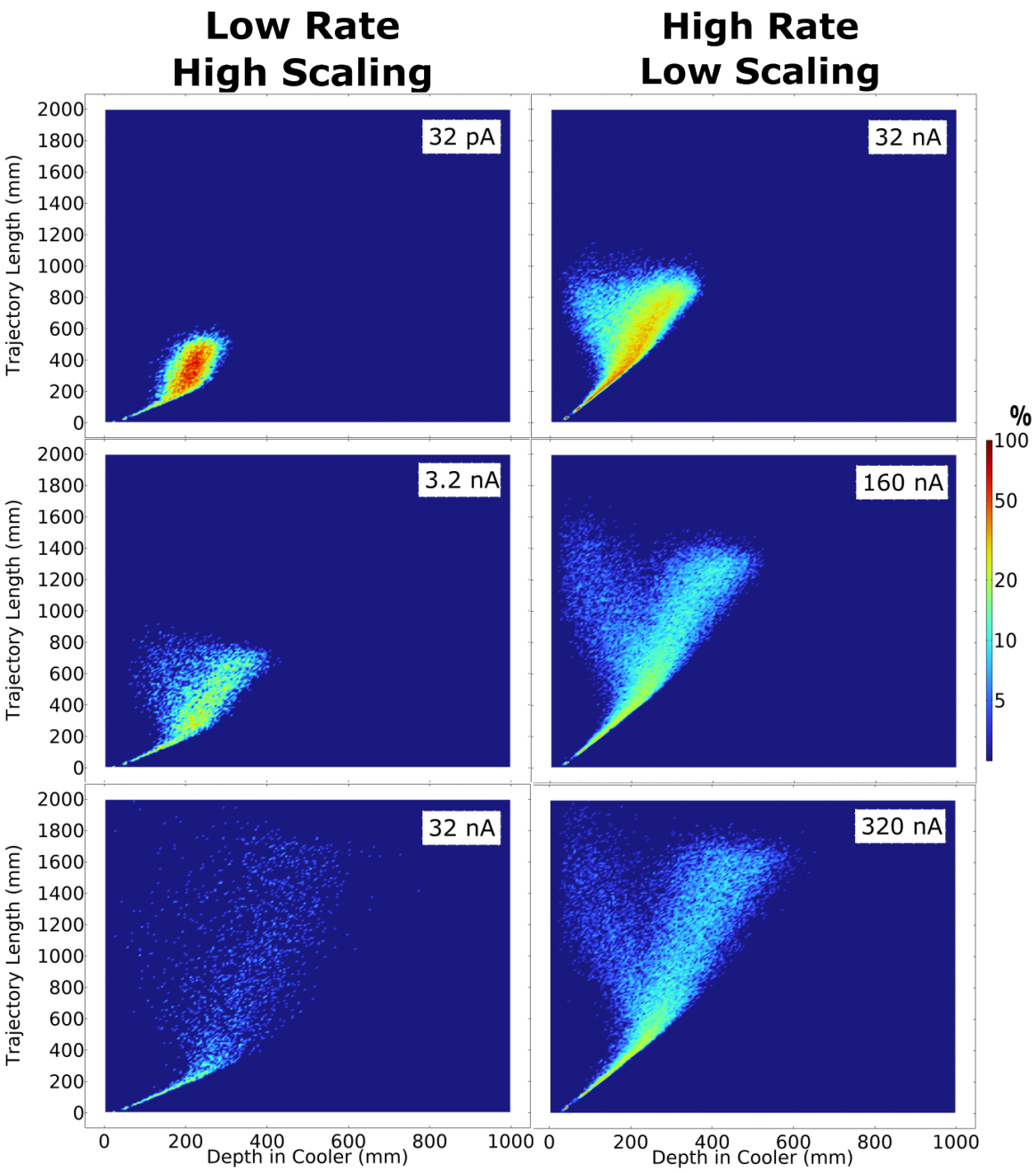

Figure 6.15: 2D particle histogram showing the trajectory length of each individual particle in mm over the depth in the cooler in mm during injection (low rate@500 µs, high rate@200 µs). The color indicates the relative abundance compared to the peak. In low depths, the majority of ions follow a direct path - buffer gas redirections only take over at a certain depth. For higher beam currents, the distribution of possible states widens over lifetime. For the 160 nA simulation and beyond, the distribution splits and several ions propagate back towards the entrance aperture.

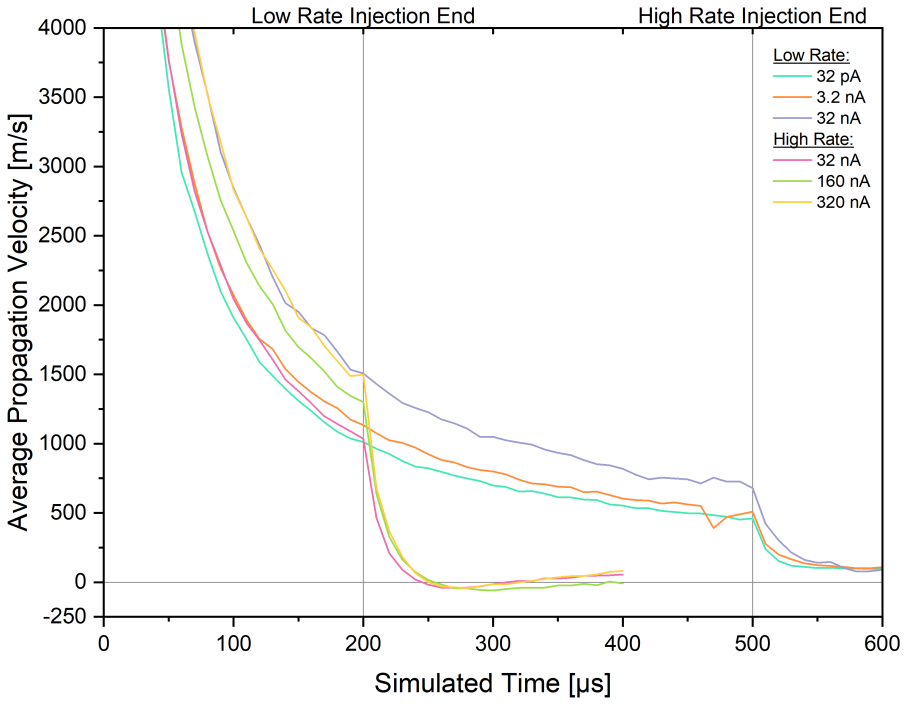

Figure 6.16: Average propagation velocity $\dot{z}$ of the particles in m/s for all beam currents over simulated time in µs. Different injection duration for the high and low rate simulations are indicated by their respective end-of-injection times. Higher beam currents lead to larger average propagation velocities. The drop after injection end indicates some influence of injection on the equilibrium state inside the cooler. For a short period after injection end, the propagation velocity becomes negative, when averaged over all ions.

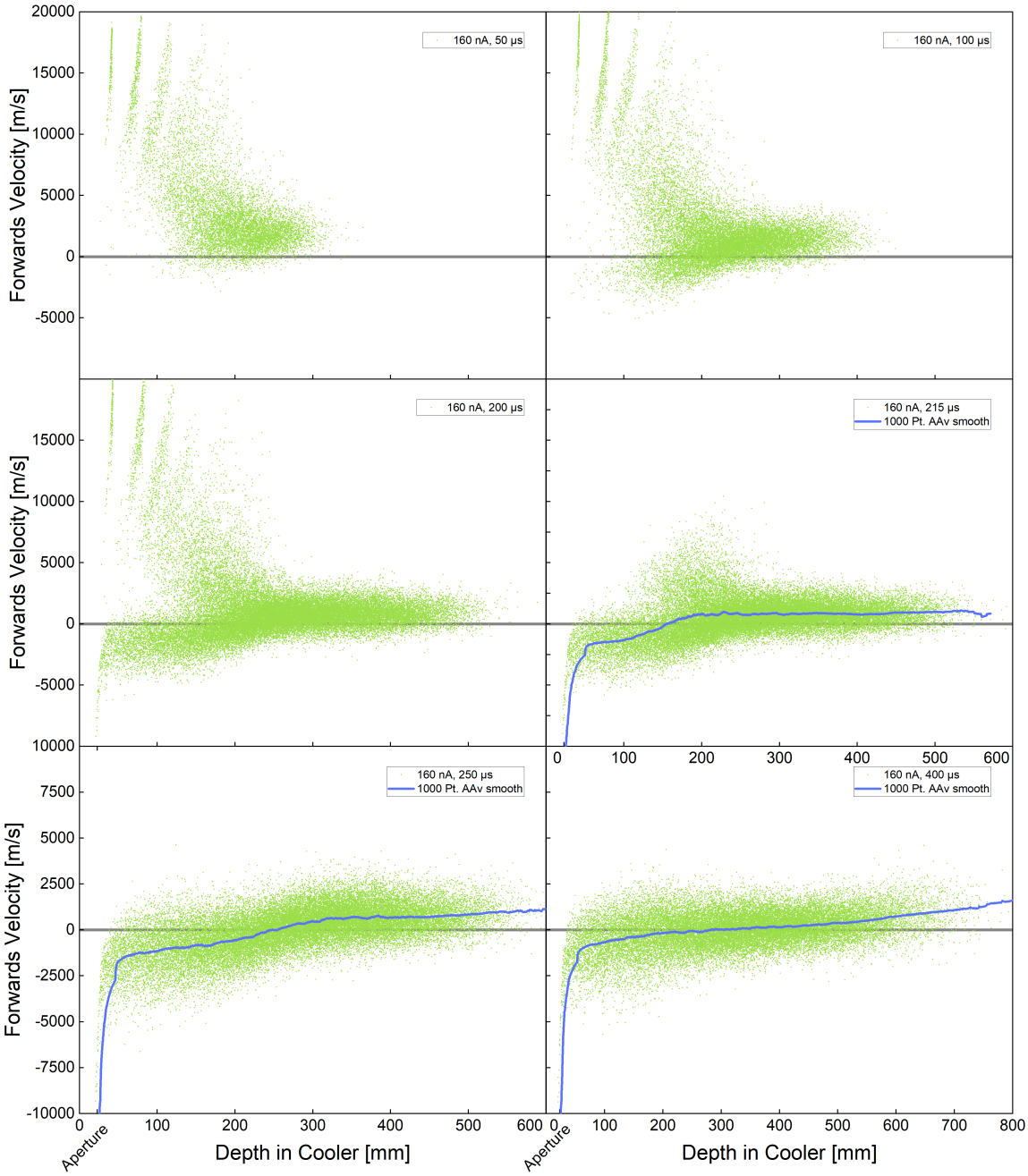

Figure 6.17: Time progression of the propagation velocity phase space (m/s, mm) in the cooler for a 160 nA high rate simulation. An 1000 point adjacent averaging (AAv) depicts the upward trend of velocity for higher depths at later times. The 0 velocity line indicates the division into forwards or backwards movement. Notice the different x-axis scale in the last plot. The constant stream of injected high-velocity ions can be seen for the first 200 µs, slowing down and accumulating around a mean deposition depth. The ions distribute through the cooler length and the diffusive transport process causes some ions to move backwards and have negative propagation velocity throughout the cooler. The propagation velocity is predominantly positive in depths after mean deposition depth and negative before. After injection ends, the distribution changes and a new equilibrium develops.

orders of magnitude, but the average energy grows with increasing ion current from 0.1 eV for low beam current, up to several eV for high beam current simulations. The distribution also appears to have a sharp cut towards high energies, while having a tail towards low energies. This correlates well with the tail towards long residence times in the real measurement data. The constant injection every 2 µs results in every particle possessing only multitudes of 2 µs as lifetime, manifesting as straight lines of dots upwards at the corresponding times with spaces in-between. The empty space of seemingly missing data at the beginning of the 3.2 nA simulation corresponds to times when the simulation was incorrectly aborted by the computer operating system or crashed, resulting in partially unrecoverable data points. It is suspected that the particle position and momentum data could be recovered as the simulation continued without problems after the crash, but the lifetime data for that period is lost.

A different kind of phase space, namely the energy of every particle over depth in the cooler, is represented in figure 6.19. The figure compares the phase space of a 32 pA to a 32 nA simulation at 150, 500 and 600 µs after simulation start. The injections end at 500 µs, thus 600 µs depicts the situation 100 µs after end of injection. While the 32 pA simulation shows the ions being deposited at their mean deposition depth with an average terminal kinetic energy with a narrow spread in both dimensions, the 32 nA simulation shows a large spread in the depth dimension, filling the cooler space to a much larger degree. At the same time, the low current has not propagated forwards significantly. The main propulsion method at higher currents seems to be displacement due to charge repulsion.

Complementary to figure 6.17 and 6.19, the time progression of the kinetic energy phase space for the 160 nA simulation is shown in figure 6.20. The continuous injection can be seen as an additional band of states coming from the high energy, low depth region until t=200 µs. Ions lose energy through the buffer gas collision and are asymptotically thermalized near a mean deposition depth. As that region fills, the ions are displaced by Coulomb repulsion either in positive or negative beam direction, causing an expansion of the ion cloud in both directions. Curiously, in contrast to the velocity phase space in figure 6.17, the state band does not linearize, and a wave-like protrusion of higher-energy particles appears at different depths. This corresponds to a fluttering, or wobble-like behaviour of the ion cloud. Bends in the otherwise straight ion cloud appear at different depth positions performing seemingly wave-like motion and making the transportation process seem unstable. The underlying cause of this is difficult to determine. Simulation artefacts are possible explanations but seem unlikely because the effect is continuous and regular, whereas artefacts would be expected to occur in an irregular, or intermittent manner. Other physical explanations include heating, other effects from the RF field, or contracting effects due to additional deceleration of the main ion bulk in the high gas density region of the center. In any case, if this finding turns out to be a real effect in ILIAMS, it would support the idea that there is no true steady state of ion transmission, the system is always close to, but not in equilibrium and a space charge distribution is never fully stationary.

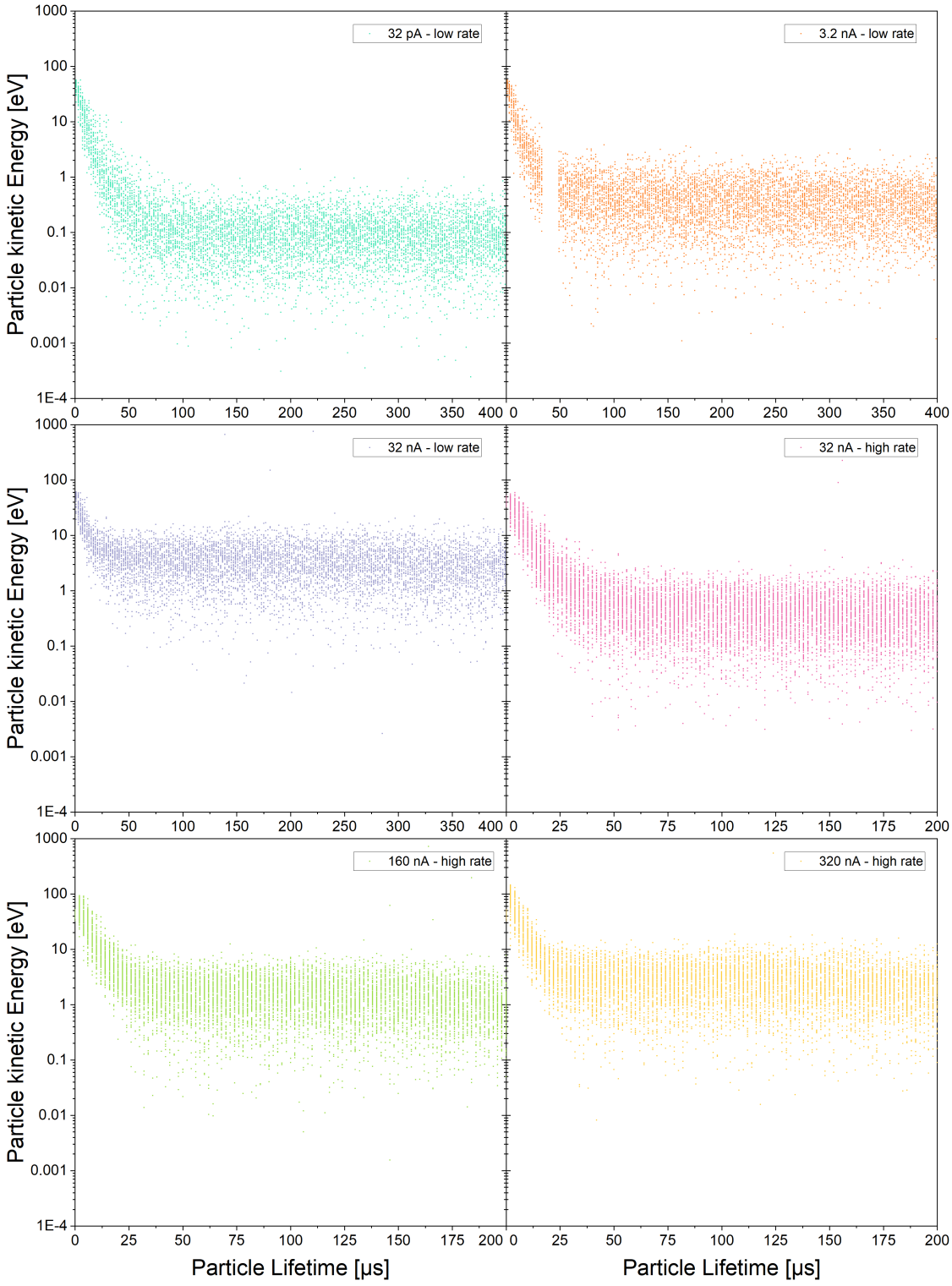

Figure 6.18: Particle scatter diagram showing the kinetic energy (eV) and corresponding lifetime (µs) of every particle in the simulation during injection (high@200 µs, low@500 µs) for different ion currents. For the high current simulations, only 25% of particles are shown for viewability. Larger ion beam currents correlate with higher average ion energies and therefore lower cooling efficiency.

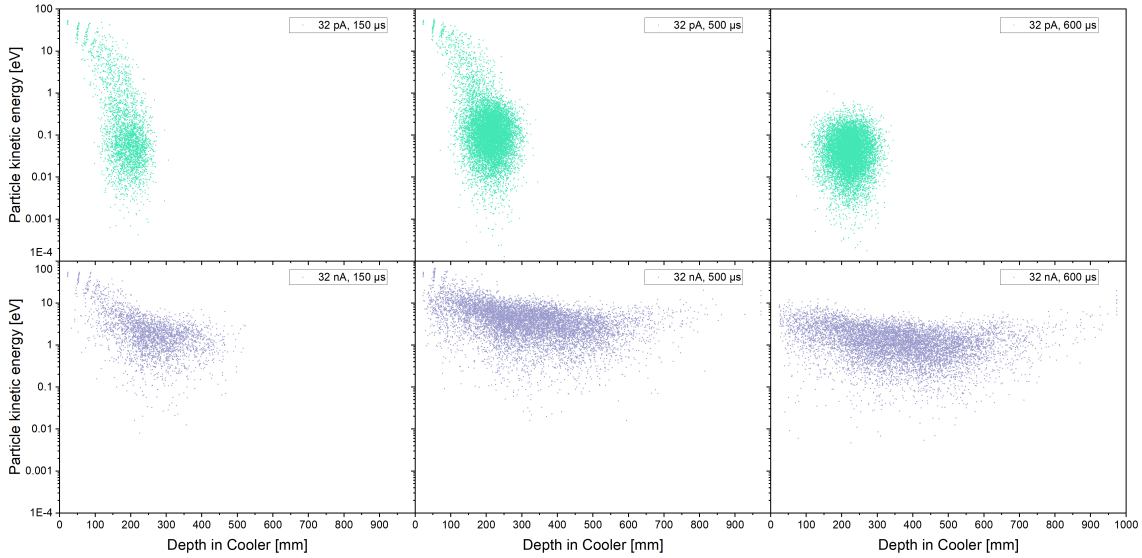

Figure 6.19: Comparizon of phase space (eV, mm) for 2 different beam currents (32 pA and 32 nA low rate) for three different times in the simulations (t=150, 500, 600 µs). The stream of injected high-energy ions can be seen until 500 µs. While the very low 32 pA beam current leads to a regular cooling and accumulation of ions around mean deposition depth, the larger repulsion from stronger space charge fields in the larger current 32 nA leads to quick distribution of ions along the entire cooler length, as well as higher average energy.

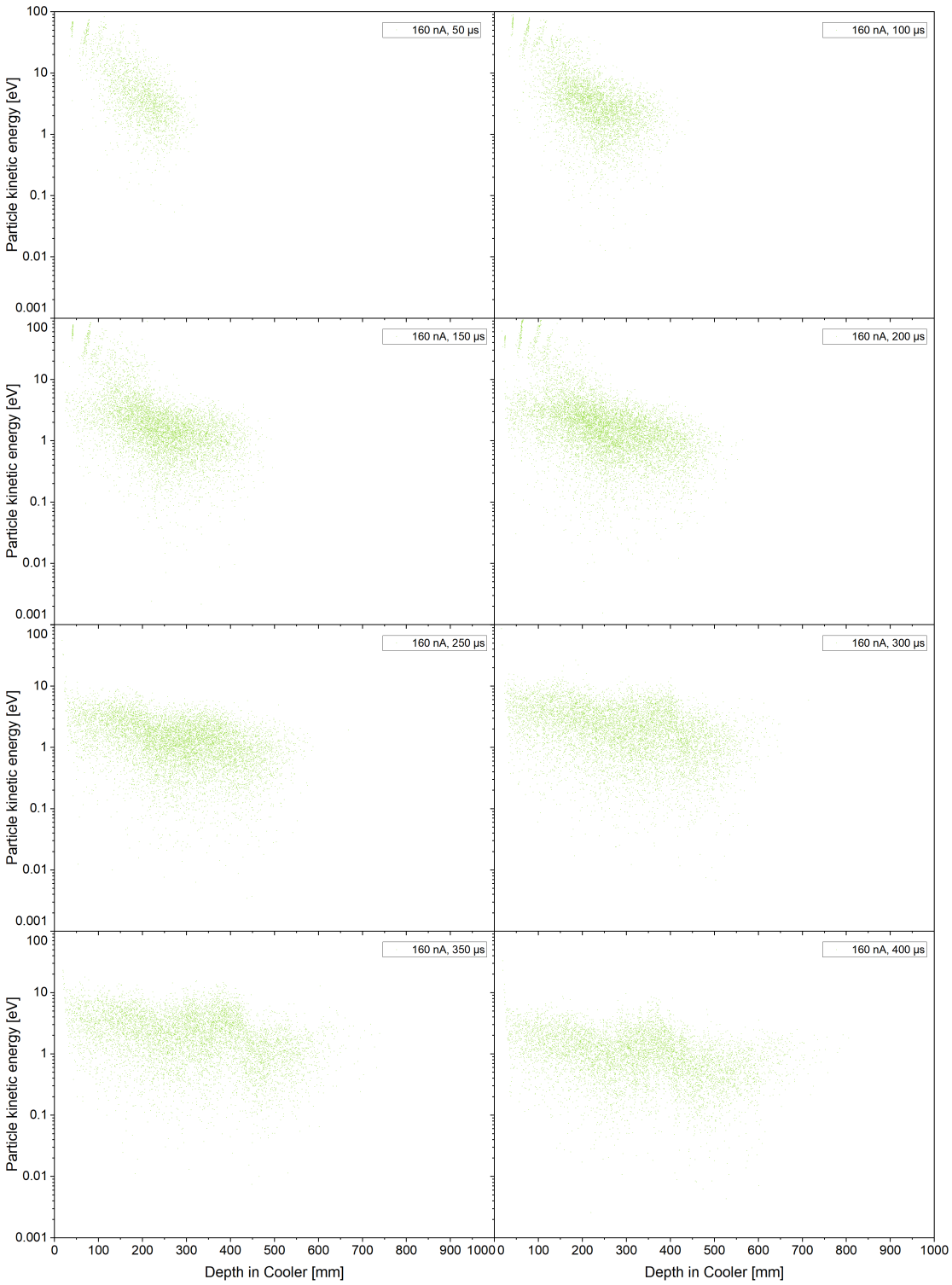

Figure 6.20: Time progression of the kinetic energy phase space (eV, mm) in the cooler for a 160 nA high rate simulation. The respective time is indicated in the legend. Only 25% of particles are shown for viewability. The injected high-energy ions can be seen to cool and accumulate around mean deposition depth until end of injection at 200 µs. Most ions distribute forwards, but some diffuse back towards the entrance aperture at low velocities.

Prediction of Residence Time

The residence time is the most elementary parameter for measurements with ILIAMS and key for sufficient isobar suppression. As the bulk of the ions never reach the exit in these simulations, however, it is impossible to obtain a value here.

It is nonetheless possible to make predictions for the residence time following equation 6.1. At any point in the simulation, an estimate for the remaining residence time in the cooler can be made for any particle from taking its depth in the cooler z_P and dividing the remaining distance until it reaches the full length of the system l_{sys}, through the current propagation velocity $\dot{z_P}$ of the particle. To get a prediction for the full residence time, the current residence time t_{res} of the particle so far is added. A possible velocity increase in the thinning buffer gas regions closer the exit due to space charge is not considered.

$$t_{res,pred.} = t_{res} + \frac{l_{sys} - z_P}{\dot{z_P}} \tag{6.1}$$

After equation 6.1 is applied to all ions when they are at near-terminal propagation velocity, 30 µs after the end of injection, the resulting histograms are depicted in figure 6.21 for the 3 low rate and 3 high rate simulation of different Cl anion beam currents.

For the 32 pA simulation, the residence time peaks around 2.5 ms, which is only approximately 25% of the value determined experimentally for Cu anions [18]. The agreement with measured data increases for more advanced particle clouds. For 3.2 nA current, the predicted residence time is at around 1.5 ms, 60% of the measured 2.5 ms, and for 320 nA, the agreement is almost 100%. More recent and elaborate residence time measurements using Cl anions, however, give a clear indication of a shorter residence time for that isotope [61], improving the agreement between simulation and experimental values.

Reasons for the disagreement might be that the particles have not reached their terminal drift velocity, or there are still overestimation effects present. It also has to be noted that the values are only a prediction and for lower currents, the ions have only propagated into very low depths of the cooler and the distance to the exit is large. In addition, the fact that agreement is better for higher currents might be because this is the region where space charge, the only simulated effect, is plausibly dominant. Other, potentially slowing effects might take place at lower currents. Also, there might be additional effects in a filled cooler, when simulating a longer continuous injection of low currents. The cooler is further away from an equilibrium state in lower beam currents and the predictive strength can therefore be expected to be weaker.

Even though the values do not agree to a high degree, a general trend can be observed: Higher currents lead to narrowing distributions and shorter residence times, agreeing well with experimental observations. A tail towards long residence times, shortening for higher currents, is a prominent feature in real data and can also be reproduced.

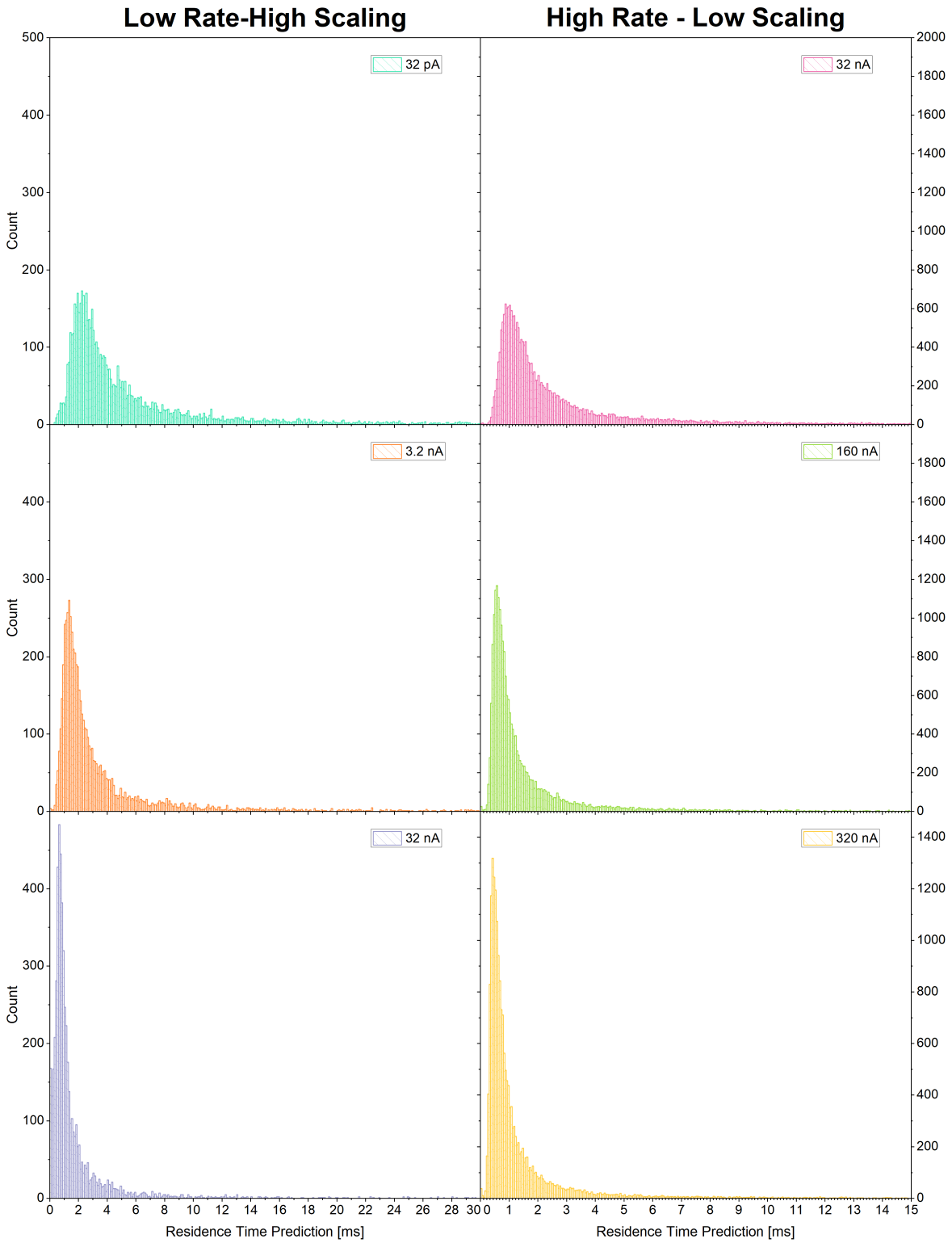

Figure 6.21: Histograms of predicted residence time in ms for 6 different approximated beam currents taken from their near-thermalized propagation velocity (low rate@530 µs, high rate@230 µs). Notice the different axis dimensions. For larger beam currents, the distribution becomes more narrow and shifted towards shorter residence times. A tail towards longer residence times can also be discerned.

7 Discussion

7.1 About the different methods

7.1.1 Arbitrary Force Method

In the arbitrary force model, we learn that the shortened residence times could potentially be explained by a constantly applied accelerating force proportional to the current. It also shows that the ion cloud diameter increases even in the absence of repulsive charge forces due to higher velocities and therefore larger trajectory deviation from the buffer gas collisions, potentially resulting in particle loss in the structure up to complete loss of beam.

All in all, even though this model can reproduce experimental data to a high degree, the physical postulations are unsound and without direct simulation results providing fundamental proof for any of the assumptions, it is naught but a toy model.

7.1.2 Convergence Method

The convergence method is an efficient and simple method, designed to determine space charge accumulation, distribution and effects in many beam dynamic simulations, but delivered only limited insight in the case of the ILIAMS simulation model. It takes an unfeasible number of iterations and related computational time to converge on a solution in a full-length simulation through the entire cooler. It cannot give insight into the experimentally founded result of shorter residence time as it shows hardly any effect on acceleration in beam direction for different beam currents.

A characteristic problem of this method is the tendency for space charge overestimation leading to inaccurate particle trajectories and nonphysical potential wells particles cannot overcome, resulting in local singularities. The convergence method may have principal difficulties with the ILIAMS model due to the abnormally low velocities of the ions, and the buffer gas collisions that can cause ion trajectories to turn back on themselves leading to an amplification of the overestimation and the incorrect computation of stationary axial charge distribution. Axial effects on e.g., particle propagation can therefore not be evaluated from this method. It is, however, applicable to show the radial space charge distribution and be a measure of the strength of its magnitude with respect to the beam current.

From the simulation results, it can be assumed that the space charge distribution is primarily radial symmetric in the high density region along the axis at small radii and increasingly rectangular in the sparse outer regions due to the influence of the shape of the guiding electrodes. An anomaly is present at the injection region that is probably due to the focusing through the aperture and de-focusing afterwards. However, due to the relatively high velocities

of the particles right after injection, this anomaly does have no perceivable effect on particle propagation.

7.1.3 Fully Time dependent Method

The simulations of the injection of a particle pulse provide the most satisfying results. The inclusion of the electric field into the time dependent calculations allows for a complete consideration of the full dynamics and direct observation of how different amounts of charge in the cooler influence ion propagation. Charge scaling presents a straightforward and adequate means to approximate different amounts of charge, and thus beam currents, with little additional computational cost and allows for the creation of a series of simulations to directly compare particle dynamics and behaviour in the cooler.

Additionally, an injection cut-off after a set time in the simulation can be implemented and evaluated to recreate a real-world measurement procedure. Most importantly, the residence time decrease for higher beam currents can be explained through these simulations.

However, it has to be noted that the simulations do not fully reflect the ILIAMS ion cooler under equilibrium conditions, as that would only be the case for a completely filled cooler. How well the behaviour of ions within the filled section during injection mimics the equilibrium state is difficult to qualify, as no such simulation exists for comparison. While for high currents, the full state seems to be nearly reached after 500 µs of injection, lower current simulations would take more than 5000 µs.

Also, the behaviour of the ions for high currents does not agree with experimental results. On closer inspection, there is increasing deviation from measurement data and space charge effects seem to be overestimated for higher current approximations. This is probably caused by the breakdown of the charge scaling method from too large scaling for an insufficiently refined mesh, explained theoretically in section 4.2.2.

It is possible to overcome this inadequacy in two ways. Refining the mesh element size to ensure accurate charge distribution would increase the computational cost of calculating the electric field dramatically, as the entire volume needs to be partitioned into smaller distances along all dimensional directions and each additional mesh node provides additional degrees of freedom to be solved for. The alternative of increasing the number of simulated particles while decreasing the charge scaling by the same factor increases the calculation cost to a smaller degree, but greatly impacts the comparability between simulation runs.

Nonetheless, even though the effects are overestimated, the trend and general picture is clear. The data can be considered an over-scaled representation of the real word scenario, and with further testing, the magnitude of the overestimation can be found and these results can serve as a surrogate model for further experimentation (see appendix section A.4). The following sections discuss the final compilation of results gathered from the various simulations.

7.2 Space Charge Distribution

Initially deemed the principal result of this work, it turns out to be only of minor significance. Evaluating the space charge distribution is only viable for the stationary convergent method,

as for the fully time dependent method the space charge effectively corresponds to the particle positions in the mesh and presents as an arrangement of differently scaled Dirac delta functions. The particle behaviour resulting from directly considering all effects fully dynamically is a significantly superior measure for understanding the processes in ILIAMS.

Nonetheless, the results of the stationary convergent method demonstrate that higher beam currents lead to a more pronounced space charge field. The shape of the field is predominantly oblate, strongest along the beam axis and exponentially decreasing in radial direction for all simulations. The guiding electrodes suppress radial symmetry and cause a bias towards a rhomboid distribution in the outer regions. An abnormality of local space charge accumulation presents itself directly after the injection, where particles diverge strongly before the confining properties of the RF field take over. The detailed axial distribution of space charge from this method can not be considered an accurate representation of a real distribution, due to its inability to reproduce physical particle trajectories.

In general, while for 1 nA and 10 nA, space charge is mainly concentrated along the axis and falls off quickly, for 100 nA the volume of high charge density is significant and encompasses almost the entire particle area, suggesting large-spread space charge accumulation for higher ion beam currents. The shape of the distribution indicates a space charge sparse injection region and a strong increase of several orders of magnitude in the region where ions are slow.

7.3 Electric Field

The electric field is a valuable and fundamental prediction measure for ion behaviour in the cooler and hence transmission, residence time and measurement efficiency. The particle movement is predominantly defined by the electric field when the stochasticity introduced through buffer gas collisions is disregarded. The electrostatic field of the guiding electrodes and RF field of the RFQ rods can be considered constant in time or frequency domain respectively, but in reality, on a small and highly precise scale, the charge of each particle affects the electric field as well. Thus, the electric field is completely dynamic and moves with the particle position.

The guiding field is designed to affect particle propagation in such a way that ions have a movement bias towards the cooler exit. It is therefore a good reference measure regarding the electric field and its power to influence the axial particle movement. Graphs 6.4 and 6.10 both show a significant influence of high ion and charge numbers on the electric field. The innately constant slope of the gradient field is increasingly disturbed for higher beam currents by the self-field of the ions. This can only be expected to greatly affect the nominal particle propagation for example by additional deceleration, or acceleration affecting the ion residence time.

The magnitude of the ion self-field of the stationary convergent method is larger than in the fully time dependent method even though the latter is overestimated. While the axial distribution of the stationary converged electric field is incorrect, there is no obvious reason why the amplitude should be conversely affected. However, overestimation, artefacts or further inaccuracies of the method cannot be entirely ruled out. In addition, the simulations in the fully time dependent method do not represent equilibrium conditions, and the electric field

could simply not be fully developed. It is therefore not possible to ascertain, which field amplitudes are closer to reality.

No simulation could provide an equilibrium state electric field throughout the entire cooler length. It is unclear, whether such a field can even be considered stationary, as it may be highly dynamic and fluctuating. Higher current simulations are closer to an equilibrium state, as the ions within the system have propagated the furthest, and the effects developed the quickest. The general shape of the electric field of all simulations coincides in a broad sense and is due to the declining number of ions in higher depths. As higher current simulations are closer to the equilibrium state and the shape, which could be seen to resemble a playground slide, persists throughout the simulations, it is reasonable to assume that such a potential exists in the cooler during steady-state operation. An electric potential slide of varying, beam-current-dependent height could hypothetically explain the shorter residence times for higher currents as the ions are pushed further and more strongly by the self-field.

7.4 Beam Diameter

The laser used for photodetachment only has a certain Gaussian profile spot size of around 2 mm at most, where photon intensity quickly falls of radially, and is additionally limited by the 3 mm aperture. This turns the ion cloud diameter into a pertinent measure to evaluate effects on the quality of measurements with ILIAMS. If the ion cloud drifting through the buffer gas spreads out of the region of photon beam overlap, ions spend less time within the detachment zone. This reduces the isobar suppression efficiency and therefore compromises the main purpose of the device.

Two main underlying causes for an increase in ion cloud diameter are present in the simulations. Firstly, a larger number of ions within the cooler increases the necessary volume of space occupied by particles, because like-charged ions can not be moved to infinitely small distances due to repulsion. The Coulomb force acting between two charges at distance r changes with $1/r^2$. This means it requires progressively more force to reduce the distance between the ions, but the confining force supplied by the RF rods follows the same law and can only increase for ions farther away from the axis, closer to the rods. The only way to hold a larger number of charges in the device at the same time is for the beam to expand radially. Secondly, higher particle velocities lead to an increased off-axis deviation due to the buffer gas collisions. The mean path length between the elastic collisions increases due to higher velocities and the related decrease in collision cross section respected by the VHS model.

One conclusion from the arbitrary force simulations concerns the beam diameter. It clearly shows higher ion velocities from accelerating forces alone correspond to an increase in beam diameters, or even beam losses, without any charge effects present. In the results of the stationary convergence method, hardly any discernible, accelerating forces are present. There, the radial distance always peaks after the focal point in injection, followed by an asymptotic approach towards an average, beam-current-dependent equilibrium distance during cooling.

The fully time dependent simulations include repulsive charge effects and clear acceleration effects. The total off-axis distance must therefore be a result of the superposition of both factors and indeed, the average ion cloud radius is larger when compared to the respective currents

of the other methods. Additionally, the peak after the injection focus, where the diameter is typically largest, grows in amplitude for higher currents, which can only be explained by space charge repulsion. For higher currents, the beam diameter reduction through cooling and RF confinement becomes progressively worse and the average off-axis distance reaches up to ten times the value expected for nominal operation. Regarding the effect of the injection stop, the data shows no influence. The average beam radius continues along a trend throughout the particle's lifetime. The small changes after injection end, when observing over simulated time are due to the increased particle loss after injection end. Thus in conclusion, for high currents, the focusing capability of RF field and buffer gas cooling no longer suffice to ensure ion confinement close to the central beam axis.

7.5 Propagation, Velocity and Phase Space

Evaluating the average position, or depth of the ions over time and their average velocity in beam direction is a straightforward way to depict ion propagation and procession through the cooler. The ions reach greater depths faster and the slope indicates consistently higher velocities for higher beam currents, also confirmed by the direct evaluation of the average ion velocity in the beam direction.

A jump forward in average depth seems to occur after the injection stops. This does not correlate with a sudden increase in velocity, but an increased particle loss in lower depth regions, shifting the average position rapidly forwards. After injection ends, the average propagation velocity drops rapidly for all currents, and the new asymptotic value is nearly identical for all simulations. In some cases, the velocity even drops below 0 for a short period, indicating dominant backwards motion. The sudden drop after injection stop can support the hypothesis that the ions injected at high velocities into an already filled cooler have a heating effect and exert an additional force forwards. However, at the same time, the majority of the ions lost in the lower depth regions after injection stop are likely to possess high kinetic energy, due to the related larger off-axis distance and movement potential, thus contributing to the drop in average velocity.

The velocity-position phase space and its progression over time gives more detailed insights into the dynamic of the ions in ILIAMS. As ions are continuously injected, they slow down stochastically over the same distance and reach near-thermalization around a mean deposition depth (200 mm in fig. 6.17). In later times, that position represents the separation of dominant forwards or backwards motion. The majority of ions at positions after the mean deposition depth are distributed around a positive average velocity, while the ions before it show predominantly negative velocities. This indicates a separation of ion flow into either forwards, in beam direction, or backwards towards the cooler entrance. This correlates well with the observed electric potential, building up around mean deposition depth, which would accelerate ions forwards or backwards, depending on the position relative to the peak. The strength of acceleration depends on the height and gradient of the potential, which both grow for larger beam currents due to the increased number of charges around mean deposition depth.

This separation can also be observed when the typical ion paths are directly evaluated.

When the depth position, travelled distance and lifetime of each ion in the cooler is known, their distributions give an idea about the typical ion paths (see fig. 6.14 and 6.15). In all simulations, after thermalizing, the ion propagation velocity is near-constant and distributed around a mean terminal drift velocity, indicated by the straight gradient of mean position over lifetime. For very low beam currents, the band of possible states is narrow and straight, giving little ambiguity towards typical ion trajectory. For higher currents, however, a separation of the possible state bands can be seen, which is more pronounced for higher currents. While a dominant band continues to penetrate further into the cooler, a portion of the injected ions turns back and returns to lower depths. When considering travelled distance, the band, which splits off, is composed of ions that have travelled longer distances without penetrating far into the cooler. This equates to a higher degree of redirection and therefore to ions partaking in more collisions, which correlates to a larger loss of kinetic energy. The ions losing a larger portion of their kinetic energy early, due to buffer gas collisions, are less likely to pass through the main bulk of ions at mean deposition depth and are retarded.

Further, aside from the splitting of the band of possible states, it also widens, while the density decreases. For higher beam currents, the range of possible states increases over injection time and the probability of finding particles at any one certain position decreases, limiting the confidence of microscopic prediction. In terms of thermodynamics, a larger number of possible states equals an increase in entropy, which correlates with higher temperature, curiously counteracting the main purpose of an ion cooler. From this perspective, data suggests that the cooling efficiency is reduced for higher beam currents. The decreasing collision cross section for higher velocities can easily be credited to contribute to this, but the reason for the ions' higher velocity needs to be discussed in the first place.

Acceleration from the built-up electric potential of beam-current-dependent height around the initial mean deposition depth of the ions, as found in all simulations, is an easily justifiable cause for higher velocities. Yet, another simple, and physically sound cause must be postulated: The energy transfer of the injected, hot ions onto the cool ions already in the buffer gas system. When space charge, and with it the charge of the ions is disregarded, they can only lose their energy through interacting with the particles of the buffer gas. If, however, ion-ion interactions are considered, the Coulomb force acts between them. Forces naturally introduce energy transfer and incoming, higher energy ions distribute their energy no longer only in the buffer gas, but also partially into the interacting ion system, reducing the cooling effectiveness. An incoming stream of ions therefore increases the mean energy, and temperature of the ion cloud and higher beam currents possess higher heating power. Supplementing this hypothesis, the distribution of particle kinetic energy shows higher averages for larger beam currents during injection (see fig. 6.18). In addition, while the distribution features a sharp, well-defined cut at higher energies, there is a gradual decrease towards lower values, representing the portion of the ions which are on the verge of being turned around by the electric potential barrier. This is in excellent agreement with the long tail in experimentally measured residence times.

The kinetic energy phase space and its time progression (fig. 6.19) give further insights into the beam-current-dependence of the ion propagation dynamics. For lower injection rates, the slowed ions all behave similarly and deposit their kinetic energy in the buffer gas over essentially the same distance. The phase space fills around that mean deposition depth and

the deviation remains small in position and energy dimension for long injection periods. When higher beam currents are injected for the same duration, the ions reach higher equilibrium energy over the injection period and the width of the positional distribution grows (see also fig. 6.20). It also shows, how near-thermalized ions at equilibrium energy are distributed throughout the cooler and spread even back towards the entrance to be rejected out of the cooler. This supports the hypothesis that charge repulsion and displacement become dominant at high beam currents, while for low beam currents, the guiding field is the main transport mechanism.

7.6 Residence Time Prediction

Residence time is truly central for successful ILIAMS measurements. It is also the only experimentally verifiable parameter, next to the transmitted beam current. Even though full-length simulations, where particles reach the exit, could not be performed due to feasibility concerns about the computation duration of weeks to months, it is possible to extrapolate or predict the residence time. Equation 6.1 is a good prediction for ions already at their terminal drift velocity asymptote, where the average propagation speed is not expected to change significantly until they exit the cooler. A possible velocity increase in the thinning buffer gas regions closer the exit due to space charge is not considered. The predicted residence times of the simulations clearly show a trend towards shorter residence times for higher beam currents. This is a major result of this work and agrees well with the data of real residence time measurements. Especially, the characteristic tail towards long residence times in the experimental data is also present in simulated data. For higher beam currents, the distribution becomes more narrow and its mean drifts towards shorter residence times.

7.7 Particle Behaviour - Observation & Deduction

One of the major advantages, and sometimes great burdens, of particle simulations is the vast amount of data and information available. As opposed to experimental measurements, where only a small number of parameters can ever be examined and evaluated, simulations make every information on any component at any time readily available. The data can then be evaluated in every way imaginable and it is not easy to fit everything on paper. Due to the impossibility of printing out videos on paper, the behaviour of the ions within the ILIAMS ion cooler shall be described qualitatively here, in words. Some connections are drawn to other data, not easily observed when only following the particle positions over time.

The ions are initially injected and focused to a spot. Due to the high localisation of charges, this generates a prominent, narrow electric field peak at that point. Higher currents cause more charge and therefore stronger fields. The ions naturally defocus after the focal point, and also due to early, high-energy buffer gas collisions. However, for higher currents, the beam additionally diverges due to the stronger self-repulsion causing higher ion motion potential[1], thus increasing distance from the central axis for higher beam currents.

[1] Motion potential should draw an analogy to the motion amplitude, a commonly used term describing the oscillating motion of ions in RFQ but not applicable for diffusion dominated motion in a buffer gas. Motion

Higher ion motion potential correlates with higher ion energies. Additionally, elastic collisions at higher energies cause stronger trajectory diversions. Thus, even though the buffer gas density is lowest right at the entrance, the elastic collisions at relatively high ion velocities prevent the ions from being confined close to the central axis at the mean electric potential minimum. Only after having lost orders of magnitude of velocity and energy, do the ions begin to equilibrate in the cooler.

Due to the statistical character of the collisions, the final deposition depth, where the particle can be considered near-thermalized, is different for every particle. Some ions reach higher depths more quickly, while others reach equilibrium more quickly. As they lose energy and the chaos calms down, their confinement also improves and the ion movement changes into diffusion-dominated behaviour. There, movement backwards would be just as likely as movement forwards, similar to a random walk, were it not for the guiding field gradient causing a bias towards cooler exit. With continuing injection, this causes the development of a fusiform ion cloud centralizing around the mean deposition depth after the entrance and decreasing ion density towards positive and negative beam direction.

With growing ion and respective charge numbers, the space charge effects begin to develop. The electric self-field from the ion charges grows to magnitudes surpassing the guiding field voltage. Ions continue to be injected but are increasingly hindered by the space charge generated by the ions accumulated around the initial mean deposition depth. The charge accumulating around the central axis essentially counteracts the confining properties of the RF field and the ions retain their motion potential, prohibited from reaching equilibrium. The electric potential minimum is now no longer at the central axis but is radial-symmetrically shifted outwards. If one ion moves into the central bulk, either itself or another ion is pushed out. Ions with high motion potential can also move around the bulk, overcoming the blocking ions in the center and continue to penetrate deeper into the cooler.

As the ion number and correlated charge increase, the outer positions are increasingly filled as well. The space charge, initially concentrated along the axis, spreads outwards until the ions reach motion amplitudes that cause them to lose confinement and crash into the RF rods or other inner structures of the device. Ions that have lost too much kinetic energy from early buffer gas collisions do not overcome the blocking ions and are increasingly retarded. The electric field in front of them causes a biased movement back towards the entrance. Eventually, one tip of the ion cloud extends back to the injection aperture, where the deceleration lens can pull them out of the RF field. Ions on the verge of turning around have the lowest kinetic energy.

At the other end of the cloud, the ions have an increasing bias towards a forward movement and are essentially accelerated, or pushed by the ions behind them. They reach higher velocities and propagate farther into the device. The collision cross section relevant for buffer gas cooling is reduced for higher ion velocities. The electric field can push them over the region of highest buffer gas density near the center, where the cooling efficiency decreases again. This allows them to stay at higher velocities and faster ions correlate with less ion-ion interaction time and decreasing space charge effects. The lower ion density and higher velocity in this region manifests as a skewed, slope-like electric potential, which reinforces the acceleration effect.

amplitude correlates with the kinetic energy, which the motion potential is equivalent to.

Due to Coulomb interactions, the injected ions with higher energy transfer some of their kinetic energy to the slower, more stationary ions they approach from behind. This energy transfer continues onward through the cloud until the energy dissipates. With each additional ion, the total energy gain increases and the collective energy gain and consequently the average energy of the equilibrium state ion cloud thus depends on the injected ion current. The cooling effectiveness is reduced because the ions deposit their energy no longer only within the buffer-, but also in the ion-gas system. The increased ion cloud excitation results in higher particle velocities, which in turn reduces the collision cross section with the buffer gas, amplifying the effect.

Once the injection ends, the influx of additional energy stops. The ion distribution changes, as the number of charges near the entrance and the corresponding electric field decreases. The ion cloud disperses with a motion bias corresponding to the electric field. The ions near the mean deposition depth, generating the large electric potential barrier, spread away from the peak of the electric field, which in turn slowly lowers, and finally collapses the electric potential barrier. Once the potential barrier is low enough, the ions once hindered by it can have a chance of turning around via the constant guiding field gradient, which now becomes the prominent transport factor again. This portion of the ions will first need to accelerate through the guiding field to reach terminal drift velocity and have significantly longer residence times. Until the full collapse of the electric potential, the ions in front obtain additional forwards acceleration from the electric field, but once all ions have reached the average ion-ion distance, the additional energy obtained from injection dissipates in the buffer gas, and ion propagation is significantly slower.

At this point, the only space charge effect is the greater number of higher energy particles at larger motion potential, because lower motion states are still blocked. Only a portion of ions at the aft end of the ion cloud can drop off into the free space generated by the cloud propagating forwards. This results in a marginally higher excitational state of the ion cloud for higher beam currents for the remainder of their journey through the RFQ ion cooler. As more and more high energy ions leave the cooler through the extraction aperture, the mean excitation decreases until finally, the slowest of the remaining ions leave the system.

8 Conclusions

Simulating space charge effects in a buffer gas filled Radio Frequency Quadrupole is no simple task. The diffusive behaviour of ions in a buffer gas adds levels of complexity to the anyway difficult task of accounting for individual Coulomb interactions between charged particles. Any attempt to approximate by assuming partially stationary fields showed drawbacks such as non-convergence or significant inaccuracy. The only reliable means has proven to be the fully time dependent simulation method, whereby all particle positions and their corresponding charge field are computed in each time step fully dynamically.

However, even with the powerful single computer workstation available (see A.8), it was not possible to perform these complex computations for simulated periods approaching typical residence times of ions in the cooler, as doing so would require months of real time. Nevertheless, important insights into the physical processes governing ion propagation inside ILIAMS were made and the deeper understanding thus allows more reliable and improved predictions for different measurements.

In brief, injected ions are cooled in the buffer gas and accumulate near a mean deposition depth, from where they propagate away through biased diffusive behaviour in the guiding field. Accumulation leads to the build-up of an electric space charge potential, which acts in addition to the guiding field and either propels the ions forwards, or hinders them and repulses them back to the entrance, acting as a barrier. As soon as the ions are transported away quickly enough, an equilibrium state is established. While its exact shape, the distribution, might be dependent on details such as buffer gas pressure or ion species, the area under the curve, the total electric potential energy, is mainly determined by the injected current, as it directly corresponds to the number of charges present. While this accelerative effect adversely affects the residence time, higher velocity and space charge repulsion also increase the diameter of the ion cloud inside the RFQ field, reducing the laser-ion overlap and therefore the isobar suppression efficiency as well.

In addition, higher beam currents lead to a larger fraction of injected kinetic energy deposited into the ion plasma system instead of the buffer gas, leading to higher average ion energies and therefore temperature, counteracting the cooling purpose of the device. The correlated increase in entropy reduces predictability, and thus tunability and capacity for optimization of the system. Furthermore, the mean deposition depth varies for injected mass, different injection energies and buffer gas pressures. These are additional factors not accounted for in these simulations, which would have an impact on the equilibrium state and ion transport. Every injected beam thus likely defines a singular equilibrium state within the cooler and with it different ion transport characteristics.

8.1 Implications for ILIAMS

Initially, when work on this thesis began, the objective was to better understand the processes inside the ILIAMS ion cooler in order to outline possible adaptations, which could overcome present limitations regarding injected ion current. However, with the insights obtained in these simulations, a solution to current problems seems even further away and poses a significant challenge. Increasing the beam current while keeping the same level of transmission and isobar suppression efficiency seems to be an impossible task.

Ions have to spend sufficient time in the interaction zone, where laser and ion beam overlap, in order to achieve good isobar suppression through photodetachment. Increasing the buffer gas pressure to improve cooling will increase the average ion cloud diameter and reduce this overlap and thus isobar suppression efficiency. Increasing RF field voltage and adjusting settings to ensure more highly confined ions will, at the same time, redistribute their momentum along the beam axis and cause higher velocities, thus shorter residence times, which again reduces the isobar suppression efficiency.

Inverting the tilt of the guiding electrodes to cause a deceleration bias showed little promise in preliminary simulations, as ions did not propagate slower while the average off-axis distance increased. Changing the polarity of the guiding field electrodes would likely have a similar effect. The electric space charge potential of higher beam currents surpasses the guiding field voltage in most cases. Also, if it were indeed possible to significantly slow the ions, the larger number of charges would again increase the diameter of the ion cloud. Even if the confinement, hypothetically, could be improved in such a way that large ion numbers, orders of magnitude above what is currently possible, are tightly packed along the beam axis and at the same time forward propagation was sufficiently restricted to ensure long residence times, the overall excitation inside the ion cloud would increase significantly and lead to other unexpected effects, possibly including general electron detachment if the excitational energies are high enough.

The main problem within ILIAMS is the repulsive acceleration due to localized charge accumulation at mean deposition depth, which comes naturally from stochastic kinetic energy loss in the buffer gas. Changing the parameters of the buffer gas would not improve the situation either, however. Lower inlet pressures would shift the mean deposition depth closer towards the center, widen and lower the accumulation distribution and related electric potential, but reduce cooling and residence time. Higher inlet pressures would narrow and heighten the distribution and shift the center toward the entrance aperture, but only to such a degree that it prohibits the injection of new ions. Any other method that shifts the position of the ions away from the accumulation zone, for example, additional electric fields, would either require accelerating them further into the cooler, resulting in anyway shorter residence times, or removing them entirely, which in turn would be equivalent to injecting a lower beam current in the first place.

All in all, increasing the beam current, while keeping the same residence times will inadvertently increase the number of charges in the cooler. For interacting ions, each occupying a certain volume due to repulsion, this inherently leads to an increase in necessary space. As the cooler is assumed to be filled over the full length of the axis when in equilibrium, the volume can only increase radially. In order to still sufficiently photodetach and remove the

unwanted isobaric component from the ion cloud, the laser spot size needs to grow with the ion cloud profile, while keeping a sufficient photon intensity at each point in the plane. The radial dimension of the RFQ, the inscribed radius, could also grow with the spot size to allow for larger ion numbers to be trapped and transported through the device at the same time. Finally, the simplest approach to solving the current limitation problem would be an increase in device length. As the space charge effects decline over the length of the RFQ buffer gas drift section after initial deposition depth, the ions are less and less affected by it, making the positive effect of longer drift sections on residence time potentially superlinear.

8.2 Future Endeavours and Outlook

The beam current limit for ILIAMS operation seems to be rooted firmly in all physical processes determining ion transport through a Radio Frequency Quadrupole ion cooler. The limit is therefore strictly dictated by device geometry and design. Possible improvements towards a higher ion current limit in future models include: a laser with larger spot size and equal photon density, larger inscribed radius and an increased length.

In terms of possible continuations of this work, a couple of questions are still not answered. What is the level of overestimation of the space charge effects in the fully time dependent simulations? How does the equilibrium state distribution look precisely for different currents and especially, for low currents? How does the space charge barrier develop over longer periods for different currents, and is the prediction of ion behaviour correct? How do different cooler parameters such as buffer gas density, guiding field strength, injected mass and others affect the space charge distribution and particle propagation? How can different cooler designs and geometries affect the behaviour and especially the beam current limitation? How can the simulation model be expanded to include other effects, such as reactive gases aiding in electron detachment or molecular dissociation, photodetachment with a laser in an interaction zone, recombination of compounds to new molecules in the gas or others?

All these problems can easily be configured to be included even in the present simulation model, but a main hindrance to answering these questions has been, and still is, the complexity of the problem from a computational perspective. Setting the boundary conditions and applying physical laws is simple in COMSOL®Multiphysics, but the only method proven to be reliably accurate, is computing the full dynamics at each time step. This requires large amounts of computer processing time, such that the simulation of the first 500 µs of time in the cooler takes roughly 8-10 days of real time to finish and provide 400 GB of stored data. Simulating for the expected low current (pA to few nA) residence times of up to 15 ms would therefore require almost a year to finish and several TB of HDD space, even with the very powerful workstation available (see sec. A.8). If further investigations of this kind are wished for, the author suggests researching ways to simulate using cluster computing resources, to significantly increase processing speed to feasible levels. The author also applauds and wholeheartedly wishes the best of luck to the future researchers tackling the unresolved questions and continuing this work.

Bibliography

[1] Ph. Gaggl. Multiphysics simulation of negative ions in a gas filled RF-quadrupole, 2021. Masterthesis, University of Vienna.

[2] VERA. Isotopenphysik website. `https://isotopenphysik.univie.ac.at/`. accessed 2.2.2023.

[3] W. Kutschera. Progress in isotope analysis at ultra-trace level by AMS. *International Journal of Mass Spectrometry*, 242(2):145–160, 2005.

[4] Y. Wang, X. Hou, Y. Fan, and et al. Determination of ^{129}I in vegetation using alkaline ashing separation combined with AMS measurement and variation of vegetation iodine isotopes in Qinling Mountains. *Journal of Radioanalytical and Nuclear Chemistry*, 326:1457–1466, 2020.

[5] M. Zhang, X. Hou, Zh. Zhang, L. Zhang, N. Chen, and M. Fang. Rapid analysis of ^{129}I in natural water samples using accelerator mass spectrometry. *Atomic Spectroscopy*, 42:190–196, 2021.

[6] W. Kutschera, P. Collon, H. Friedmann, R. Golser, P. Hille, A. Priller, W. Rom, P. Steier, S. Tagesen, A. Wallner, E. Wild, and G. Winkler. VERA: A new AMS facility in Vienna. *Nuclear Instruments and Methods in Physics Research Section B: Beam Interactions with Materials and Atoms*, 123(1):47–50, 1997.

[7] A. Priller, R. Golser, P. Hille, W. Kutschera, W. Rom, P. Steier, A. Wallner, and E. Wild. First performance tests of VERA. *Nuclear Instruments and Methods in Physics Research Section B: Beam Interactions with Materials and Atoms*, 123(1):193–198, 1997.

[8] P. Steier, S. Puchegger, R. Golser, W. Kutschera, A. Priller, W. Rom, A. Wallner, and E. Wild. Developments towards a fully automated AMS system. *Nuclear Instruments and Methods in Physics Research Section B: Beam Interactions with Materials and Atoms*, 161-163:250–254, 2000.

[9] P. Steier, R. Golser, V. Liechtenstein, W. Kutschera, A. Priller, Ch. Vockenhuber, and A. Wallner. Opportunities and limits of AMS with 3-MV tandem accelerators. *Nuclear Instruments and Methods in Physics Research Section B: Beam Interactions with Materials and Atoms*, 240(1):445–451, 2005.

[10] M. Martschini, P. Andersson, O. Forstner, R. Golser, D. Hanstorp, A. O. Lindahl, W. Kutschea, S. Pavetich, A. Priller, J. Rohlén, P. Steier, M. Suter, and A. Wallner. AMS of ^{36}Cl with the VERA 3mv tandem accelerator. *Nuclear Instruments and Methods in*

Physics Research Section B: Beam Interactions with Materials and Atoms, 294:115–120, 2013.

[11] R. Golser and W. Kutschera. Twenty years of VERA: Toward a universal facility for accelerator mass spectrometry. *Nuclear Physics News*, 27(3):29–34, 2017.

[12] P. Steier, R. Golser, W. Kutschera, A. Priller, Ch. Vockenhuber, and S. Winkler. VERA, an AMS facility for "all" isotopes. *Nuclear Instruments and Methods in Physics Research Section B: Beam Interactions with Materials and Atoms*, 223-224:67–71, 2004.

[13] P. Steier, R. Golser, W. Kutschera, V. Liechtenstein, A. Priller, A. Valenta, and C. Vockenhuber. Heavy ion AMS with a "small" accelerator. *Nuclear Instruments and Methods in Physics Research Section B: Beam Interactions with Materials and Atoms*, 188(1):283–287, 2002.

[14] O. Forstner, P. Andersson, C. Diehl, R. Golser, D. Hanstorp, W. Kutschera, A. Lindahl, A. Priller, P. Steier, and A. Wallner. Isobar suppression in AMS using laser photodetachment. *Nuclear Instruments and Methods in Physics Research Section B: Beam Interactions with Materials and Atoms*, 266(19):4565–4568, 2008.

[15] M. Martschini, D. Hanstorp, J. Lachner, Ch. Marek, A. Priller, P. Steier, P. Wasserburger, and R. Golser. The ILIAMS project – an RFQ ion beam cooler for selective laser photodetachment at VERA. *Nuclear Instruments and Methods in Physics Research Section B: Beam Interactions with Materials and Atoms*, 456:213–217, 2019.

[16] M. Martschini, J. Lachner, K. Hain, M. Kern, O. Marchhart, J. Pitters, A. Priller, P. Steier, A. Wiederin, A. Wiese, and et al. 5 years of Ion-Laser InterAction Mass Spectrometry—status and prospects of isobar suppression in AMS by lasers. *Radiocarbon*, 64(3):555–568, 2022.

[17] J. Pitters. Laser photodetachment in a gas-filled RF-quadrupole, 2015. Masterthesis, University of Vienna.

[18] T. Moreau. Development and characterization of the Ion Laser InterAction Setup (ILIAS), 2016. Masterthesis, University of Vienna.

[19] O. Forstner, P. Andersson, D. Hanstorp, J. Lahner, M. Martschini, J. Pitters, A. Priller, P. Steier, and R. Golser. The ILIAS project for selective isobar suppression by laser photodetachment. *Nuclear Instruments and Methods in Physics Research Section B: Beam Interactions with Materials and Atoms*, 361:217–221, 2015.

[20] H. Synal. Developments in accelerator mass spectrometry. *International Journal of Mass Spectrometry*, 349-350:192–202, 2013.

[21] W. Kutschera. An overview of world-wide AMS facilities. *Nuclear Instruments and Methods in Physics Research Section B: Beam Interactions with Materials and Atoms*, 538:87–94, 2023.

[22] M. Martschini, J. Pitters, T. Moreau, P. A., O. Forstner, D. Hanstorp, J. Lachner, Y. Liu, A. Priller, P. Steier, and R. Golser. Selective laser photodetachment of intense atomic and molecular negative ion beams with the ILIAS RFQ ion beam cooler. *International Journal of Mass Spectrometry*, 415:9–17, 2017.

[23] COMSOL Inc. Comsol webpage. `https://www.comsol.com/`. accessed: 13.5.2023.

[24] M. Schiffer, O. Marchhart, A. Priller, S. Herb, G. Hackenberg, S. Heinze, M. Martschini, E. Strub, T. Dunai, R. Golser, and A. Dewald. An advanced radio-frequency quadrupole ion cooler for accelerator mass spectrometry. *Nuclear Instruments and Methods in Physics Research Section B: Beam Interactions with Materials and Atoms*, 528:27–33, 2022.

[25] J. Lachner, Ch. Marek, M. Martschini, A. Priller, P. Steier, and R. Golser. ^{36}Cl in a new light: AMS measurements assisted by ion-laser interaction. *Nuclear Instruments and Methods in Physics Research Section B: Beam Interactions with Materials and Atoms*, 456:163–168, 2019.

[26] J. Lachner, M. Martschini, A. Kalb, M. Kern, O. Marchhart, F. Plasser, A. Priller, P. Steier, A. Wieser, and R. Golser. Highly sensitive ^{26}Al measurements by Ion-Laser-InterAction Mass Spectrometry. *International Journal of Mass Spectrometry*, 465:116576, 2021.

[27] M. Honda, M. Martschini, O. Marchhart, A. Priller, P. Steier, R. Golser, T. Sato, T. Kazuaki, and A. Sakaguch. Novel ^{90}Sr analysis of environmental samples by Ion-Laser InterAction Mass Spectrometry. *Anal. Methods*, 14:2732–2738, 2022.

[28] K. Hain, S. Adler, F. Gülce, M. Martschini, J. Pitters, and R. Golser. Isobar suppression studies for ^{99}Tc detection using Ion-Laser InterAction Mass Spectrometry (ILIAMS). *Nuclear Instruments and Methods in Physics Research Section B: Beam Interactions with Materials and Atoms*, 531:109–114, 2022.

[29] A. Wieser, J. Lachner, M. Martschini, D. Zok, A. Priller, P. Steier, and R. Golser. Detection of ^{135}Cs & ^{137}Cs in environmental samples by AMS. *Nuclear Instruments and Methods in Physics Research Section B: Beam Interactions with Materials and Atoms*, 538:36–40, 2023.

[30] I. Kapchinskii and V. Teplyakov. A linear ion accelerator with spatially uniform hard focusing. *Prib. Tekh. Eksp.*, 1970(2):19–22, 1970.

[31] A. M. Lombardi. CAS school for small accelerators. In *The radio frequency quadrupole (RFQ)*, 2006.

[32] J. Staples. RFQ's: An introduction. 1990. Technical Report, Lawrence Berkeley National Lab. (LBNL), Berkeley, CA, `https://www.osti.gov/biblio/6527337`.

[33] F. Major, V. Gheorghe, and G. Werth. *Charged Particle Traps - Physics and Techniques of Charged Particle Field Confinement*. Springer Berlin, Heidelberg, first edition, 2004.

[34] P. Wolfgang. Electromagnetic traps for charged and neutral particles. *Reviews of Modern Physics*, 62(3):531–540, 1990.

[35] H. Okamoto, Y. Wada, and R. Takai. Radio-frequency quadrupole trap as a tool for experimental beam physics. *Nuclear Instruments and Methods in Physics Research Section A: Accelerators, Spectrometers, Detectors and Associated Equipment*, 485(3):244–254, 2002.

[36] W. Itano, J. Bergquist, J. Bollinger, and D. Wineland. Cooling methods in ion traps. *Physica Scripta*, 1995(T59):106, 1995.

[37] Y. Liu, J.F. Liang, G.D. Alton, J.R. Beene, Z. Zhou, and H. Wollnik. Collisional cooling of negative-ion beams. *Nuclear Instruments and Methods in Physics Research Section B: Beam Interactions with Materials and Atoms*, 187(1):117–131, 2002.

[38] A.E. Litherland, I. Tomski, X.-L. Zhao, Lisa M. Cousins, J.P. Doupé, G. Javahery, and W.E. Kieser. Isobar separation at very low energy for AMS. *Nuclear Instruments and Methods in Physics Research Section B: Beam Interactions with Materials and Atoms*, 259(1):230–235, 2007.

[39] J. Rienstra-Kiracofe, G. Tschumper, H. Schaefer, S. Nandi, and G. Ellison. Atomic and molecular electron affinities: Photoelectron experiments and theoretical computations. *Chemical Reviews*, 102(1):231–282, 2002.

[40] G. Gutsev and A. Boldyrev. The electronic structure of superhalogens and superalkalies. *Russian Chemical Reviews*, 56(6):519, 1987.

[41] R. Middelton. *A Negative-Ion Cookbook*. Department Of Physics, University of Pennsylvania Philadelphia, PA 19104, 1990.

[42] L. Palumbo M. Ferrario, M. Migliorati. CAS-CERN accelerator school: Advanced accelerator physics, Trondheim, Norway. In *Space Charge Effects*. CERN, 2013.

[43] N. Pichoff A. Chance. Lecture master npac (nuclei, particles, astroparticles, cosmology). In *Beam dynamics with space-charge*. CERN, 2020.

[44] K. Schindl. Space charge. `https://cds.cern.ch/record/941316/files/p305.pdf`. CERN Records/Educational Notes.

[45] D. Guo, Y. Wang, X. Xiong, H. Zhang, X. Zhang, T. Yuan, X. Fang, and W. Xu. Space charge induced nonlinear effects in quadrupole ion traps. *Journal of the American Society for Mass Spectrometry*, 25(3):498–508, 2014.

[46] Zh. Xiaohua, W. Yuzhuo, H. Lili, G. Dan, F. Xiang, Zh. Mingfei, and X. Wei. Reducing space charge effects in a linear ion trap by rhombic ion excitation and ejection. *Journal of The American Society for Mass Spectrometry*, 27:1256–1262, 2016.

[47] M. Baus and J. Hansen. Statistical mechanics of simple Coulomb systems. *Physics Reports*, 59(1):1–94, 1980.

[48] A. Vlasov. The vibrational properties of an electron gas. *Soviet Physics Uspekhi*, 10(6):721, 1968.

[49] S. Bazhal and R. Hellborg. Beam envelope techniques for ion-optical calculations. `https://s3.cern.ch/inspire-prod-files-2/2ccf683c79fb9fef1dfc971e6b03b0c9,accessed:16.5.2023`. CERN Records/Educational Notes.

[50] M. Ferrario. CAS–CERN accelerator school: Free electron lasers and energy recovery linacs, Hamburg, Germany. In *Space Charge Mitigation*. CERN, 2016.

[51] E. Lee and R. Cooper. General envelope equation for cylindrically symmetric charged-particle beams. *Part. Accel.; (United States)*, 7:2, 1976.

[52] J. Struckmeier. Improved envelope and emittance description of particle beams using the Fokker-Planck approach. `https://doi.org/10.48550/arXiv.2307.12272`, 2023.

[53] H. Widom C. Tracy. Asymptotics in ASEP with step initial condition. *Communications in Mathematical Physics*, 290:129–154, 2009.

[54] D. Wolf, P. Keblinski, S. Phillpot, and J. Eggebrecht. Exact method for the simulation of Coulombic systems by spherically truncated, pairwise r^{-1} summation. *The Journal of Chemical Physics*, 110(17):8254–8282, 1999.

[55] F. Read, A. Calupka, and N. Bowring. The charge-tube method for space-charge simulations. *COMPEL - The international journal for computation and mathematics in electrical and electronic engineering*, 18(4):548–555, 1999.

[56] R. Boussaid, G. Ban, J. F. Cam, and C. Vandamme. Simulations of high intensity ion beam RFQ cooler for DESIR/SPIRAL 2: SHIRaC. *Journal of Instrumentation*, 9(07):7009, 2014.

[57] P. Wasserburger. Simulation und Optimierung des Laser-Ionen-Aufbaus an VERA, 2018. Masterthesis, University of Vienna.

[58] COMSOL Inc. *COMSOL Multiphysics Reference Manual, Version 6.1.*

[59] Multiphysics cyclopedia. `https://www.comsol.com/multiphysics`. accessed: 27.4.2023.

[60] COMSOL Inc. *Particle Tracing Module User's Guide.*

[61] F. Albrecht. Measurement of ion residence times in the ILIAMS cooler with a new multi-beam switcher, 2024. Masterthesis, University of Vienna.

Acronyms

AMS Accelerator Mass Spectrometry. iii, v, 1–3, 5, 8, 11–13

ASEP Assymetric Simple Exclusion Process. 18

BM Bending Magnet. 5

CAD Computer Aided Design. 25

CPU Central Processing Unit. 28, 29

DOF Degrees of Freedom. 24, 26, 27, 36, 37

EA Electron Affinity. 9–11

ESA Electrostatic Analyzer. 5, 12

FEM Finite Element Method. 23–25, 31, 33, 38

FLOPS Floating Point Operations Per Second. 28

HDD Hard Disk Drive. 29, 95

ILIAMS Ion-Laser InterAction Mass Spectrometry. i, iii, v, viii, 1–3, 5–9, 11, 17–21, 23, 37, 42, 43, 46, 47, 53, 55, 56, 58, 60, 62, 64–68, 70–72, 74, 76–78, 80–87, 89, 93–95, 105–107, 112–115, 117, 118

IoI Isotope of Interest. 2, 6, 11

MBS Multi Beam Switcher. 5

MC-SNICS Multi Cathode Source for Negative Ions by Cesium Sputtering. 5, 11

RAM Random Access Memory. 28

RF Radio Frequency. iii, v, 6, 7, 12, 13, 17, 19, 20, 25, 32, 42, 47, 61, 65, 68, 77, 85–87, 90, 94, 116, 117

RFQ Radio Frequency Quadrupole. iii, 2, 6–9, 11, 13, 17, 19, 20, 31, 42, 46, 47, 49, 50, 53, 61, 85, 89, 91, 93, 95, 105, 107, 108, 110, 112, 115, 116

RFQs Radio Frequency Quadrupoles. iii, 6

SSD Solid State Drive. 28, 29

VERA Vienna Environemental Research Accelerator. iii, v, 1, 2, 5, 13

VHS Variable Hard Sphere. 9, 42, 86, 106, 116, 118

List of Figures

A Appendix

A.1 VERA Beamline Complex

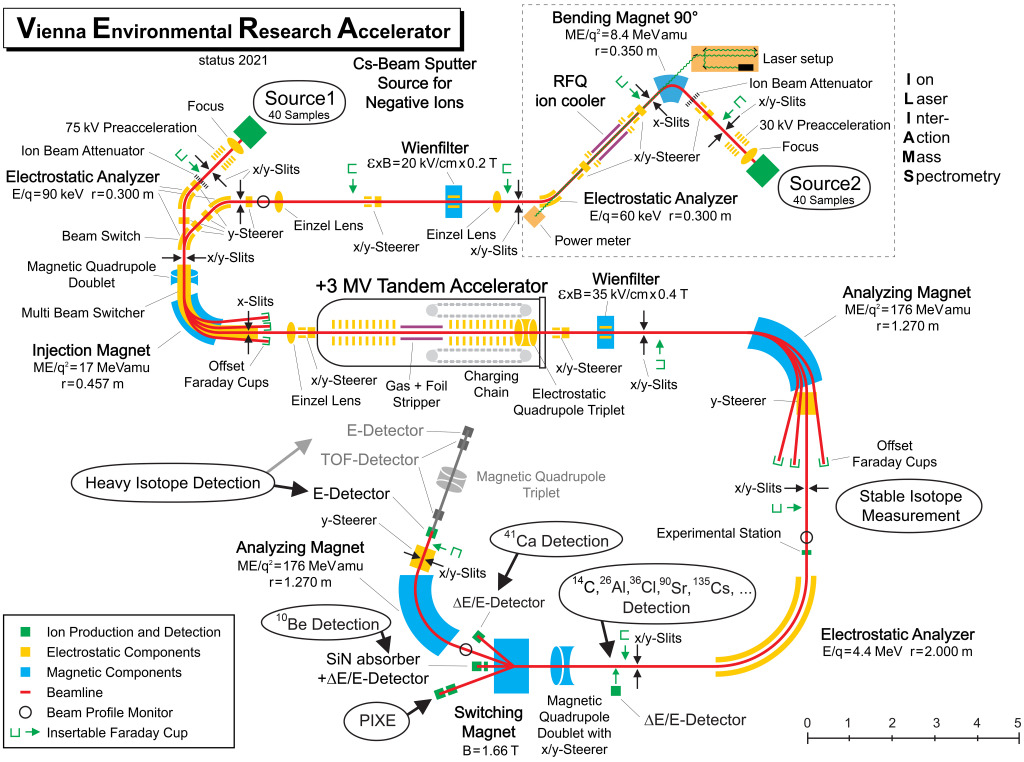

Figure A.1: VERA beamline map with components. The dedicated ILIAMS beamline is indicated by the section surrounded with dashed lines [2].

A.2 RFQ Particle Trajectories

A very basic RFQ model was used to simulate particle trajectories for different q-values and particle starting conditions. It should give insight into the complex particle motion inside.

A single particle is injected in parallel to the central axis and simulated through the RFQ for constant Mathieu q, but varying radial distances and angles in the injection plane. Its trajectory is traced with a line and the planar projection is depicted in figure A.2. Its initial momentum vector has a large influence on the trajectory: When injected in parallel to the

beam axis at a certain radial distance, the projection rotates and is skewed for different radial distances.

When injecting the particle in parallel to the central axis with the same momentum vector and initial position, but for different Mathieu q values of the RFQ, the resulting trajectory projections can be seen in figure A.3. A lateral and diagonal presentation can be seen in figure A.4.

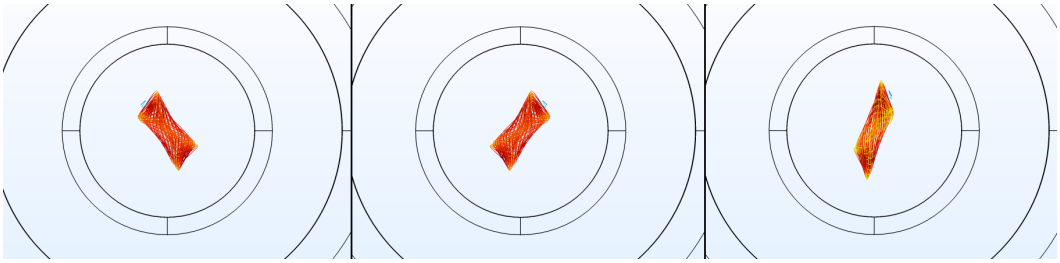

Figure A.2: Axial plane projection of particle trajectories for the same Mathieu q-value but different starting positions. The starting position greatly affects the particle trajectory. The same radial distance in a different angle results in a shifted path (left/middle), while a different radial distance from the central axis results in a different trajectory shape(right).

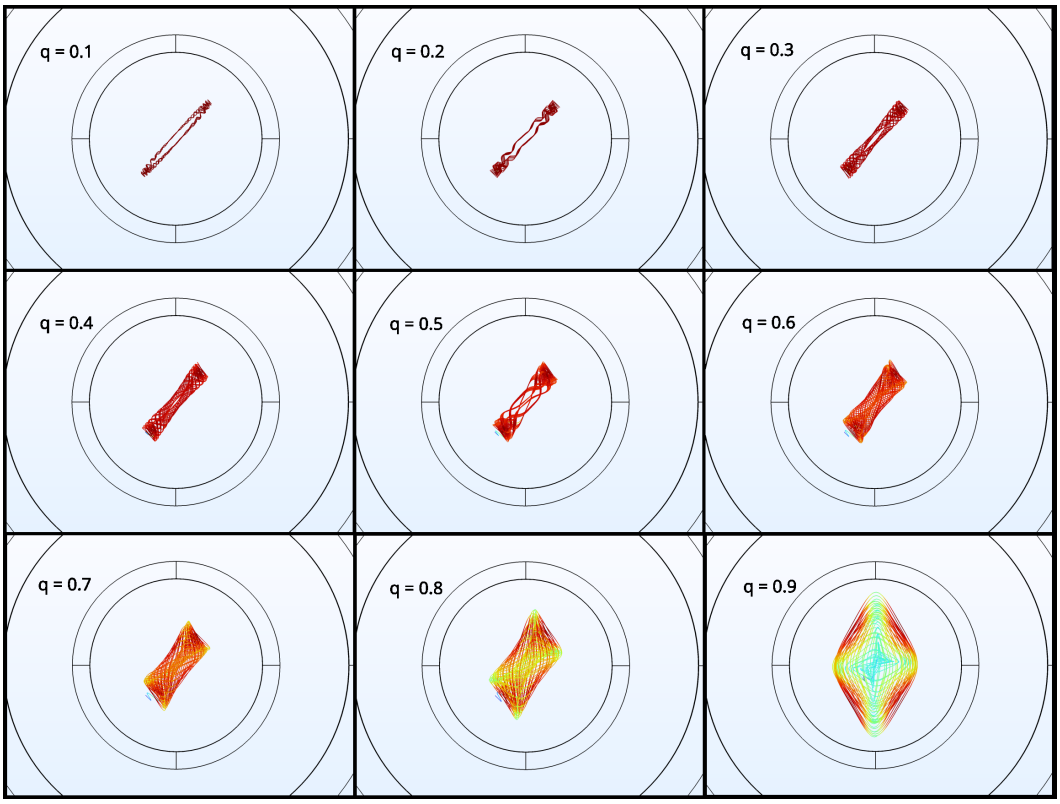

Figure A.3: Axial plane projection of particle trajectories for a single particle starting at the same starting position and velocity but different Mathieu q-values. For q=0.9 the starting position has the same angle but 33% of the radial distance at the starting position, as there is a significant motion amplitude blow-up

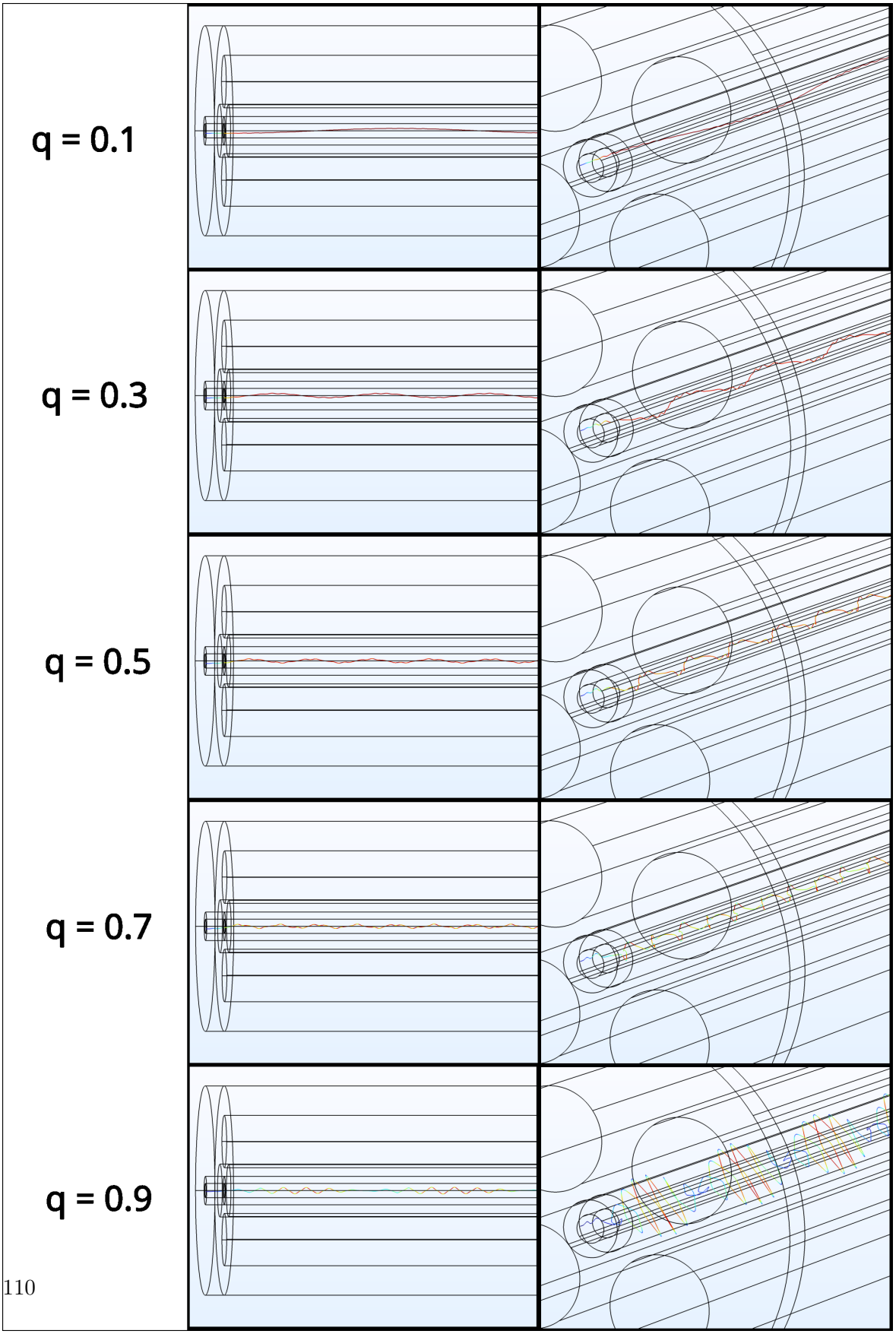

Figure A.4: Lateral and diagonal plane presentation of particle trajectories at the entrance to the RFQ for a single particle starting at the same starting position and velocity but different Mathieu q-values.

A.3 Simple Model - Average Off-Axis Distance without Buffer Gas

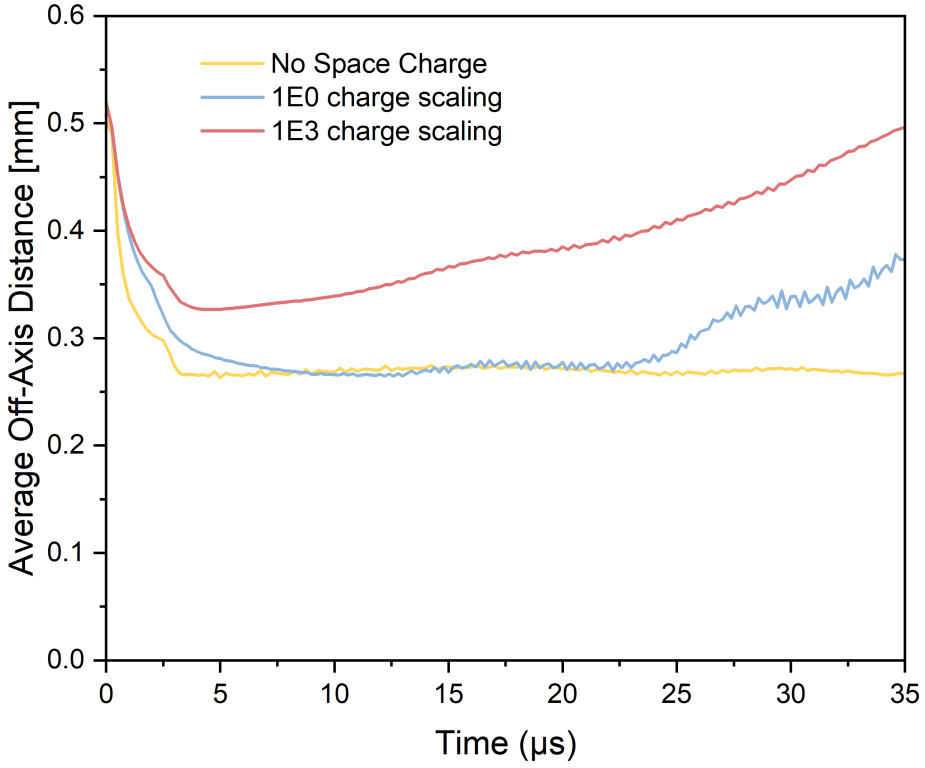

Figure A.5: Average Off-Axis Distance of ions in mm over simulated time in µs for the simple model without buffer gas. The average distance and therefore ion beam diameter increases for larger charge numbers.

A.4 Charge Overestimation

This section includes simulation results, which were disregarded in the main sections due to significant overestimation: approximated beam currents of 96, 160 and 320 nA. All simulations here have a base injection frequency of 40 simulated particles per 2 µs.

A plot, showing the number of active in-flight particles in the system compared to the mean particle lifetime over the time in the simulation is shown in figure A.6. The number should increase linearly due to the constant injection rate. While this is true for lower currents, the gradient seems to decline for higher currents, subject to a growing loss rate because particles

are lost after being veered into an unstable trajectory, and collide with inner RFQ structures from large charge repulsion. The loss rate increases with the number of ions in the system until it equals the injection rate, leading to the asymptotic approach of a certain amount of charge in the system. This could indicate a charge limit for the real ILIAMS for very high currents. A high particle loss rate for the higher currents causes the particles to have shorter average lifetimes resulting in a plateau effect for the average lifetime. This affects all data and graphs, where parameters are plotted against average lifetime, as particles of equal lifetime can have different values and some long lifetimes do not exist at higher currents. The jitter of the 96 nA line is due to a sudden particle loss close to the injection at around 170 µs, possibly caused by unrecoverable data after a simulation crash. The effects are overestimated, however, which could potentially mean they can occur in the real system for very high operating currents in the several µA-range.

Other data from the overestimated plots include the average radial distance over time (see figure A.7), average depth in the cooler over simulated time or particle lifetime (see figure A.8) and average propagation velocity over time or particle lifetime (see figure A.9).

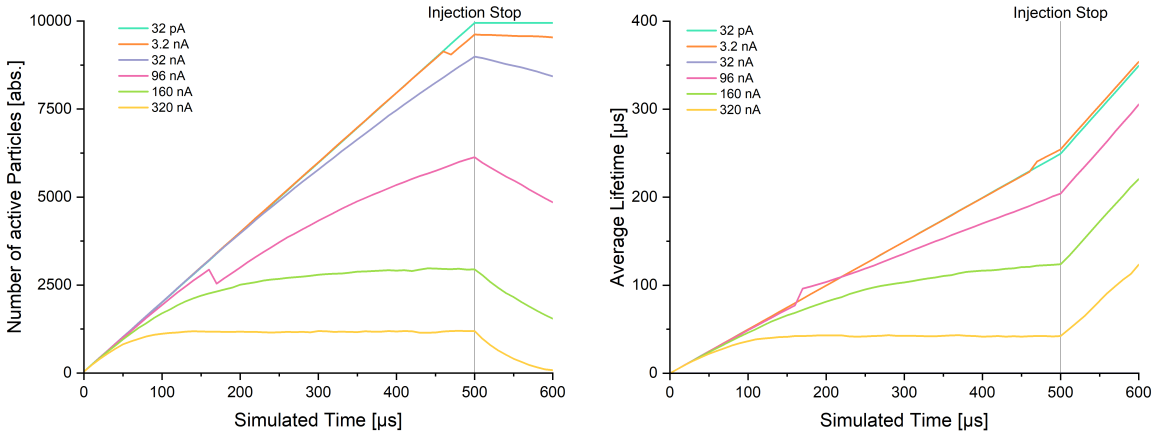

Figure A.6: Number of active in-flight particles in the simulation (left) and average particle lifetime (right) over time for different beam currents. There is increasing particle loss for larger beam currents, also reflected in the average particle lifetime. At 320 nA beam current, the number seems to have reached a limit.

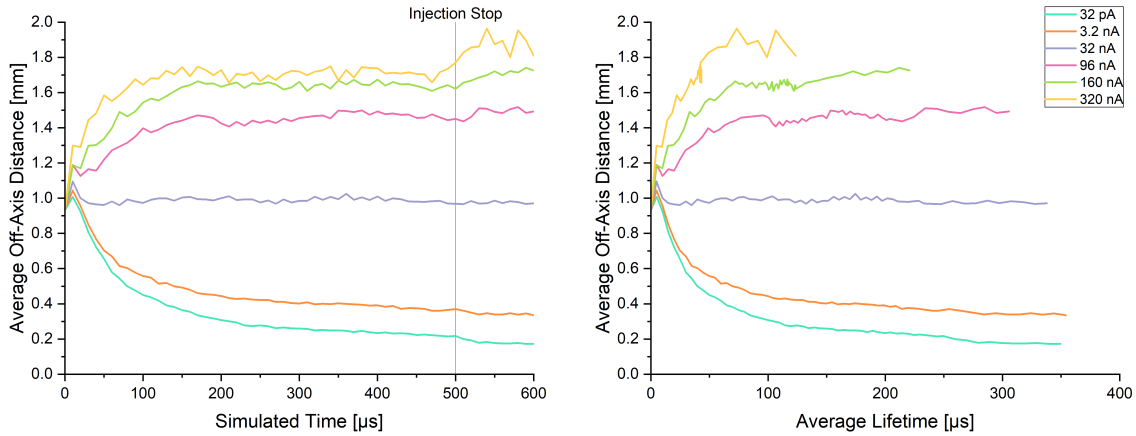

Figure A.7: Radial distance from the central axis in mm averaged over each particle within each time step over simulated time in µs (left) or alternatively over average particle lifetime in µs (right) for different beam currents. The average ion cloud radius is larger for higher beam currents.

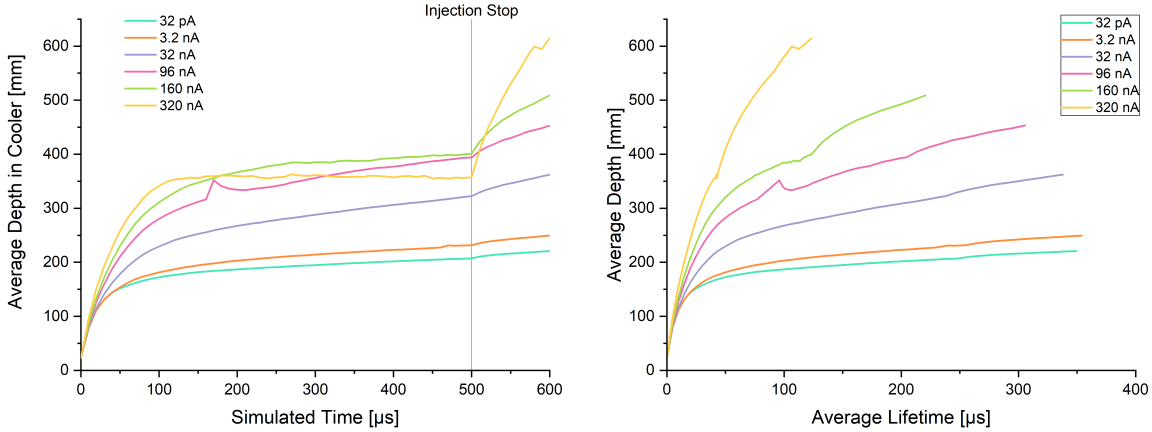

Figure A.8: Average particle depth or position within ILIAMS in mm over time (left) or over average particle lifetime in µs (right) for different beam currents. The depths reached by the particles in the cooler are larger for higher currents.

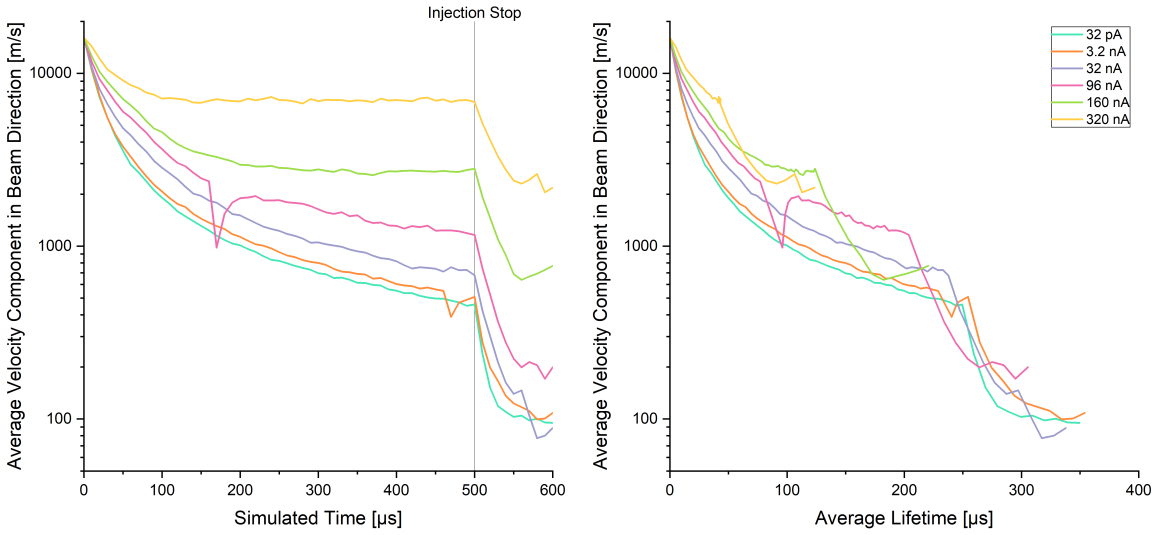

Figure A.9: Average particle propagation velocity $\dot{z}$ within ILIAMS in m/s over simulated time in µs (left) or over average particle lifetime in µs (right) for different beam currents. The velocities are larger for higher currents.

A.5 Scaling Tests

To benchmark the validity of the simple model, a couple of exploratory simulation studies were performed in directly scaled versions of the real, full model in a $1{:}10^3$ and $1{:}10^6$ size ratio.

Considering only the electric forces the ion beam behaves exceptionally well under scaled conditions. Ignoring possible technical details in the real world such as ultra-high frequency generation and noise suppression, the ion trajectory scales directly proportional to the entire geometry when scaling the electrics to hold the Mathieu parameters constant even in the $1{:}10^6$ scale.

However, the scaling fails when trying to account for buffer gas collisions. The scattering and energy loss are fundamentally dependent on properties in the molecular dimension and do not correlate to the device geometry dimension. Ion-gas collisions cause the ion to be scattered independently from device dimensions but because of smaller typical lengths in scaled geometries, the ions are more likely to collide with inner walls and be lost. This becomes particularly apparent in the $1{:}10^6$ scale, as essentially every collision causes the ion to be scattered into the wall. Increasing the pressure so that the Knudsen number is constant for different scales only increases the problem because each collision yields ion loss and scaling down cross section or ion/gas mass in various combinations does not yield satisfying results. In the smallest dimension, ions either pass through the device unaffected by the gas molecules exiting with their initial speed or they are lost in the device after interaction making ion cooling essentially impossible. Thus, ion cooling cannot be achieved in the same way as in the real models and the ion trajectories in differently scaled models cannot be compared directly. Reducing the size of the simulation model to save resources is thus not a valid option to attain

real results.

However, the small model used in this work for qualitative exploration of space charge effects in a RFQ buffer gas ion cooler is still considered a satisfying approximation, as the flow regime is in the same region as for the real model (A.5.1) and the length scales ($\approx 1:10$) are sufficient for ion containment. The small model is, therefore, suitable to study space charge effects relevant for the real ILIAMS.

A.5.1 Scaling the Knudsen number

The Knudsen number describes the ratio of mean free path length λ over typical lengths in the confining frame L and essentially describes the ratio of inter-particle over particle-wall interactions. For an ideal gas the mean free path length can be computed from pressure p, temperature T, and particle diameter d using the Boltzmann constant k_B via equationA.1.

$$Kn = \frac{\lambda}{L} = \frac{k_B T}{\sqrt{2}\pi d^2 p L} \tag{A.1}$$

Continuum flow is assumed when inter-particle interactions dominate the particle-wall interactions (e.g. $Kn < 0.01$), while molecular flow neglects inter-particle interactions and distribution is mostly affected by wall interactions (e.g. $Kn > 10$). The transitional flow and slip flow regimes make up the region where particle-particle and particle-wall collisions are comparably frequent.

When scaling a model, the different L affect the Knudsen number and to keep it constant the other parameters must be adjusted. For ILIAMS, the $Kn \approx 10^{-4}$, which indicates continuum flow. Reducing the length scales by one order of magnitude (e.g. in the small model) the Knudsen number would still be in the continuum flow when the other parameters were kept.

A.6 Details about the Mesh

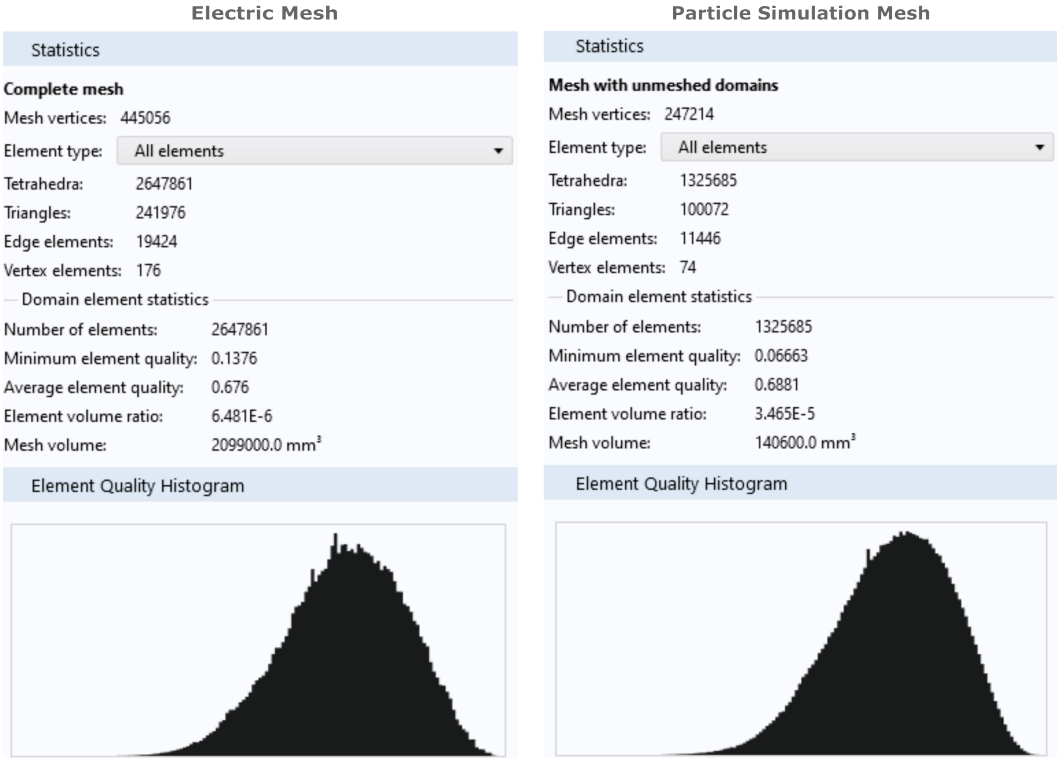

Figure A.10: Mesh statistics for the Mesh used for calculation of the stationary and time harmonic calculation of the electric fields (left), or the time dependent particle and space charge simulation (right) in the full model. The particle simulation mesh fills less volume, because only the particle tracing area is meshed

A.7 Used simulation parameters

A.7.1 Cooler Parameters

The *cooler parameters* are identical across all simulations. The low voltage injection lens is set to 940 V and the low voltage extraction lens to 400 V. The guiding field is set to 2.88 V/m. The RFQ settings are a 200 V RF voltage amplitude with a frequency of 2.6 MHz (0.38 µs period) amounting to a Mathieu q-value of 0.42. The buffer gas used for collision simulation in a VHS model is set to pure ^{4}He with a set inlet pressure of 0.3 mbar using the same parameters and configuration used in previous work ([1]). The properties of the simulated particles are set to replicate a singly charged ^{36}Cl anion.

A.7.2 Solver Details

For all simulations, the total electric field within ILIAMS is computed in a high resolution mesh first. The time-harmonic solution for the RF field is used in all later simulations and not computed again. It can be superposed on top of the time dependently recalculated electrostatic field. Further simulations use a mesh with high resolution in the particle tracing area and radially decreasing mesh quality, where domains outside the particle tracing area are not meshed.

The *RF field* is solved in the frequency domain with the *BiCGStab* (BiConjugate Gradient Stabilized) iterative solver using a *Geometric Multigrid preconditioner* (2 iterations, V-cycle, 1 multigrid level, lower element order first (any) hierarchy generation) consisting of SOR (Successive Overrelaxation) forward as a pre-moother, SOR backward (SORU) as a post-smoother and the MUMPS (MUltifrontal Massively Parallel Sparse) direct solver as a coarse solver.

The *electrostatic field* is in all cases solved using the *Conjugate Gradient* iterative solver and a *Algebraic Multigrid preconditioner* (2 iterations, V-cycle, 5 multigrid levels, classic coarsening method with hierarchy quality factor 3) with the same pre-, post- smoother and coarse solver configuration as used for the RF field solver.

Particle motion[1] is in all cases simulated with the *GMRES* (Generalized Minimum RESidual) iterative solver and a *Jacobi preconditioner*. For the cumulative bidirectionally coupled method, *MUMPS direct solver* is used to compute the cumulative *space charge density* in every time step.

When electric fields and particle motion are solved together fully time dependently, a *segregated solving approach* is applied, where the related equations are individually solved using their solver from above.

A.7.3 Buffer Gas Distribution

[1] and all other auxillary dependent variables

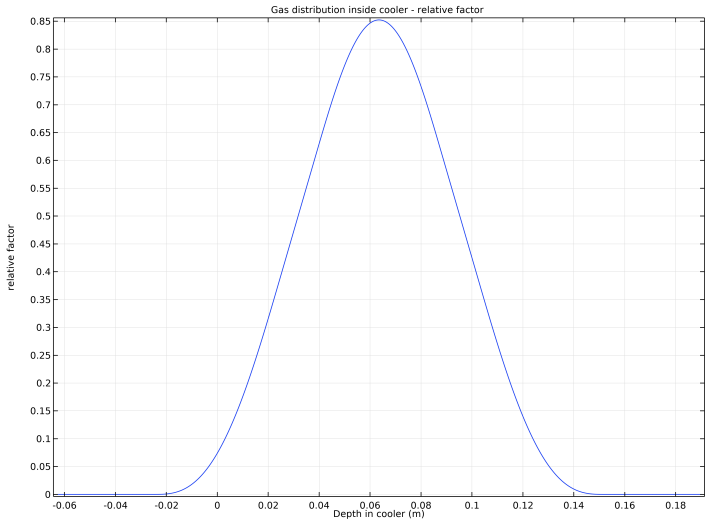

Figure A.11: Buffer gas distribution factor for the small model. A smoothed triangular distribution

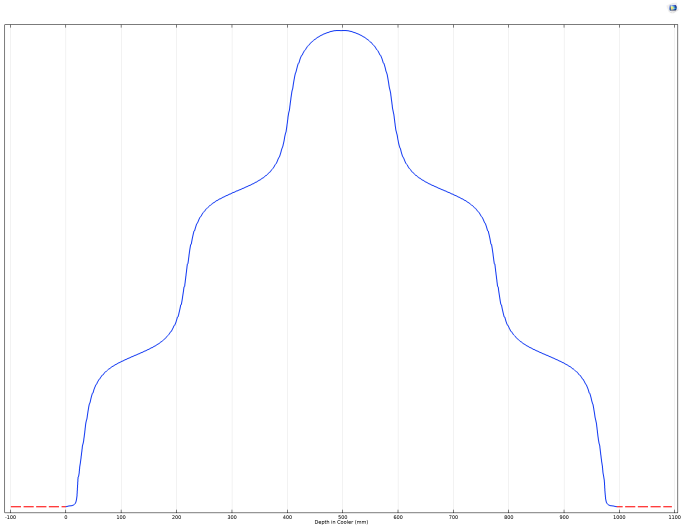

Figure A.12: Buffer gas distribution for the VHS collision model used in the full ILIAMS model. The gas density is distributed step-wise, due to the spacer plates affecting flow.

A.8 Computational Resources

	Low Resource PC	**High Resource PC**
CPU Type	Intel(R) Xeon(R) W-2125	AMD Ryzen Threadripper PRO 5975WX
CPU Speed	4,01 GHz	3,60 GHz
CPU Cores(Logical)	4(8)	32(64)
CPU L1/L2/L3	256KB/4MB/8.2MB	2MB/16MB/128MB
RAM Space	32.0GB	128GB
RAM Speed	2666MHz	3200MHz

Table A.1: Details on the computational resources used for the simulations